Aerodynamic effects of frontal elongation applied to a bluff body

According to a CFD design study

R. Wildvank

Technische Universiteit Delft

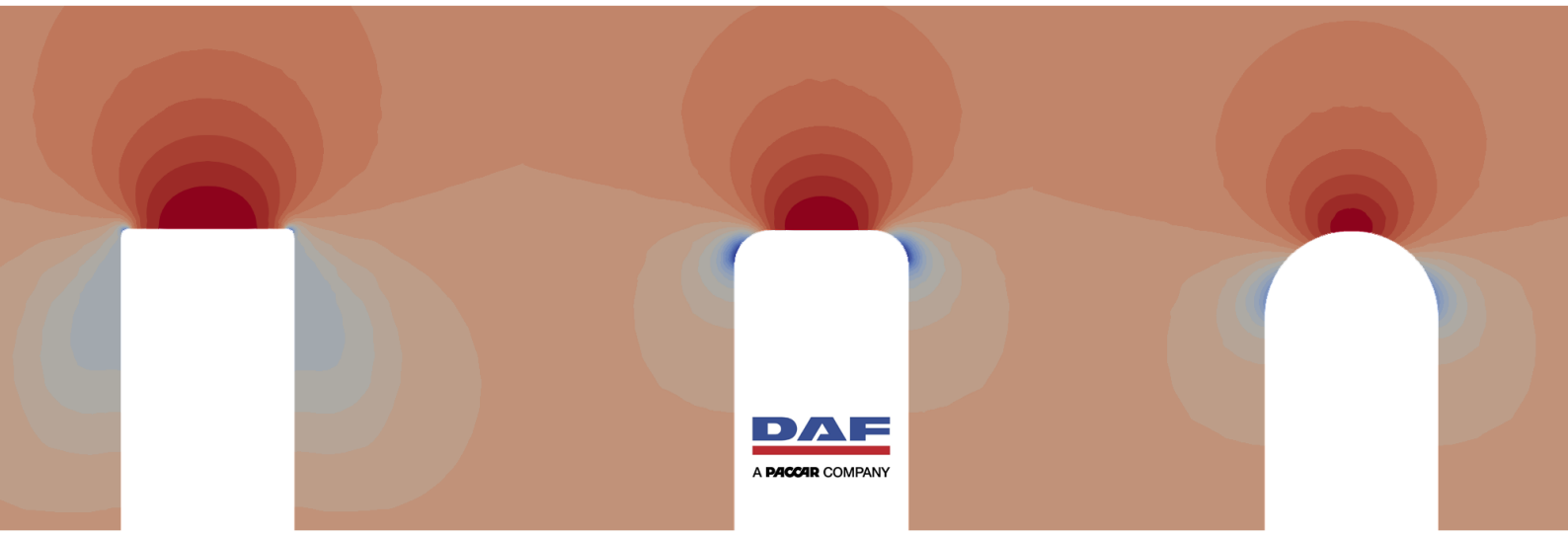

TU Delft Delft University of Technology

Challenge the future

AERODYNAMIC EFFECTS OF FRONTAL ELONGATION APPLIED TO A BLUFF BODY

ACCORDING TO A CFD DESIGN STUDY

by

R. Wildvank

in partial fulfillment of the requirements for the degree of

Master of Science
in Aerospace Engineering

at the Delft University of Technology,
to be defended publicly on Friday 26, 2018 at 10:30 AM.

Supervisor:	Prof. dr. ir. L. Veldhuis	
Thesis committee:	Dr. Ir. G. Van Raemdonck,	TU Delft
	Dr. Ir. D. Rentema,	DAF Trucks
	Ir. W. Timmer,	TU Delft

TU Delft Delft University of Technology

SUMMARY

The EU has committed itself to reduce the greenhouse gas emissions with 20% by 2020 with respect to the 1990 level. This means that all industry sectors including the transport sector have to become more energy efficient. The long and short haul trucks are, with 4.95% of the total CO_2 equivalent emissions, a major contributor in the transport sector. In order to achieve a reduction in emissions, the European Commission is proposing new regulations that allow for front elongation of trucks. This elongation might improve the aerodynamic efficiency and hence reduce the emissions and fuel costs.

Reducing aerodynamic drag for tractor-trailer combinations has been researched for a long period of time. In 1965 Hoerner published the results of his experimental research on 3D bluff bodies and identified that the drag coefficient at the front was related to the total drag coefficient. In 1985 Cooper determined that an optimal front edge radius based on the Reynolds number and the frontal area of the vehicle exists. These two studies concerning bluff bodies form the basis of numerous follow up studies and this thesis. This thesis analyses how the geometry of an elongated bluff body can be optimized in order to reduce the aerodynamic drag coefficient

Typically the flow around a bluff body is characterized instable and separated flow. At the front of the truck the incoming flow velocity reduces to zero at the stagnation point. A high pressure region is formed at this location. Further downstream the flow reaches the front edge corners of the truck, where the flow is accelerated. Flow separation might occur at these front edge corners. At the rear a large low pressure region is formed which contributes to the total drag coefficient.

In this thesis numerical simulations are performed in order to identify the relative importance of several front-end design parameters. The numerical calculations are performed by means of the steady-state RANS $k-\omega$ turbulence model. The domain is refined near the surface model and its wake using two density boxes around the model with different cell dimensions and an inflation layer around the model. A wall model is used to approximate the flow behavior in the boundary layer. The wall model and the local refinements reduce the computational time while retaining a high level of accuracy of the numerical solution.

The numerical simulation is validated using the data from an already existing wind tunnel experiment. This wind tunnel experiment has been performed on a 1:15 scale model in the Low Turbulence wind tunnel at the TU Delft. First the influence of the mesh cell size is determined by varying the cell sizes of the two density boxes surrounding the model. One density box is close to the model and has small cell dimensions, while the second density box is encapsulating a larger volume. This resulted in chosen cell dimensions with a ratio of 1:4. The discretization error is 4.1%, while the number of cells used is $4.47 * 10^6$. The second part is the validation itself. The drag coefficient of the model is 0.297 for the wind tunnel experiment and 0.300 for the simulation, while the base pressure is slightly lower for the numerical simulation. The pressure distribution at the base is not correctly captured in the simulation results. The final part of the validation is the comparison of the boundary layer development. The results of the simulation obtained in this thesis show great similarity with the results found in the wind tunnel experiment.

To explore the real world effects the 1:15 scale results are compared to 1:1 scale models. The mesh of the 1:1 scale model is different from the 1:15 scale model in two ways. First the inflation layers are attached on the rear, this is done to reduce the effect of low quality mesh elements near the base of the model. Second the inflation layers themselves are different in size due to a different development of the boundary layer at larger models. The numerical configuration for the 1:1 scale model uses a higher turbulence intensity and Reynolds number in order to better match the real world conditions. When comparing the two scaled models, these configuration differences lead to a small discrepancy in the drag coefficient. To further analyze the 1:1 scale model, the front edge radius is varied. This variation shows that a critical radius of 540 mm exists in order to keep the flow attached at yaw angles of 0, 3 and 6 yaw. Increasing the radius beyond 540 mm shows a minor decrease in drag coefficient, while a large decrease of the stagnation area and suction forces are observed.

After the analysis of the non-elongated 1:1 models, the models are elongated with 500 mm. Elongating the baseline model increases the drag slightly due to the increased wetted area. The stagnation pressure and suction force do not change when the model is only elongated.

The final part of this research explores several front designs for elongated models. The first effect that is studied is the change in circular radius. The observations are in line with the observations for non-elongated

models: when the radius is larger than the critical radius of 540 mm, the flow stays attached and only a small decrease in drag coefficient is observed. The model with the lowest drag coefficient has a circular radius of 1300 mm, the benefit over the baseline model is 6 drag counts for 3 degree yaw. Second, an elliptical front edge radius is applied. Variations in front edge radius showed minor changes in drag coefficient. Lower drag coefficients are observed when longer axes are chosen, while the minimum radius is kept constant. Finally, various frontal shapes are applied to an elongated model. The changes in frontal shapes resulted in minimal reductions of the drag coefficient.

When all models variations in this study are taken into account, an overall conclusion can be drawn: the most important parameter for the drag coefficient is the front edge radius. When the radius is equal to the critical radius, the flow stays attached for all models, which reduces the drag coefficient. Increasing the radius beyond the critical radius result in only a very small aerodynamic drag reduction. Therefore the impact of elongating bluff bodies to reduce green house gas emissions is very limited.

CONTENTS

LIST OF FIGURES

LIST OF TABLES

ABBREVIATIONS

CFD Computational Fluid Dynamics. viii, 4, 14–20, 27, 30, 32–34, 37, 57, 74

CO_2 Carbon Dioxide. vii, 1, 2, 4, 61

CoE Cab Over Engine. vii, viii, 6, 10, 16, 19, 21, 23, 25, 34, 35, 61

DNW German-Dutch Wind Tunnels. 14

DC Drag Counts. 15

DES Detached Eddy Simulation. 63

EC European Commission. 1, 62

EU European Union. 1–4, 19, 62

FAT Forschungvereinigung Automobiltechnik. vii, 8, 14, 15, 17

GETS Generic European Transport System. viii, 4, 13, 21–23, 25, 27, 31, 32, 34, 35, 38, 39, 42, 44, 46, 48, 53, 56, 57, 59

LTT Low Turbulence Tunnel. 74

GRV Ground Research Vehicle. 10

GTS Ground Transportation System. 21, 23, 52

HDV Heavy Duty Vehicle. 2, 4, 6, 23, 61

LES Large Eddy Simulation. 63

NASA National Aeronautics and Space Administration. 8–10, 23

NRC National Research Council of Canada. 16, 17

OEM Original Equipment Manufacturer. 2

PIV Particle Image Velocimetry. viii, 28, 29

RANS Reynolds-Averaged Navier-Stokes. 17, 20, 21, 25, 32

SAE Society of Automotive Engineers. 21, 25, 37, 74

SN Softnose. vii, 14–17, 53

SST Shear Stress Transport. 21

DUT Delft University of Technology. 20

US United States. 2, 16, 18, 19

LIST OF GREEK SYMBOLS

α	Inclination of the road	^{o}
δ	Boundary layer thickness	mm
δ_A	Ratio of the boundary layer thickness just upstream of the boat tail to the square root of the base area	-
δ^*	Displacement thickness	-
ϵ	Rate of dissipation of turbulence energy	-
η	Non-dimensional radius; radius divided by the square root of the frontal area	-
θ	Momentum loss thickness	-
μ	Friction coefficient	-
ρ	Density of air	kg/m^3
τ	Friction force	Pa
ω	Specific rate of dissipation	-

LIST OF ROMAN SYMBOLS

a	Acceleration	m/s^2
A_f	Frontal area	m^2
C_D	Drag coefficient	-
$C_{Df,b}$	Fore body drag coefficient	-
C_P	Pressure coefficient	-
C_{P_b}	Pressure drag at the base of the vehicle	-
C_S	Side force coefficient	-
C_T	Truck force coefficient in driving direction	-
F_{tot}	Total force	N
H	Shape factor	-
k	Turbulent kinetic energy	m^2/s^2
K	Constant in the nominator of Hoerner's equation	-
m	Mass	kg
R	Front edge radius	mm
R_{min}	Minimum radius for attached flow	m
Re	Reynolds number	-
Re_A	Reynolds number based on frontal area	-
$Re_{cr,A}$	Critical Reynolds number based on area	-
$Re_{tr,A}$	Transcritical Reynolds number based on area	-
u	velocity of the fluid	m/s
u_∞	Velocity of the undisturbed flow	m/s
w	Width of the model	mm
y^+	Dimensionless wall distance	-
y_p	Half of the first cell layer height	mm

1

INTRODUCTION

The European Union (EU) committed itself to reduce the greenhouse gas emissions with respect to the 1990 level. In order to achieve these goals all industry sectors should reduce their greenhouse gas emissions. To help the transport sector achieve these goals the European Commission (EC) is preparing new laws that allow for the relaxation of the dimensional constraints of heavy duty trucks. The EC hopes that these new regulations result in more aerodynamic efficient vehicles, which require less power and produce less emissions.

Heavy duty trucks are considered bluff bodies and are subject to complex aerodynamics. New research should be conducted in order to determine how these new dimensions can best be translated into an optimized aerodynamic shape.

This chapter will describe the context of the problem, the basics of bluff body aerodynamics and the research question of this thesis.

1.1 European climate goals

The EU has committed itself to reduce the greenhouse gas emissions with 20% by 2020 with respect to the 1990 level [8]. For 2050 the goals are even more challenging: a 60% reduction should be realized with respect to the 1990 level [9]. In order to achieve these goals it is crucial for all industry sectors, including the transport sector, to become more energy efficient. The transport sector is responsible for 19.7% of the total equivalent CO_2 emission; the emissions of long and short haul trucks account for 4.95% of the total CO_2 emissions [1] as depicted in figure 1.1.

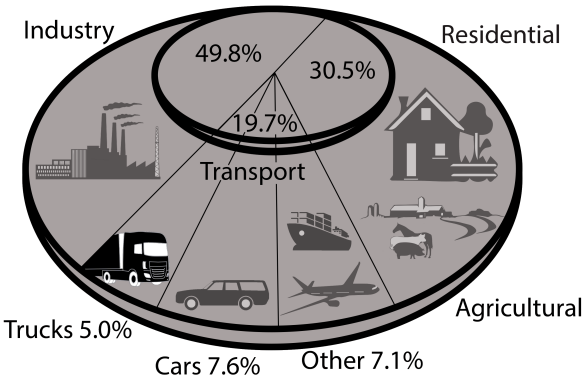

Figure 1.1: CO_2 equivalent emissions in the European Union arranged by sector type, data from 2014

Both in the transportation sector as well as in the road transportation sub sector the green house gas emissions increased by roughly 20% between 1990 and 2014, this is shown in 1.2(a) an 1.2(b).

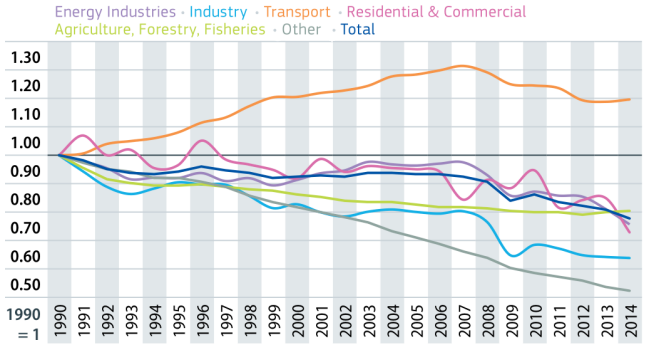

(a) Green house gases emissions by sector in million tonnes CO_2 equivalent for 2014

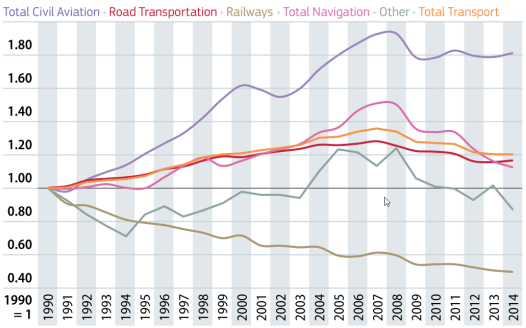

(b) Green house gas emissions by transport sector in million tonnes CO_2 equivalent for 2014

Figure 1.2: Green house gas emission specified per sector [1]

NEW EUROPEAN DIRECTIVES

Currently, heavy duty trucks are not very streamlined due to dimensional legislative constraints. In the absence of appropriate legislation and collaboration between Original Equipment Manufacturer (OEM) no real improvements were accomplished during the last decades [10]. Recent changes in regulations and the Supertruck program in the United States (US) led to more efficient commercial vehicles [11]. These efficiency gains include an automatic tire inflation system, drive train improvements and more aerodynamic shaped trailers. The Heavy Duty Vehicle (HDV) markets in the US and the EU are similar. A similar effect could be accomplished with the proposed EU directive EU/2015/719 [12], where the dimensions constraints of heavy-duty trucks are relaxed. A front elongation of 0.5m is proposed. This allows for different designs, which might be more aerodynamic, resulting in a lower CO_2 emission.

1.2 Economic incentive

The fuel consumption of an HDV is among the largest contributors to the vehicles total cost of ownership. The typical cost of operating an HDV consist of wages (40%), fuel (30%), maintenance (9%), depreciation and interest [13]. The significant share of the fuel cost gives rise to an economic incentive for transport companies to develop more aerodynamic trailers. With lower fuel cost, a significant economic benefit can be obtained.

1.3 Drag components

In order to reduce the fuel consumption the drive train and the drag components can be optimized. As such this research will focus on analyzing and reducing the drag components, in particular the aerodynamic drag.

The forces acting on a vehicle in motion can be summarized in equation 1.1 [14].

$$F_{tot} = m\frac{du}{dt} + mg\sin\alpha + \mu mg\cos\alpha + \frac{1}{2}\rho A_f C_D u^2 \tag{1.1}$$

The total force, F_{tot}, is equal to the terms on the right hand side of the equation. The first term, represents the force necessary to accelerate the vehicle, it includes the m of the vehicle and the a. The second term is caused by α of the road. The rolling resistance is covered in the third term and consist of the μ. The last part of the equation represents the aerodynamic force, which consists of the density ρ, the A_f of the vehicle, the C_D and the u.

In general long haul road transport operates at the constant maximum allowed velocity; in the EU this varies between 80 and 90km/h [1]. The power consumption on a flat road is shown in figure 1.3 [15]. The two main components of power consumption are rolling resistance and aerodynamic drag resistance. At 80km/h the aerodynamic drag contributes roughly the same as the rolling resistance, depending on the configuration of the truck, the road conditions and the operating conditions. Therefore the aerodynamic drag is an important contributor to the total drag. If one wants to optimize the aerodynamic drag the C_D is the only component which can be altered; as the ρ, A_f and the operating u are regarded as constant.

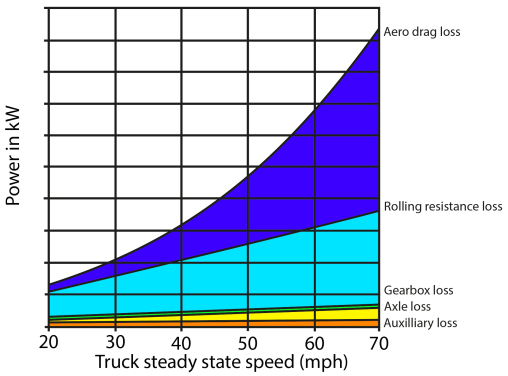

Figure 1.3: A sketch of the drag forces that a 10-tonne rigid vehicle must overcome. 50 mph equals 80.4 km/h)

According to Wong [14], the rolling resistance coefficient is dependent on the tire pressure, tire compound, smoothness of the road and velocity. This coefficient is often the subject of research to lower fuel consumption [16], [15],[17]. Furthermore the rolling force consists of the m, the gravitational constant gravity constant and the inclination of the road α.

1.4 Bluff body aerodynamics

Aerodynamic drag is an important parameter of the total drag of an heavy vehicle, especially at highway velocities. Aerodynamic drag can be split into two main components, pressure drag and friction drag. Pressure drag is the pressure difference acting on all surfaces perpendicular to the driving direction.

Friction drag is the aerodynamic drag due to the shearing action of the air against the vehicle surface. Previous studies [18] and [19] show that for bluff bodies pressure drag is dominant over friction drag.

For heavy duty vehicles, a high pressure region is located at the front and a low pressure region is located at the rear. Due to the abrupt changes at the front and rear of the body the flow separates and becomes unstable, as shown in figure 1.4(a). Increasing the front edge radius can eliminate flow separation at the front. This topic is intensively studied topic by Götz [20], Cooper [4], Newnham [21], Hennemans [22]. At the base the flow also separates. These unstable vortices are complex and are studied by Roskho [23], Hucho [24], Duell and Geogre [25] and Pastoor [26]. The vortex formation is asymmetrical and causes a periodic variation in pressure levels near the base of the vehicle.

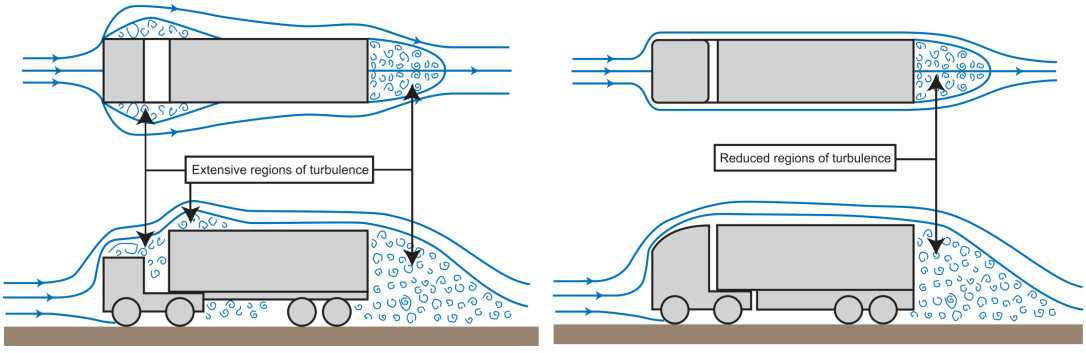

Figure 1.4: Typical airflow of a truck trailer combination. On the left, regions with extensive turbulence are present at the cabin, trailer roof and rear. On the right, an optimized combination is shown with only a wake region at the rear [2].

Flow separation is detrimental for a low drag coefficient. Therefore optimizing the geometry of the vehicle is of key importance. An optimized airflow reduces separation and wake areas, an example is shown in figure

1.4(b). Hoerner [27], Saltzman [28] and Diebler [29] studied the influence of the fore body drag on the rear and total drag. The exact nature of this relations is heavily debated, this is elaborated in section 2.2.1.

1.5 Drag reduction methods

The aerodynamic drag for HDV can be reduced by several measures. These measures include fore body design [4], platooning [30], the under body design and rear end design. Often add-on devices are used for streamlining the flow, such as side wings [31], wheel covers [32], roof spoilers [33], and boat tails [34]. However, C_D depends on the shape of the total vehicle, therefore multiple studies emphasize a holistic approach in order to optimize the drag coefficient [35] and [10]. Furthermore, Hoerner showed that the pressure distribution at the front and rear are intertwined [27].

There are two types of drag reduction methods: active and passive. Active drag reduction devices require power, are relatively complex, and have been studied extensively [36–38]. Passive drag reduction is a relatively simple and robust method, since it does not require power or include moving parts. Therefore the focus will be on passive drag reduction. This can be achieved by adjusting the geometry of the heavy-duty vehicle. The tractor-trailer can be divided into three main areas of interest for aerodynamic purposes: the front, the trailer and under body and the rear of the vehicle. In chapter 2 a detailed overview of the aerodynamic drag reductions for these areas is given.

1.6 Aerodynamic development tools

Evaluation of the aerodynamic performance of heavy duty trucks can be performed in three distinct ways; track testing, wind-tunnel testing and CFD analysis. The methods all have their own challenges.

Performing aerodynamic experiments on a dedicated test track provides realistic wind and ground conditions. Despite this advantage the difficulty lies in controlling these conditions. Furthermore, these full scale tests are very time consuming and expensive to perform.

The second option is to use a wind tunnel to measure the aerodynamics of heavy duty trucks. The results obtained from these test are repeatable and can closely match the real on-road conditions (depending on the fidelity of the boundary conditions). Disadvantage are that often simplified and scaled down models are used and turbulence intensities are different compared to the full scale models.

The use of CFD can also provide repeatable simulations that are able to match the real world on-road conditions while costing only a fraction of the track and wind tunnel tests. The precision of the simulation results depends on the application of boundary conditions and model assumptions. Therefore the simulation should always be validated with a wind tunnel or track test.

1.7 Research goal

The main question of this master thesis is: "How can the geometry of an elongated bluff body be optimized in order to reduce the aerodynamic drag coefficient?"

To answer this high-level question, sub questions are defined and listed below.

- How does front elongation a bluff body influence the aerodynamic flow behavior, in terms of suction and pressure forces, when the front of a full scale model is elongated with 500mm?
- What influence does a variation of the front edge radius have on the suction and pressure forces on an elongated bluff body?
- What are the key design parameters (radius, ellipse fillets, slanted surfaces, etc) for the front design which lead to a low drag coefficient?

Understanding the flow behavior of the GETS model will help to create a low drag design for current and elongated heavy-duty trucks. This can reduce the fuel consumption and thereby reduce the CO_2 emission of heavy-duty trucks in the future. Ultimately, these low drag designs will contribute to the climate goals of the EU.

1.8 Report structure

The research questions will be answered by validating the simulation results, analyzing a full scale model and investigating the effects of an elongation. The next chapter will elaborate on the numerical setup. Chapter 4 describes the validation of the numerical simulation using wind tunnel data performed by Van Raemdonck [31]. After the validation the model is scaled to a $1:1$ ratio, this allows for more realistic interpretation of the simulation, as described in chapter 5. Chapter 6 explains the effect of elongation and shows the effect of several front designs. The last chapter will cover the conclusions.

2

BACKGROUND

In this section an overview of the important literature will be given. First general aerodynamic flow around bluff bodies will be explained. The second part deals with the several important studies for aerodynamic development of HDV. The final part will discuss the aerodynamic of specific front designs.

2.1 General flow around bluff bodies

The flow around bluff bodies is characterized by a thick boundary layer and regions of separated flow. This is shortly discussed in section 1.4. It is shown that the flow around bluff bodies is considered to be turbulent due to a high Reynolds number, large pressure gradients, flow irregularities and surface irregularities. This will eventually cause the flow to separate at some point at the truck's surface. The critical locations at which separation can occur are detailed structures and sharp edges. In general, flow at the front edge is prone to separation and flow at the rear will always separate with the current CoE and trailer designs. Separation at the base of the vehicle creates a large low pressure area. In this region, the flow is unstable and produces asymmetrical vortices as is visualized in figure 2.1 [25]. The two larger vortices are trapped in a shear layer.

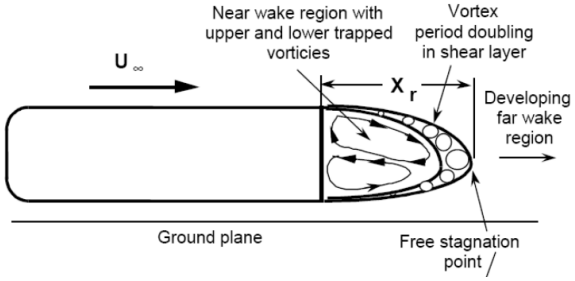

Figure 2.1: Schematic representation of the wake region of the bluff body. Two counter-rotating vortices formed at the base of the vehicle.

2.1.1. BOUNDARY LAYER DEVELOPMENT

The boundary layer is the small layer between the object and the undisturbed flow. Outside the boundary layer the flow is considered uniform and stable, while inside the boundary layer the flow properties change greatly. The boundary layer development is dependent on the flow properties, the shape and the material properties of the object facing the viscous flow. The thickness of the boundary layer increases with surface length and surface irregularities. At the surface of the object the velocity of the flow is zero while just outside the boundary layer the flow velocity is equal to the free stream velocity. The velocity gradient perpendicular to the surface can be represented as a velocity profile, as shown in figure 2.2 [39].

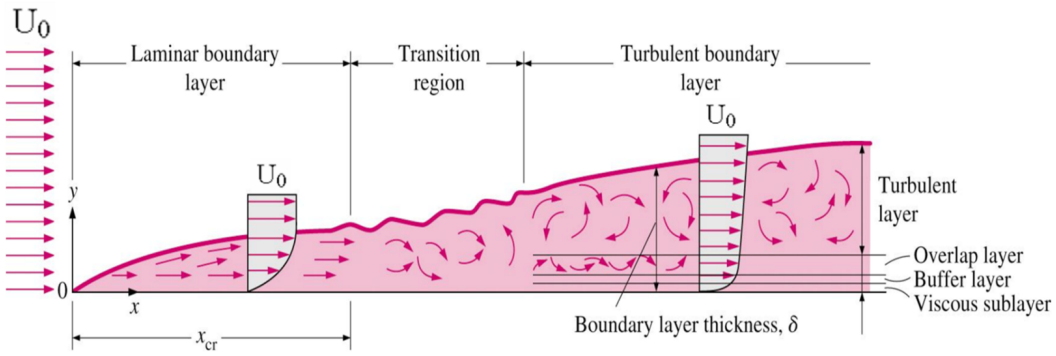

Figure 2.2: Typical boundary layer development: the flow starts laminar and transitions to a fully turbulent boundary layer as it growths thicker.

The boundary layer starts thin and laminar, after a certain length the boundary layer becomes turbulent. Typically for a flat plate this occurs at a Reynolds number of $5 * 10^5$ [40]. The average velocity profile is shown for the laminar and the turbulent region in figure 2.2. The velocity profile in the turbulent case is different due involvement of fast moving particles, which are further away from the wall and move into the lower regions of the boundary layer. The turbulent boundary layer can be subdivided in three regions. The layer closest to the wall is the inner layer, in this part the viscous shear forces are dominant. This layer is followed by a buffer layer and an outer layer. In the buffer layer both viscous effects and turbulent effects are important and in the outer layer turbulent effects are dominant. A distinction between these layers can be used to simplify the numerical simulation process, this is explained in section 3.6.

2.1.2. REYNOLDS NUMBER EFFECT

The Reynolds number is a parameter of the flow which represents the ratio of the inertial forces over the inviscid forces [41]. It is given by equation 2.1:

$$Re_A = \frac{inertial forces}{viscous forces} = \frac{u\sqrt{A_f}}{\mu}, \tag{2.1}$$

where Re_A is the Reynolds number based on the frontal area, u is the maximum relative velocity of the vehicle with respect tot the fluid, A_f the frontal area and μ the kinematic viscosity. At low Reynolds numbers viscous forces are dominant and the flow is laminar. Turbulent flow occurs at high Reynolds numbers and is dominated by inertial forces. The latter is characterized by instable, chaotic flow with vortices.

Studies by [42], [4], [43] and Wood [3] showed that the drag coefficient is dependent on the Reynolds number. As shown in figure 2.3, the C_D is relatively high at lower Re. The C_D drops steeply around the transitional Re number. In the final stage, the transcritical stage, the drag coefficient stays more or less constant.

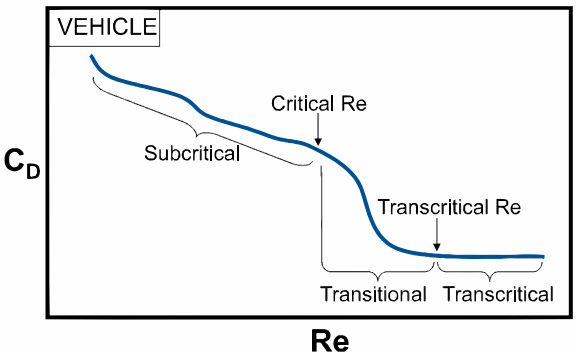

Figure 2.3: Reynolds number effect according to Wood [3]

When smaller scale models are compared to full scale models it is important that the wind tunnel experiments and simulations are performed in the transcritical region. In this region the value of the C_D is almost constant with increasing Re. Thereby ensuring that the obtained results replicate the full scale configuration.

2.2 Previous works

This section will elaborate on several important studies regarding aerodynamic effects of bluff body designs. Many studies emphasize the holistic approach to optimizing the total vehicle C_D, instead of just focusing on the front or rear part [10, 15, 27]. First the relations of Hoerner will be explained, subsequently other important studies will be explained in this section, like the studies performed by Götz, Nakaguchi, FAT and the Supertruck program.

2.2.1. HOERNER'S RELATIONS

Hoerner experimentally determined the drag and lift coefficient of a large variety of objects. He suggested that the base drag is dependent upon the vehicle's fore body drag [27]. The boundary layer acts as an insulator for the oscillating vortices at the trailing edge. The boundary layer can thus reduce the base and total drag. The thickness of the boundary layer is dependent on the fore body drag. By testing the drag of 2D and 3D objects, Hoerner derived two equations. The 2D relation is shown in equation 2.3 and the 3D relation in equation 2.2. These relations are also shown in figure 2.6(a), where C_{P_b} represents the base pressure drag and $C_{Df,b}$ the fore body drag coefficient.

$$C_{P_b} = -\frac{0.029}{\left(C_{Df,b}\right)^{\frac{1}{2}}} \tag{2.2}$$

$$c_{P_b} = -\frac{0.135}{\left(C_{Df,b}\right)^{\frac{1}{2}}} \tag{2.3}$$

For objects where the fore body drag contributes very little to the total vehicle drag, the total drag can be decreased by increasing the fore body drag. When the fore body drag is plotted versus the total drag coefficient, there is an optimal fore body drag coefficient. This is called Hoerner's drag bucket, shown in figure 2.6(b). Studies by National Aeronautics and Space Administration (NASA) refined Hoerners relationship, which is covered in section 2.2.3.

Hoerner [27] suggests that a thin boundary layer at the side of a bluff body is responsible for more negative pressure in the wake than a thick boundary layer. This implies that a well formed fore body, creates a thin boundary layer, which will result in lower pressure at the back of the trailer. A front which creates thick boundary layers will result in higher back pressure coefficients. This phenomena is studied in detail by Mariotti, which is outlined in the next section.

2.2.2. MARIOTTI

The relation between the boundary layer thickness and the base pressure of Hoerner is replicated for 3D flow by Mariotti et al. [44]. Mariotti experimentally investigated the thickness of the boundary layer on an axis symmetric body with an elliptical nose and a sharp edge base. The bullet shaped model was constructed with a diameter-to-length ratio of 0.175. The free stream turbulence level was set to 0.9% and the Reynolds number at $5.5 * 10^5$. The pressure measurements were recorded using pressure taps and the velocity field was outlined through hot wire anemometry.
Using emery cloth to modify the thickness of the boundary layer, it was found that an increase in boundary layer thickness increases the width and length of the recirculation zone. Furthermore the velocity and the fluctuation in velocity reduce while the base pressure increases with increasing boundary layer thickness. The author appoints the lower velocities at the point of separation as the cause of a lower base drag, this is shown in figure 2.4.

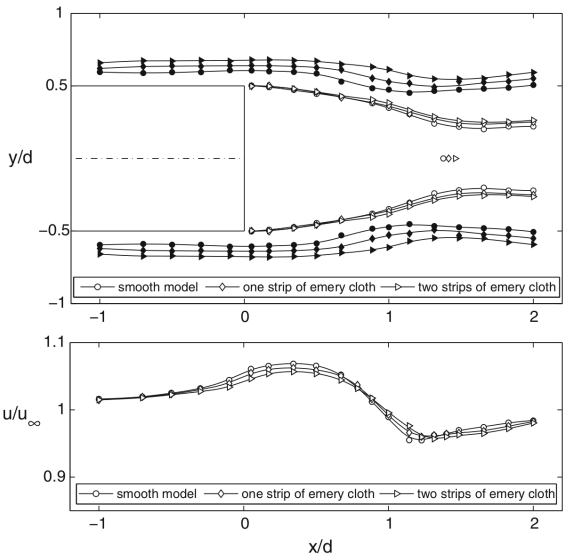

Figure 2.4: Boundary layer study on a bluff body by Mariotti. In the top figure the variation in boundary layer thickness is shown for the three different models. In the bottom figure the velocity distribution along the edge of the boundary layer and of the near wake is shown.

2.2.3. NASA STUDIES

Before the oil crises in the early 1970s, road vehicle shapes were dominated by box shapes. On the onset of the crises, NASA performed full scale experiments in order to optimize the shape of vans by means of coast-down techniques [28]. Although the tests were performed for a box-shaped vehicle, the authors state that the same results hold for heavy trucks and buses. In figure 2.5(a), the baseline model with sharp edges and the optimized model are shown. The model with a truncated tail, rounded edges and a smooth under body reported the lowest C_D value, as shown in figure 2.5(b).

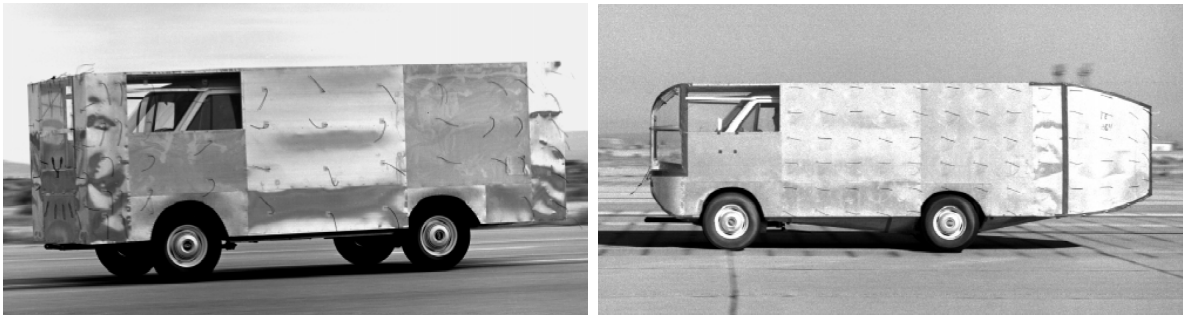

(a) NASA baseline vehicle (model A), C_D=0.89

(b) Optimized NASA test vehicle (model H), C_D=0.242

Figure 2.5: Two of the test vehicles used by NASA to investigate the aerodynamic effects of, among others, a rounded front and boat tail.

In addition to the coast-down test NASA also investigated Hoerner's equations [27], see equation equation 2.3 for a 2D model and 2.2 for a 3D model. The experimental data revealed that Hoerner's formulas underestimate the dependence of base drag on fore body efficiency for road vehicles. The NASA researchers noticed an increase in base pressure at the rear from 0.1 for the baseline vehicle to 0.3 for the aerodynamically optimized van. The gains of streamlining the front is partially offset by the increased base pressure. In order to fully realize the potential of a streamlined front design, the after body design should be more refined.

The authors proposed a new factor as nominator in Hoerner's equation, indicated by the letter '*K*'. The new nominator, the original 2D and 3D equations of Hoener are shown in figure 2.6.

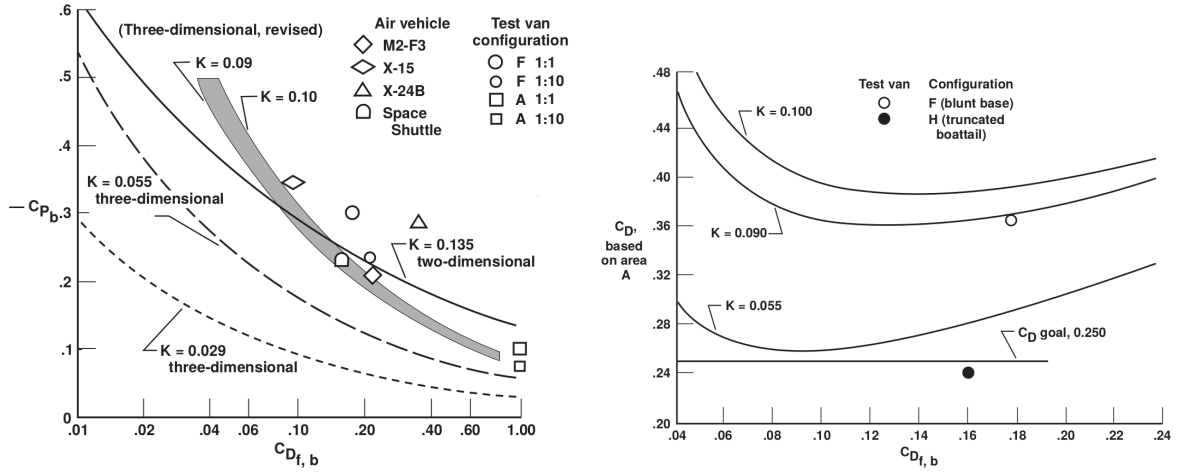

(a) The relation between base pressure and drag coefficient according to Hoerner's (2D and 3D) equations and the measurements of the NASA Dryden research.

(b) Total drag for 3D bodies, using Hoerner's equation. The figure is an edited version of Hoerners equation by Saltzman [45]

Figure 2.6: Hoerners 2D and 3D relations; the drag of the fore body is shown in relation to the drag of the base (left) and the total drag (right). The measurements reveal that Hoerners equations indeed show a qualitative relation, though for a quantitative analysis, the Hoerners equation can not be used.

GÖTZ

Götz showed the effect of rounding the front edge radius combined with slanting the roof. The results are shown in figure 2.7(a). For all the configurations the rounded edges opposed to the squared edge give a large

reduction in C_D . By adding a large boat tail, even larger reductions can be realized. Note that with a poorly designed front, the reduction achieved by adding a boattail is not very strong.

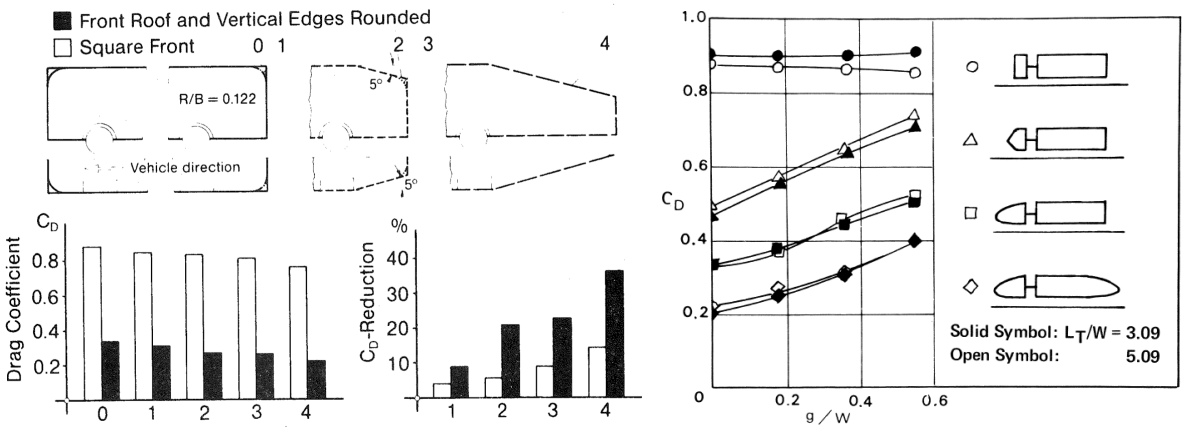

(a) Results of the study performed by Götz

(b) Results of the study performed by Nakaguchi

Figure 2.7: Studies by Götz and Nakaguchi on 3D bluff bodies in the 1980s. The results show that rounding the front edge and boat tailing reduces the C_D significantly.

NAKAGUCHI

In figure 2.7(b) the results of Nakaguchi are shown. The effect of different front and rear designs of a simplified CoE model is studied while the gap ratio is changed [46]. These 3D models are tested in the wind tunnel at a Reynolds number of $1.7 * 10^5$. The results reveal that a long rounded nose in combination with a long boattail results in the lowest C_D . Again the decrease in C_D is amplified when a low drag front and a low drag rear are combined.

DIEBLER

In 2000 Diebler at the NASA Dryden Research facility gained a renewed interest in the formulation of Hoerner's equations on larger scale vehicles [29]. Therefore a Ground Research Vehicle (GRV) has been developed to study the base drag relationship on full scale vehicles. The GRV is a bus shaped model of 13 m long, 2.1 m wide and 2.7 m tall, the Reynolds number equals $3 * 10^7$. The vehicle has square corners and is tested in two configurations, one with an exposed under body and one with an enclosed under body. For both configurations the total error in C_D between the measurement and the 2D Hoerner equation is within 4%. However, the base drag values are off by 70% compared to Hoerner's 2D base drag model and 600% for the 3D model. The author believe that the chaotic fore body flow of the GRV model causes the large errors in the base C_D and more research with a rounded edge GRV is recommended.

WOOD

Wood states that the ability of the flow to follow the boat tail surface depends on the boundary layer state, the thickness of the boundary layer and the base area size compared to the boundary layer [3]. The non-dimensional boundary layer thickness, δ_A, is the ratio of the boundary layer thickness (just upstream of the boat tail) to the square root of the base area. Based on the published data of other studies Wood summarized that the drag reduction capacity of a boat tail is reduced as the non-dimensional boundary layer size increases. The effectiveness of a boat tail is thus dependent on the aerodynamic performance of the all the parts upstream the boat tail.

2.3 Front design

This section discusses the aerodynamic effects of altering certain aspects of the front of the truck. First general tractor designs are discussed, followed by a the front edge radius section. Next, several topics like the effect of front nose elongation, roof fairing, a-pillar positioning, mirror and bumpers will be elaborated on.

2.3.1. GENERAL TRACTOR DESIGN

The basic tractor design has been studied by many, among them are Gilhaus and Götz. Multiple configurations, the influence of the Re number and edge rounding were investigated. Gilhaus studied the effect of the cab shape on 1:5 scale trucks in a wind tunnel [42]. A simplified cab and trailer were used to establish the drag coefficient of different cap designs. Götz studied the influence of rounding of the front, side and rear edged of bluff bodies. Götz and Gilhaus concluded that the radius of the leading edge of the bluff body has significant influence on the drag coefficient. Both studies found that with a rounded front edge the C_D is almost the same as with as 'Stormfront' configuration, shown in figure 2.8(b).

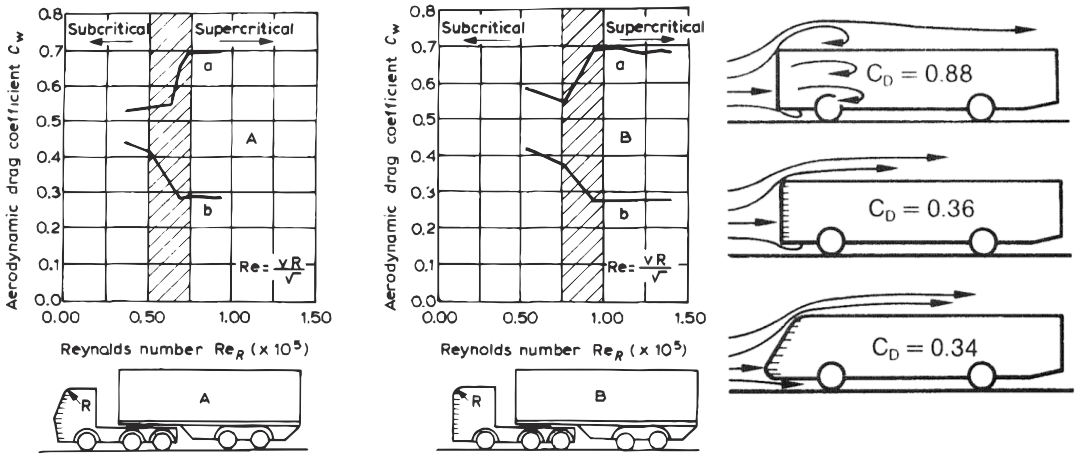

(a) Results of the study performed by Gilhaus

(b) Götz models, squared edge at the top, rounded front edge in the middle and the 'stormfront' below.

Figure 2.8: Basic front end designs studied by Gilhaus and Götz.

2.3.2. FRONT EDGE RADIUS

Rounding the front edge has a large influence on the C_D of the vehicle. This is shown in multiple experiments of [47], [4], [21] and [43]. Götz tested multiple simplified truck and bus shaped models in a windtunnel and determined the drag coefficient of different radii. Cooper [4] also showed that the Reynolds number and thus the velocity of the vehicle determined the optimal front edge radius. This is shown in figure 2.10. The non dimensional radius equals the radius divided by the square of the frontal area. It is concluded that rounding the front edge can reduce the C_D upto a point, after which it virtually stays constant. At this optimal front edge radius the flow at the leading edge is fully attached. Further increasing the radius will not result in a significant C_D reduction. This relation can also be described analytically with equation 2.4, which gives the minimum radius for which the flow will be attached:

$$R_{min} = 1.3 * 10^5 \frac{u}{u_\infty} \tag{2.4}$$

where R_{min} is the minimum radius, μ represents the viscosity and u_∞ the velocity of the oncoming flow. In figure 2.10 it is indicated that a larger non-dimensional radius requires a larger Re (velocity) in order utilize to the full aerodynamic potential.

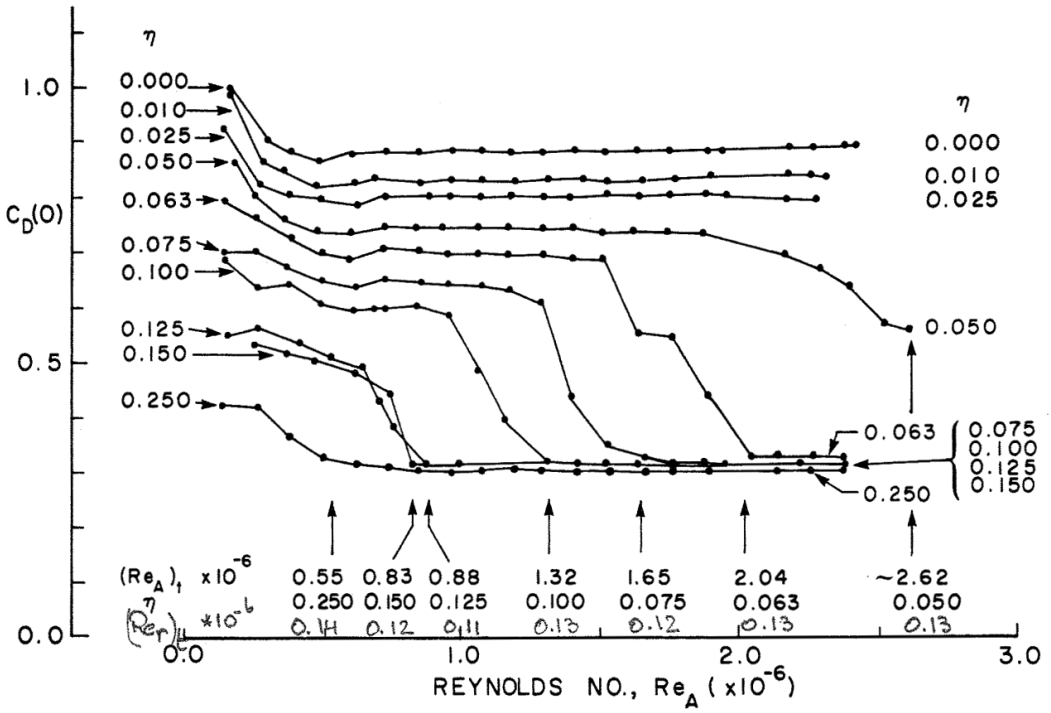

Figure 2.9: The C_D of multiple front edge radii were tested at different *Re* (velocities) [4]. For a given *Re* an minimal radius exist after which the drag coefficient does not decrease anymore.

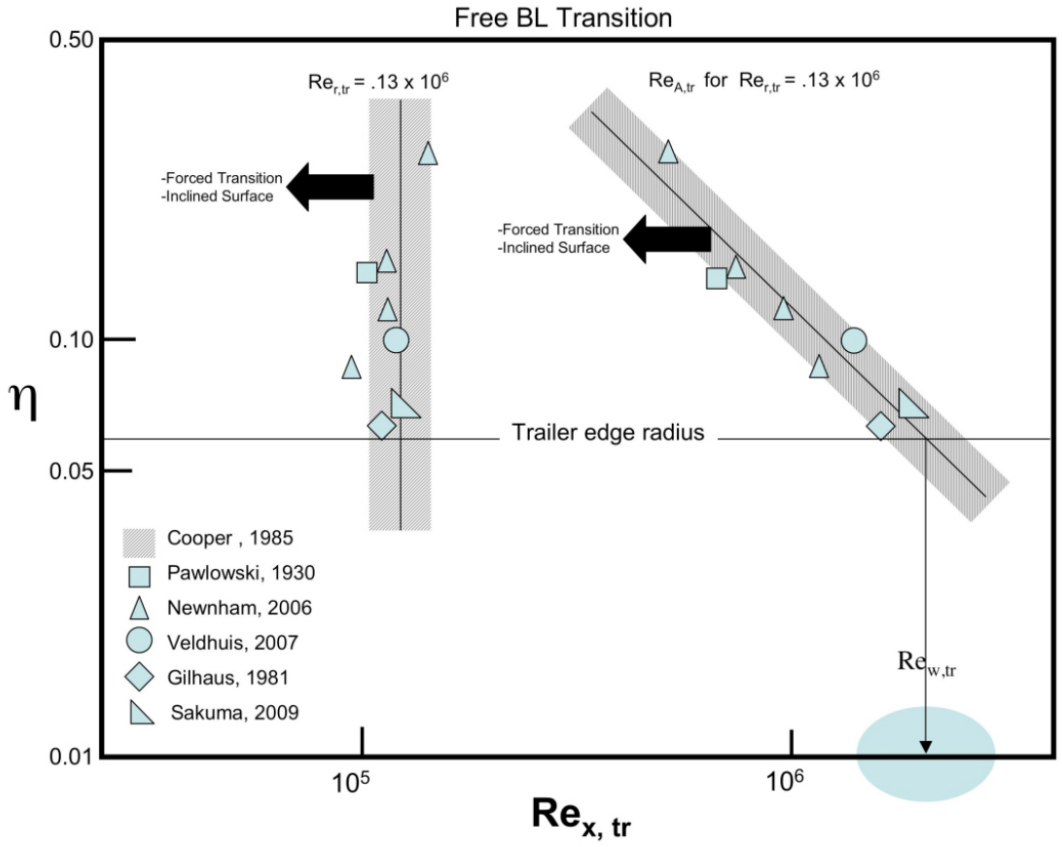

Figure 2.10: Comparison of front edge radius data with Cooper design boundaries.

It is noted that the difference between subcritical (decreasing C_D) and transcritical (low constant C_D) is large and that after the critical radius no change in C_D is observed. However, from figure 2.9 it can be concluded that with increasing radii a very small decrease in C_D has been measured. This phenomena is confirmed by the data of Newnham [21].

2.3.3. WOOD

Wood analyzed the findings of Cooper and others, which is shown in figure 2.10. The dataset shows that with an increasing non-dimensional radius η the $Re_{cr,A}$ and the $Re_{tr,A}$ are reduced proportionally. The gray area on the left indicates the critical Reynolds number of $1.3 * 10^5$ for modern trucks. The critical Re for a η of 0.06 is thus equal to a $Re_{tr,A}$ of $2 * 10^6$ as indicated in the figure.

2.3.4. HENNEMANS

Hennemans [22] studied the influence of the transition point from laminar to turbulent flow on an axis symmetric cylindrical bluff body. The front edge radius, η, is varied between 0.025 and 0.1. Furthermore the turbulence level is varied between 0.08 and 5%. The experimental results are shown in figure 2.11. In this study 'r' is the front edge radius and 'D' represents the diameter of the model. The Reynolds number effect for the small radii is not found. At the largest radius (0.1) the Reynolds number effect is found, however, it is more gradual than the result of Cooper. Furthermore, the author concluded that the turbulence intensity largely influence the C_D, especially for larger radii.

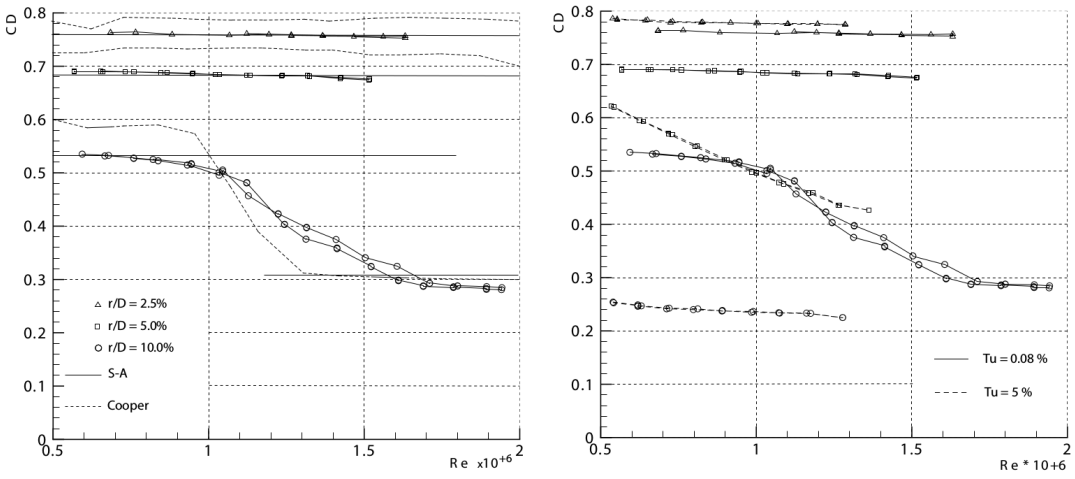

Figure 2.11: Results of the Reynolds number effect for different front edge radii, performed by Hennemans.

2.3.5. SAKUMA

Sakuma et al [48] investigated flow separation around the front of a 1:5 scale vehicle model, using a Reynolds number of $1.9 * 10^6$ based on the width. The pressure distribution, flow behavior and aerodynamic drag of various front edges shapes and size were measured. The baseline model shows great similarities with the GETS model developed by van Raemdonck. The main findings are summarized in figure 2.12.

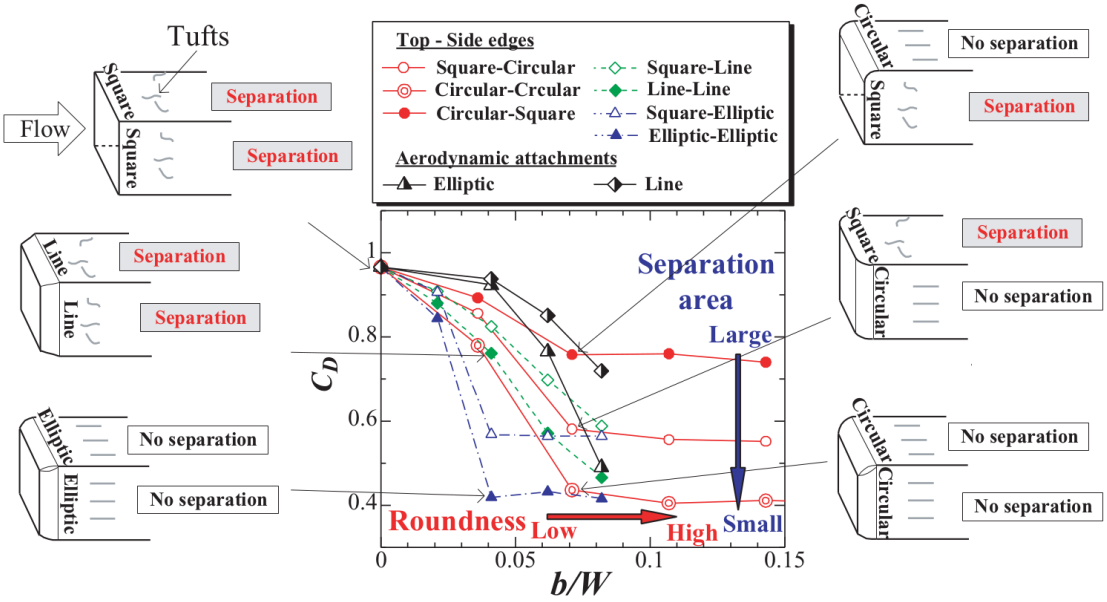

Figure 2.12: Summarizing chart of the results obtained by Sakuma. The size of the front-end edge design is varied in a non-dimensional parameter a/W and b/W. Where a indicates the longitudinal direction, b the lateral direction and W the width of the model.

The authors conclude that the C_D value decreases when the number of rounded edges at the front is increased. The length of the elliptical arc in longitudinal direction can be shorter compared to that of a circular arc for the same C_D values. The most effective shape of the front-edge is an elliptical shape; the size of the arc should at least be greater than b/W=0.04 and a/W=0.07 to prevent flow separation.

2.3.6. FRONT NOSE ELONGATION

Front nose elongation might increase the aerodynamic efficiency of a heavy-duty truck. A few studies have been performed on this subject, among them are the Scania 'SN', a study by the German FAT organization and a more recent study by Martini.

SCANIA

In 2004 Scania was one of the first to study the effects of a SN model using CFD and the German-Dutch Wind Tunnels (DNW) [49]. By means of an elongation of 1000 mm an improvement of 1.2% in fuel economy was claimed with respect to the reference truck. However, no peer-reviewed records of these SN models studies are published and hence the claimed improvements can not be verified. The SN models are shown in figure 2.13. It is noted that the difference between the 500 mm elongated model and the 1000 mm elongated model is only 4 drag counts, while an improvement of 18 drag counts was realized between the reference truck and the 500 mm elongated model.

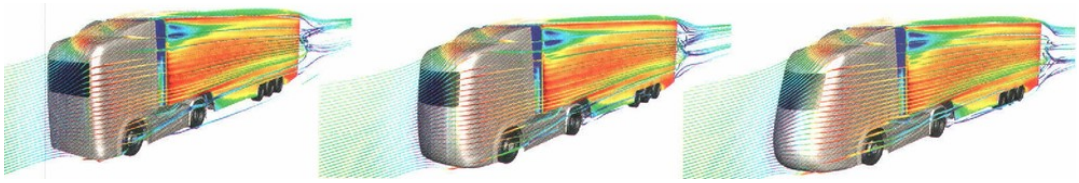

Figure 2.13: Scania SN variants: a reference truck is shown on the left, a 500 mm elongated SN in the center and a 1000 mm SN on the right hand side [5].

FAT STUDIES

The German FAT organization conducted extensive testing regarding the front elongation of a generic European truck [43]. The simplified model used in the study is a blend of three models from different tractor manufacturers (Daimler AG, Iveco and MAN). The base model, SN and an elongated were tested in the wind tunnel of Daimler AG. Furthermore, the flow around the models was simulated numerically. The models are shown in figure 2.14.

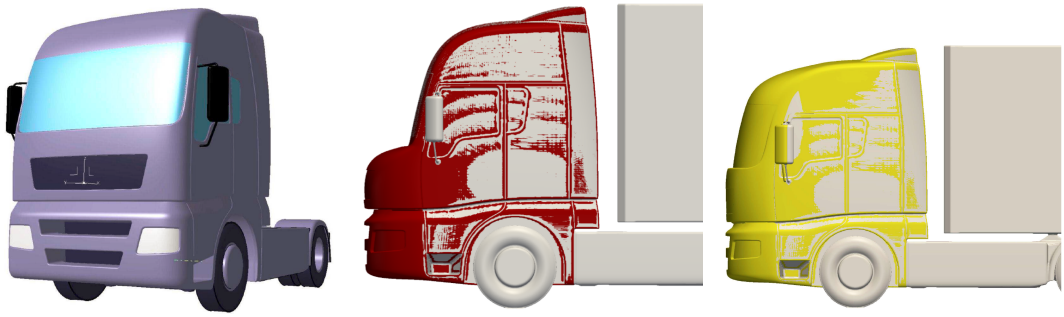

(a) Baseline model (b) SN model (c) Elongated model

Figure 2.14: Models of the FAT study.

Using smoke, it was concluded that the flow remained attached until a quarter of the trailer, after which it separated. This was observed in the wind tunnel and in the numerical simulation. The simulated results show a decrease in drag of 7 Drag Counts (DC) for the SN variant and 13 DC for the elongated variant. According to the authors, the reduced drag is a result from the larger corners radii. In the baseline model the radii varied between 20 mm (on the bottom of the truck and the side front edge) and 150 mm (at the top front edge). The front edge radii of the elongated variant was kept between 85 mm and 800 mm. The SN model uses the same radii as the elongated model on the elongated part, while at the upper part the radii of the baseline model is applied.

The pressure profiles show a reduction in pressure at the front of the vehicle. The suction forces at the front edge corner decreased in magnitude. However, this latter effect is less than the decrease in pressure at the front of the vehicle. The authors further notice that the flow velocity on the sides increase less than at the reference vehicle. Furthermore, in side wind conditions the aerodynamic drag was slightly lower compared to the reference model.

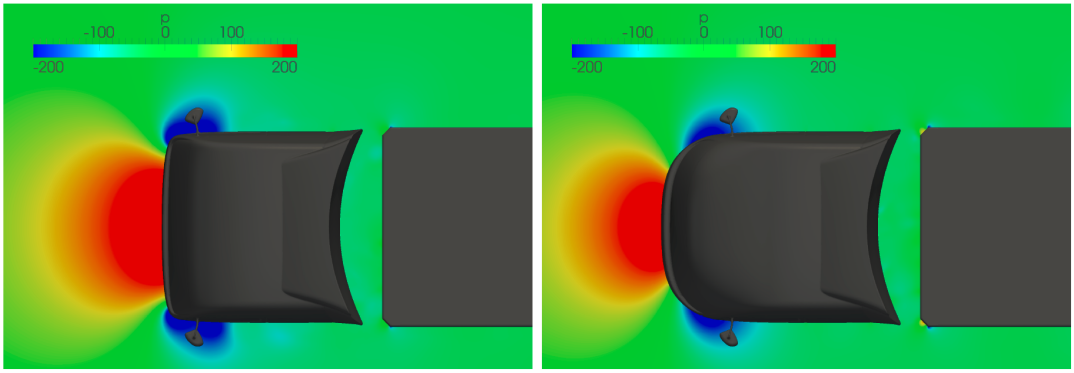

Figure 2.15: Comparison of pressure profile in XY plane, Z = 0 m, p = m^2/s^2 between the baseline model and the front elongated model. The magnitude of both the pressure and suction forces in the elongated model decreased.

In table 2.1 the DC differences in C_D are shown with respect tot the reference model. The decrease in drag coefficient at the truck for both the SN as the pure elongated model are counteracted by the increased drag coefficient at the trailer and the motor. In the simulation the cooling is included in the motor compartment.

Model	Truck	Trailer	Motor	Total
Softnose	-26	16	3	-7
Elongation	-44	27	4	-13

Table 2.1: Results of the FAT study; drag count difference for 0 degree yaw at 22 m/s

The FAT also studied the effect of a SN and a front elongation truck in combination with a boat tail in the wind tunnel and with CFD. A drag reduction was realized of 12.5% for the combination of the 400 mm and

the elongated front design. While only a front elongation provided a reduction of 4.5% and only a boat tail a reduction of 9.5%. The authors concluded that the boat tail of 400 mm performed roughly the same as a boat tail of 800 mm or 1200 mm.

MARTINI

Martini investigated the influence of an SN elongated CoE detailed Volvo truck using CFD. The truck is simulated at full scale with a velocity of $22 m/s$. Elongating only the grill area is referred to as a SN. Where soft implies that the structure should be deformable to minimize injuries in case of a crash. Two SN models were investigated, a 200 mm and a 500 mm elongated model. Martini observed a reduction of 23 drag counts for 200 mm at 0 degree yaw and a reduction fo 38 drag counts delta for 5 degree yaw. For the SN of 500 mm the results were more pronounced: a 33 drag counts reduction for 500 mm 0 degree yaw and a 55 drag counts reduction at yaw angle of 5 degrees. Especially in side wind condition the benefits of a SN are significant. In order to explain these results Martini visualized the flow velocity in the yawing condition, these are shown in figure 2.16.

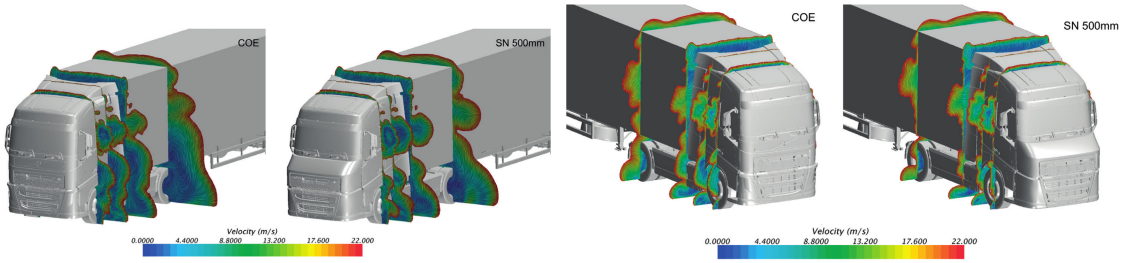

(a) Leeward side (b) Windward side

Figure 2.16: Planes of velocity magnitude at different locations along the vehicle for 5 degree yaw for both the baseline CoE and SN model

The planes of velocity magnitude reveal that in the windward side the nose redirects the flow significantly in the mirror region. The separation areas increased in the SN variant. However lower velocities at the chassis can be observed. The windward side of the vehicle also shows significant differences in flow structure. The differences around the mirror area are not as pronounced as on the leeward side. The losses at the chassis level were reduced with the SN The same trends were visible at 0 yaw, though less significant in size.

TRACTOR ROOF FAIRING

Gilhaus [42] investigated the use of wind deflectors on the roof of the cabin for CoE truck. Gilhaus concludes that the wind deflector must ensure that the flow does not separate and that the front of the roof deflectors is very close to the edge of the cab roof. Leuschen [32] investigated several drag reduction devices in the wind tunnel of the National Research Council of Canada (NRC) on a US truck. The author concludes that the roof fairing should be developed in conjunction with a sun visor. A fairing on top of the trailer provides little additional benefit when a cab-roof deflector is present. When this is not present a leading edge fairing can provide fuel savings. Martini also investigated the effect of tractor roof fairing for a CoE truck [50]. The effect of only a roof fairing can be upto 35 drag counts and up 50 drag counts when the roof fairing is combined with side fairings, at zero degree yaw.

A-PILLAR POSITIONING

In the US an extensive collaboration between the government and the industry led to the Supertuck project. The project investigated a lot of aspects of the truck and trailer, one of them is the a pillar position. In figure 2.17 two concept trucks are shown. The left is an aerodynamically optimized concept, while the right also incorporates the pillars of the baseline truck, which is a Cascadia truck. CFD simulation showed that the increase in C_D between the two pillar locations is roughly 1%. No further explanation was provided.

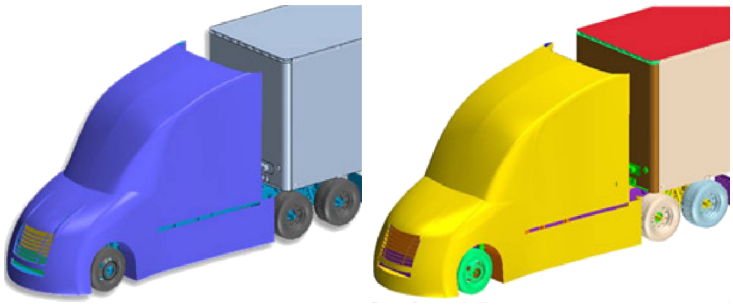

(a) Supertruck concept with inward a-pillars

(b) Supertruck concept with conventional positioned a-pillars

Figure 2.17: Supertruck a-pillar study. The aerodynamic penalty of more outer positioned (right) a-pillars was roughly 1% compared to the more aerodynamic concept on the left.

MIRRORS

The effect of mirrors is studied by the FAT. A baseline model, a SN model and a 500 mm front elongated model are studied in the wind tunnel and with CFD. These models are shown in figure 2.18. In the baseline model the mirror causes the flow to separate around the side of the truck-trailer combination. Without the mirror the C_D is reduced by 0.017.

(a) Numerical simulation

(b) Windtunnel experiment

Figure 2.18: FAT mirror study. Flow separation at the baseline model. Left the numerical simulation, right the smoke investigation in the wind tunnel experiment.

In the front elongated model the effect of the mirror is even larger. Without the mirror the C_D reduces with 0.042. This is due to the fact that the mirrors are in clean air in the elongated truck and in a lower pressure region in the reference truck. For the SN variant the C_D without the mirrors reduces with 0.007. This is less than in the elongated model. The authors reason that the mirror is not in clean airflow, therefore the influence of the mirror is less pronounced. The authors conclude that mirrors can significantly influence the C_D of the vehicle. By switching mirrors for small cameras a reduction in C_D of 10% can be achieved.

THERMAL MANAGEMENT

Thermal management and cooling airflow are important in the truck development. The cooling flow has a direct effect on the aerodynamic performance of the vehicle. Thermal management is investigated by Devasa (FAT study) [43], the Supertuck program [15] and Martini [50]. In the FAT study the cooling package is simulated by means of a porous part. In the elongated model the C_D increases with 0.004, in the SN model with 0.003. When the air intake is covered a reduction in C_D is observed of 0.022 for the elongated model and with 0.019 for the SN model.

Martini [51] compared the effects of cooling between a CFD study and wind tunnel measurements. A wind tunnel test is performed at the NRC, this is compared with several turbulence Reynolds-Averaged Navier-Stokes (RANS) CFD models. The reported difference between a closed grill and an open grill is maximum at zero degree yaw and equal to 4%. At higher yaw angles the effect is close to 2%. The effect on the C_D of a closed grill opposed to an open grill is mainly visible at the front of the cab. In the closed grill case, a steep increase in drag is noticed as a consequence of air hitting the grill, instead of flowing through. However, when

the under-hood region is reached the local drag reduces. This is caused by the eliminated flow through the under-hood that would have otherwise led to a drag increase.

BUMPER

The bumper is one of the many optimization topics of the US Supertruck program. Typically the bumper ramp angle is 15° to accommodate for parking lots etc. This occurs at the cost of an aerodynamic penalty. This aerodynamic penalty is investigated for ramp angles of 15° and for normal bumpers at 15, 8 and 0 degrees. The different bumpers are shown in figure 2.19. The 8 degree bumper decreased the drag by 0.04 the 0 degree bumper increased the C_D with 0.22% and the 15 degree slotted bumper increased the C_D with 0.16%.

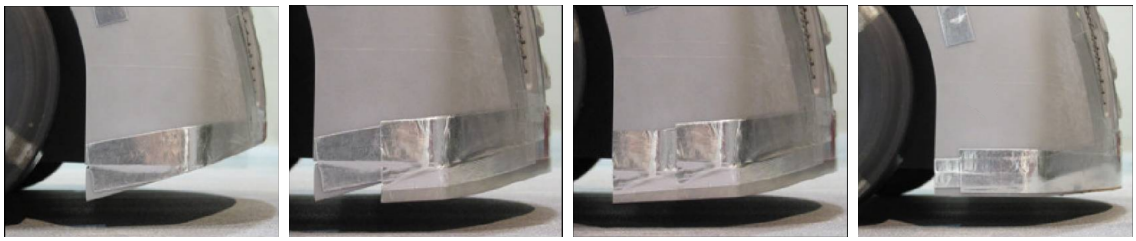

(a) 15° bumper (b) 15° slotted bumper (c) 8° bumper (d) 0° bumper

Figure 2.19: Supertruck bumper variants

The conclusion of the bumper study is that a 15 degree ramp with an air dam down to 8 degrees is the best balance between aerodynamics and practice. It was shown that a bumper air dam in conjunction with tire spats further helps in reducing drag on front tires.

US SUPERTRUCK BASIC TRACTOR SHAPE EVALUATION

The Supertruck team started with a theoretically optimal shape for a vehicle, a streamlined bullet-vehicle without any gaps. In this program the aerodynamic effects of the tractor shapes, the tractor-trailer gap, the cooling system, ground clearance, under body aerodynamics and more are studied. After a parametric study one, the Cascadia front, the bullet front and three boat tails were studied. The results of these CFD simulations are shown in figure 2.20.

The aerodynamic effect of three boat tails is investigated on different vehicles. A long, medium long and a short tail were fitted on three models; a bullet shaped font with low ground clearance, a bullet shaped front with normal ground clearance and an optimized Cascadia tractor. The results are shown in figure 2.20. The drag is measured for four yaw angles. The C_D between the three models is significant. Note that the length of the tail on a Cascadia model does not change the C_D significantly.

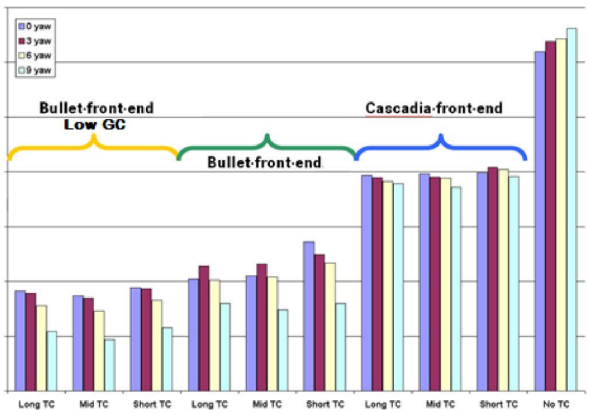

Figure 2.20: Aerodynamic performance of basic tractor and boat tail shapes, on the vertical axis no units area published.

The conceptual study with the bullet shape showed that a significant drag reduction was possible. The next step in the study was to translate these findings to a more conventional shaped truck in order to satisfy

other requirements. CFD was used to analyze several basic tractor shapes, of which two are shown in figure 2.21.

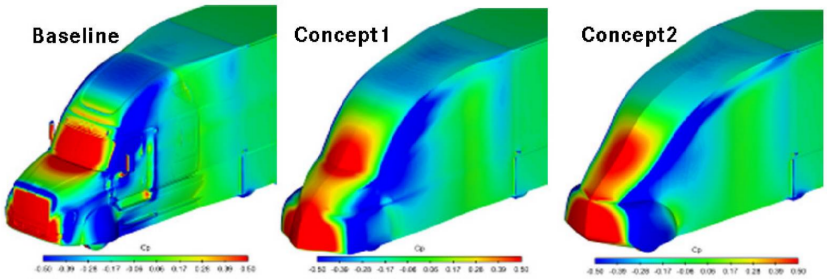

Figure 2.21: C_P distribution on three models of the Supertruck concepts in phase 1

Refinements and recommendations were made on the first two basic tractor shapes. The refinements include a more detailed hood and window shapes, the new tractors are shown in figure 2.22.

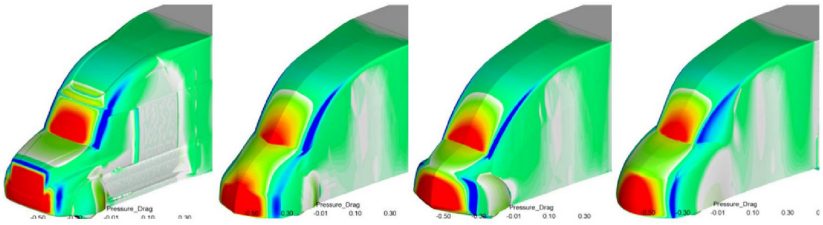

Figure 2.22: C_P distribution on three models of the Supertruck concepts in phase 2

Figure 2.22 shows the pressure drag, with in red color the positive pressure (drag) and in blue the negative drag (suction). An important difference between the first two models and the third is the rounding of the bumper, the hood and the sides (near the wheels). From figure 2.22, it is clear that the pressure (red) area is much smaller than the baseline model, but also smaller than the first two concepts. In particular at the nose of the truck, less pressure drag occurs. The CFD results show a larger drag reduction for concept 1 than for concept 2. Concept 3 achieved the most drag reduction. The concepts were tested at 0° and 6° degrees yaw.

The final conclusion of the Supertruck program states that an drag reduction of 54% has been achieved over the baseline model. 15% is due to the tractor contributions and 39% due to trailer contributions.

2.4 Truck trailer combinations in the EU and US

Legislation limits the maximum length of vehicle combinations in a different way for the EU and the US. In the US the length of the trailer is fixed, whereas in the EU the tractor-trailer combination is fixed. The European legislation, Directive 96/53/EC, led to the development of the CoE tractors. These cabs have a flat front opposed to the conventional trucks with a hood used in the US. Furthermore the lower maximum velocity means that aerodynamics has less of an impact in the EU. In figure 2.23 the two different models are shown.

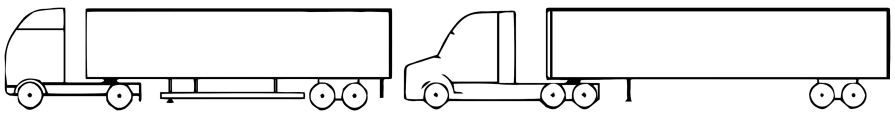

Figure 2.23: Sketch of typical USA and EU trucks

According to Hjelm the difference in terms of drag coefficient between a conventional and CoE truck is around 0.05 [52]. This difference is a consequent of the limited design freedom for EU trucks. Although, the benefit of the US trucks is counteracted by the usually larger gap between the truck and the trailer.

Currently, in the EU a trial started in 2016 where longer truck trailer combinations are allowed. Fuel consumption and the logistic system could benefit from these longer combinations.

3

NUMERICAL SETUP

This chapter describes the numerical setup of all the numerical simulations performed in this thesis. First the computational domain, the boundary conditions, the model and the CFD settings will be explained.

3.1 Navier-Stokes equation

The Navier-Stokes equations will be used to simulate the flow around the vehicle. It consist out of the continuity and momentum equation, equation 3.1 and 3.2. The complete derivation is explained in detail by Anderson [53]. The principle behind the continuity is the conservation of mass, the equation is given by equation 3.1.

$$\frac{\partial \rho}{\partial t} + \nabla \cdot (\rho V) = 0 \tag{3.1}$$

The principle of the momentum equation is Newton's second law. This law states that the rate of change in momentum of a fluid particle equals the sum of the forces on that particle. Its main contributors are the body and surface forces. The momentum equation for fluid flow is also known as the Navier-Stokes equation and is given in equation 3.2.

$$\begin{aligned}
\frac{\partial (\rho u)}{\partial t} + \nabla \cdot (\rho u \mathbf{V}) &= -\frac{\partial \rho}{\partial x} + p f_x + (F_X)_{viscous} \\
\frac{\partial (\rho v)}{\partial t} + \nabla \cdot (\rho v \mathbf{V}) &= -\frac{\partial \rho}{\partial y} + p f_y + (F_Y)_{viscous} \\
\frac{\partial (\rho w)}{\partial t} + \nabla \cdot (\rho w \mathbf{V}) &= -\frac{\partial \rho}{\partial z} + p f_z + (F_Z)_{viscous}
\end{aligned} \tag{3.2}$$

3.2 Turbulence modeling

Solving the Navier-Stokes equations completely requires a lot of computational power. Therefore the turbulence of the flow is simplified using a RANS turbulence model and a closure model.

3.2.1. RANS

RANS is a steady-state method, this means that the velocity and pressure components are split into a mean flow and a fluctuation part. Therefore the solution has no time component, this significantly lowers the computational effort. At the Delft University of Technology (DUT) the RANS method is often used in combination with the ANSYS Fluent software [30], [54],[55] [31] [36]. Comparing experiments with the simulated RANS data shows good qualitative agreement, however, the quantitative measurements, like mean velocity profiles

in separated regions can deviate from the experimental data. The quantitative data may not be valid for massively separated flow [56]. A more detailed summary of the numerical approaches which can be used to solve the turbulence models is given by Choi [56].

3.2.2. CLOSURE MODEL

In order to remove the fluctuation part in the RANS equations, a closure model is needed. A closure model describes the fluctuating part as a function of the mean flow. Several different models are available in ANSYS Fluent. According to [57] the Shear Stress Transport (SST) k-ω model provides an optimal balance between accuracy and performance. The variables k and ω represent the turbulent kinetic energy and the specific rate of dissipation [7]. All two equation models like the RANS k-ω model relate the turbulence stress tensor to the mean strain rate sensor, this assumptions is called the Boussinesq eddy viscosity assumption [6]. This assumptions greatly reduces the computation cost and has a major weaknesss: the assumption is valid for simple flow with straight boundary layers and wakes. However, for complex flow with strong curvature or quick accelerating and decelerating flow it is not valid. For bluff bodies, the flow at separated regions are therefore not captured correctly. The overall flow conditions are can be simulated correctly: Veluri and Roy [58] obtained good qualitative and quantitative results with a similar bluff body (Ground Transportation System (GTS) model). Furthermore Nalanagula [59] showed that the SST k-ω has a better convergence than the k-ϵ closure models for a CoE truck.

Veluri and Roy [60] studies the effect of several closure models on the GTS model using ANSYS Fluent software. Which shows great comparison with the GETS model. The models studied are: the standard Wilcox 1998 k-ω model, the SST k-ω model, the standard k-ϵ model and the Spalart-Allmaras model. Drag coefficients, pressure coefficients and flow structures where examined. The authors conclude both the k-ϵ and k-ω SST predicted the drag coefficient close to the wind tunnel experiment. Furthermore, Nalangula [59] concluded that k-ω SST was more robust than the k-ϵ closure model in terms of converging.

3.3 Computational domain

The recommended computational domain size for heavy commercial vehicles is captured in Society of Automotive Engineers (SAE) Guideline J2966 [61] and is therefore used. The computational domain is separated into three main regions: the domain, the outer density box and the inner density box. The different regions are shown in figure 3.1. The relative dimensions are shown in table 3.1. By separating these regions, different cell sizes can be defined. This will save processing time while maintaining accuracy of the solution.

The dimensions of the surrounding density box are chosen such that the most relevant flow phenomena are captured in high detail, such as the wake of the vehicle. Directly on the model a group of layers with structured cells is positioned. These inflation layers are chosen such that the boundary layer is fully captured.

Volume	Relative length	Relative width	Relative Height
Domain	13 * L	12 * W	6 * H
Surrounding box	2,5 * L	L	0,5 * L
Wake refinement	1,6 * L	1,3 * W	1,2 * H
GETS model	L	W	H

Table 3.1: Relative dimensions of the domain and refinement volumes

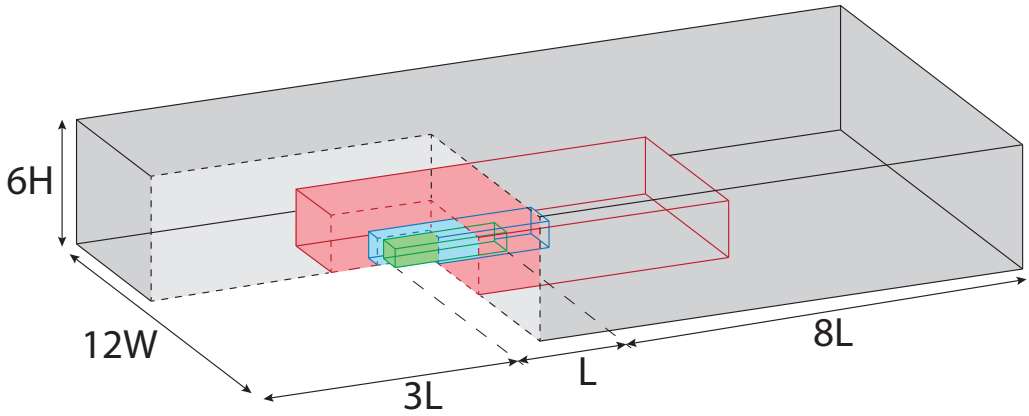

Figure 3.1: Layout of the computational domain, a cut-out in the domain exposes the distinctive volumes. The grey volume is the domain. Inside this domain the surrounding density box (red) and the wake refinement (blue) density boxes are located. The green volume represents the model.

3.3.1. BLOCKAGE RATIO

The blockage ratio is defined as the ratio between the surface area of the model and the cross sectional area of the domain. This is shown in equation 3.3. Hyvarinen [62] concludes that the blockage effect is greatest for separated flows. Blockage effects can be caused by the following: compressed airflow at the sides and top of the model, pressure drop around the vehicle (stronger suction regions at front edges) and a lower base pressure.

$$Blockage\ Ratio \quad = \quad \frac{A_{model}}{A_{domain}} = 1.2\% \tag{3.3}$$

According to Lanfrit [63] the blockage ratio should be sufficiently low to obtain correct results. In the simulations of the GETS model in this thesis the blockage ratio is 1.2%, which is sufficiently low.

3.4 Boundary conditions

The boundary conditions of the domain and vehicle are also set to the industry standard J2966. The boundary conditions for the domain and vehicle surfaces are listed in the table 3.2 and the boundary surfaces are visualized in figure 3.2.

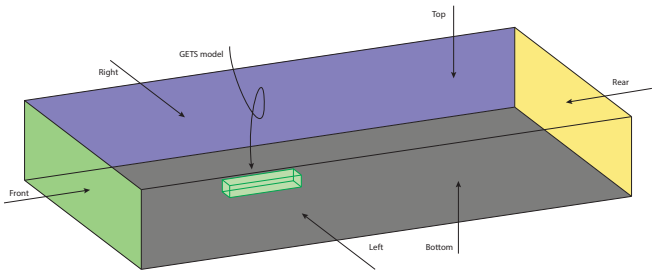

Figure 3.2: Boundary conditions of the domain

Surface	Yaw = 0°	Yaw > 0°
Domain, front	Velocity Inlet	Velocity Inlet
Domain, rear	Pressure Outlet	Pressure Outlet
Domain, left	Symmetry	Velocity Inlet
Domain, right	Symmetry	Pressure Outlet
Domain, top	Symmetry	Symmetry
Domain, bottom	Moving wall	Moving wall
GETS model	No-Slip Wall	No-Slip Wall

Table 3.2: Boundary conditions per surface

At the velocity inlet, the flow enters the domain with a constant velocity. The velocity, the turbulence intensity and turbulent length scale are defined. The turbulence intensity is dependent on the wind tunnel conditions and is defined as the difference between the velocity fluctuations and the average flow velocity [7]. The turbulence intensity in the wind tunnel is 1% [31], therefore this parameter is also chosen in the 1:15 scale model. For the full scale simulation the turbulence intensity is set to 5% which is recommended by Muncrief [11].

The flow leaves the computational domain at the outlet. At the outlet the pressure is constant and the turbulence intensity and length scale are defined. The bottom of the domain is configured as a moving wall in order to simulate a moving road. On the left, right and top surface a symmetrical boundary condition is applied for 0 yaw as recommended by Lanfrit [63]. Symmetrical boundary conditions mean that the flux is zero and thus no flow is passing through that surface and no boundary layer is formed on that surface. This eliminates the need for small structured volumes like prism layers on these surfaces. On the surface of the GETS model, the no-slip wall boundary condition is applied. This means that the velocity component normal to the surface is equal to zero. A boundary layer will form on the no-slip wall, therefore small structured layers are defined to capture the complete boundary layer [7].

3.5 Surface model

The GETS model is a simplistic interpretation of an CoE-truck and specifically designed in order to perform research based on the European semi-trailer combination [64] and is shown in figure 3.3. HDV have a complicated geometry, which can be different for every model. Small but influential components like styling elements, mirrors, mud-flaps, rotating wheels, etc, increase the computational time significantly. Since this study focuses on the general flow behavior around a bluff body there is no need to capture all the details of a real truck. The GETS model is designed in analogy to the NASA GTS model [65]. The front edge radius is optimized according to the experimental results of Cooper [4]. The GETS model is shown in figure 3.4 and the dimensions are listed in table 3.3 for the full scale and wind tunnel scale.

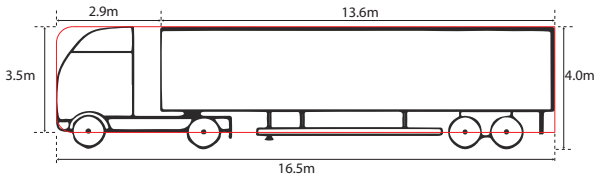

Figure 3.3: Sideview comparison between a sketch of a CoE (in black) and the GETS model (in red).

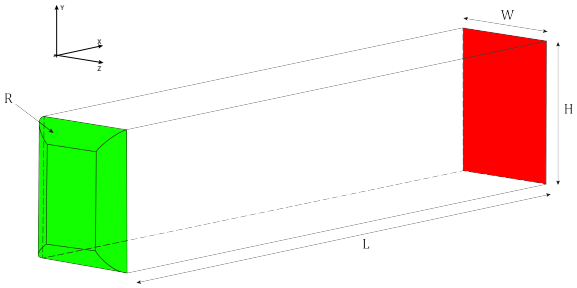

Figure 3.4: GETS surface model, the green color in indicate the front, the red color the rear. The transparent surfaces are the sides

The GETS model contains 10 surfaces as shown in figure 3.4. In green the front is illustrated, it consist out of the following surfaces: front middle, front right, front left, front top and front bottom. The sides are named right, left, top and bottom, these are transparent. In red the rear is visualized. The axis definition in this figure is used in this study.

Parameter	Symbol	1:1 [m]	1:15 [m]
Length [m]	L	16.5	1.1
Height [m]	H	3.5	0.234
Width [m]	W	2.6	0.173
Front edge radius [m]	R	0.54	0.036
Ride height [m]	rm	0.5	0.033

Table 3.3: GETS dimensions

3.5.1. YAW ANGLE TRANSFORMATION

The output of ANSYS Fluent gives the forces and coefficients in the direction of the virtual wind tunnel as visualized in figure 3.5. The x-direction indicates the driving direction, the y-direction the upward direction and the z direction the lateral direction. The angle of attack is set to 0 degrees, the drag and lift therefore align with the vehicle axis. The angle between the direction of the truck and the direction of the air due to the side wind is defined as the yaw angle.

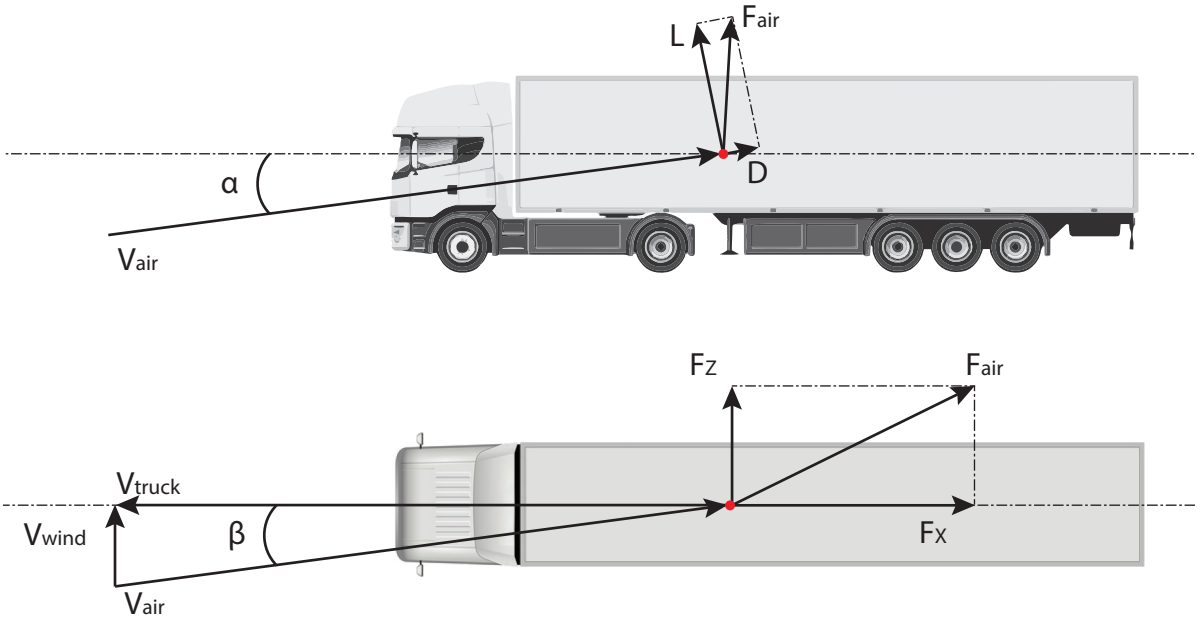

Figure 3.5: Virtual wind tunnel axis to vehicle axis

The drag force and the side force are of primary interest for the aerodynamic performance of the model. These are obtained by using a transformation from wind tunnel axis to vehicle axis, as shown in equations 3.4 [31]. To all the simulation results which involve yaw angles these transformations are applied.

$$C_D = \frac{C_Z * sin(\beta) + C_X * cos(\beta)}{cos^2(\phi) + sin^2(\beta)} \tag{3.4}$$

3.6 Boundary layer and y^+

The flow in the region near the wall of the model is subject to large pressure and velocity gradients. In order to describe these gradients, the dimensionless wall coordinate y^+ is used. In order to simulate the boundary layer with the least amount of computational resources a wall model is used. In figure 3.6 the relation between the boundary layer thickness and the y^+ variable is explained. In the boundary layer three separate regions can be distinguished. In the viscous sublayer ($y^+ < 5$) the Reynolds shear stress is negligible compared with viscous stress. Between the viscous sublayer and the log-law region sits the buffer layer ($5 < y^+ < 30$). For $y^+ > 30$ the log-law is valid and performs well for high Re flows where the turbulent boundary layer is fully developed [6].

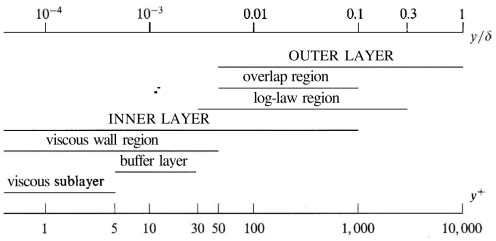

Figure 3.6: Sketch of the various wall regions and layers for a turbulent channel flow at high Reynolds number [6]

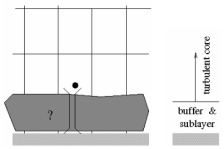

Figure 3.7: Wall function approach according the Fluent manual on the left [7]

This requires a certain height of the first cell layer to be between 30 and 300.

$$y^+ = \frac{\Delta y_p \sqrt{\rho \tau}}{\mu} \tag{3.5}$$

$\Delta\ y_p$ represent half of the height of the first cell, ρ the density of the fluid, τ the friction force and μ represents the dynamic viscosity. The ρ and μ of the fluid are constant, the only variable in this equation is τ. Using equation 3.6, it can be observed that the value of y_p is therefore depended on the local flow velocity.

3.6.1. SKIN FRICTION DRAG

The skin friction drag is simulated using the equation 3.6 and equation 3.7 in which μ is the skin friction coefficient $\frac{du}{dy}$ the velocity gradient in perpendicular to the wall, ρ the air density and u the local air velocity.

$$\tau = \mu * (\frac{du}{dy}) \tag{3.6}$$

$$c_f = \frac{\tau}{0.5 * \rho * U^2} \tag{3.7}$$

The gradient of the velocity $\frac{du}{dy}$ is calculated using the wall functions, this component is the most important factor in these equations because it will vary significantly more than the other parameters.

3.7 Solver settings

ANSYS Fluent is used as the solver and it is configured using the recommendations of Lanfrit [63], the SAE [61] en the Fluent manual[7].

Two types of solver exist in ANSYS Fluent, a pressure-based solver and a density-based coupled solver. The density based solver is in particular useful when a strong coupling between the energy, momentum and/or species exist, for example in high speed compressible flow with shock waves. The pressure-based solver take momentum and pressure as the primary variables and is applicable for low speed incompressible flow to high-speed compressible flow, in particular it is applicable for single phase flows. The SAE J2966 guidelines recommend a pressure-based coupled solver [61]. According to Fluent this results in superior performance in terms of memory requirement and computing time [7].

For the pressure-based solver two algorithms are available in Fluent. A segregated solver, which solve pressure correction and momentum sequentially and a coupled solver, which solves the pressure and momentum simultaneously. The latter yields superior performance and therefore is used in this study. The gradient of the solution variables are required to determine the diffusive fluxes, velocity derivatives and higher-order discretization schemes. These gradients at the cell center can be determined by three approaches of which the Green-Gauss Node is chosen. According to the Fluent manual, this interpolation method is the most accurate and minimizes false diffusion for tetrahedral meshes. Finally the interpolations methods are chosen. For the first 150 iterations the simple solver is used and the first order interpolation method is used for the momentum equation, turbulent kinetic energy, specific dissipation rate and the pressure discretization. For the last 1850 iterations the coupled solver is used and 2nd order upwind scheme is used for the spatial and pressure discretization. The benefit is a first order scheme is that the solution converges easier and using less computational resources. After 150 iterations the residuals of the solutions are small enough such that a more accurate solution can be obtained with the second order discretization scheme.

3.8 Limitations

Using a simplified model to represent CoE trucks, without wheels, a cooling interface and styling elements greatly reduces computational time. All these components can influence the aerodynamic properties in significantly. To find trend in aerodynamic behavior regardless of individual truck designs, a simplified design like the GETS surface model can be useful. The use of a steady state RANS solver limits the analysis of flow behavior to attached flows. It has been shown that the quantitative results of the separated flow can sometimes be used. For example the flow behavior at the rear is not simulated correctly, however the sum of the pressure coefficient can be used. Turbulence models, like k-ω are often used without further limitations for bluff body models [58].

4

MODEL VALIDATION

The solution of the CFD simulation of a GETS model (scaled at 1:15) is validated using the wind tunnel data of a 1:15 scale model. The experimental data is obtained by van Raemdonck [31]. The simulation results are compared to the findings of Cooper [4] and Newnham [21]. First the y^+ values are checked, followed by a mesh sensitivity study. Subsequently the wind tunnel setup is explained and the pressure coefficient and forces are compared. Finally the Reynolds number effect and the boundary layer development are discussed.

4.1 y^+ validation

First, the y^+ values are analyzed. According to the ANSYS Fluent manual, these should range between 30 and 300 in order to have correct wall functions [7]. The enhanced wall functionalities of ANSYS Fluent automatically detect whether wall functions should be applied. In figure 4.1 the y^+ values are shown on the 1:15 GETS model. The values range between the 30 and 300 as required. At the stagnation point the flow velocity decreases to 0 and therefore the y^+ values decrease to 0 as well. At the rear of the vehicle the y^+ values are lower than 30. The flow separates directly at the rear surface of the vehicle, therefore the boundary layer does not have to be resolved and thus the y^+ values are of no interest in this region.

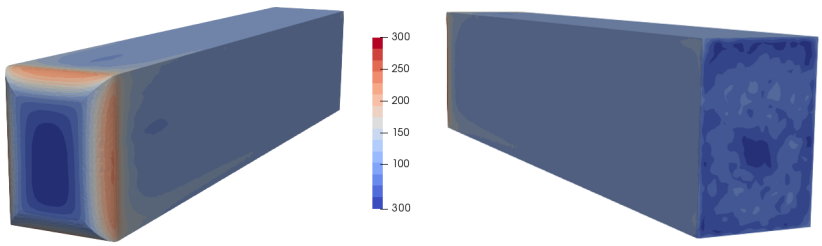

Figure 4.1: y^+ values on the 1:15 GETS model

4.2 Mesh sensitivity

A mesh sensitivity study reveals the dependency of the simulation result on the number of cells used. A trade off must be made between the computational effort and the discretization error. The discrepancy between the asymptote and the chosen cell dimensions is called the discretization error. In this mesh sensitivity study the dimensions of the inner and outer density box are varied. The first layer of cells directly mounted to the model are not altered, since this would change the y^+ value. Furthermore, the cell dimensions outside the outer density box are not changed.

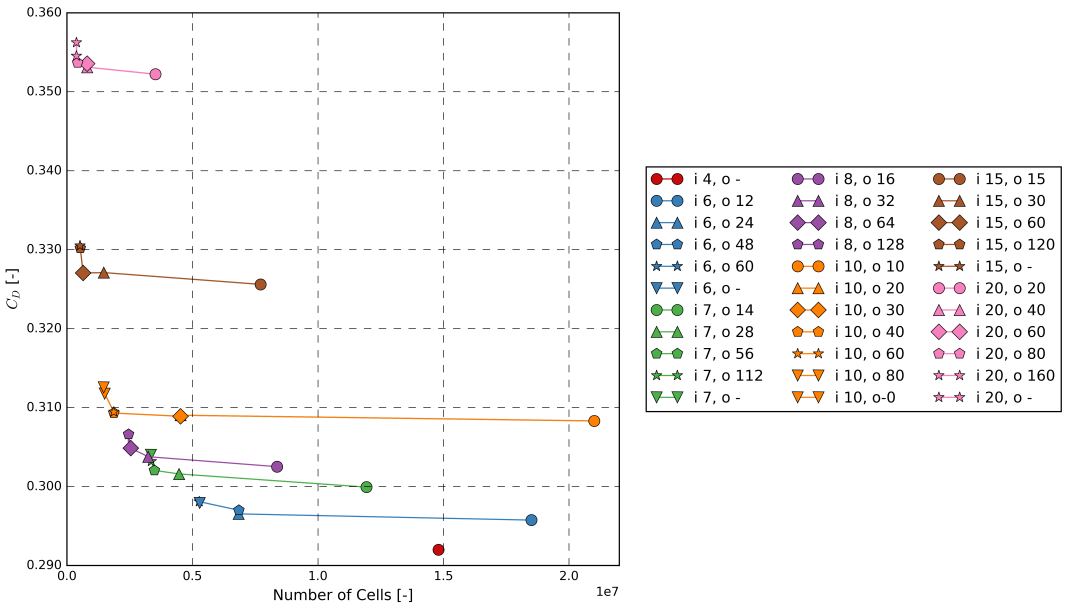

Figure 4.2: Mesh sensitivity overview. Every different color represents a different inner density box cell size. Within that group, the outer density box cell size is varied, this is visualized using different symbols. In this way the influence of the inner and outer density boxes are explored.

The results of the mesh sensitivity study are shown in figure 4.2. The C_D values are plotted versus the number of total cells for various inner and outer box cell size dimensions. Each color represents one inner box cell dimension with variations in outer box cell dimensions. The outer box cell dimension is ratio of the inner box cell dimension.

From the figure it can be concluded that the influence of the cell size in the outer density box on the C_D is minimal, however, the number of cells increases rapidly. For example, the green markers in the graph represent an inner box cell of 7 mm and a variation in outer density box cell dimensions between 14 and 112. In this case the C_D only varies between 0.3 and 0.304, while the total number of cells decreases from $12 * 10^6$ to $4 * 10^6$.

The goal of this study is to investigate the trends and flow behavior of different models. Exactly predicting the forces and coefficients is less relevant and requires a large number of cells. Therefore a trade-off has to be made: the C_D value has to be accurate enough to capture the flow phenomena correctly, while still being able to test a wide variety of models. Therefore, an inner density box size of 7 mm and an outer box size of 14 mm are chosen. The C_D is relatively close to the final C_D value of 0.292 (4 mm inner box cell size, no outer box). The discretization error of this configuration is 1-0.304/0.292 = 4.1 %. An overview of the mesh is shown in Appendix C.

4.3 Near wake structure

In figure 4.3 the near wake structure of the numerical simulation and PIV measurement conducted in the wind tunnel are shown. The figures show a projection of the path lines (black lines) and the velocity magnitude of the flow (colored surfaces) in the xy-plane at z = 0 m. From the figures one can observe two counter rotating vortices forming a ring vortex behind the model.

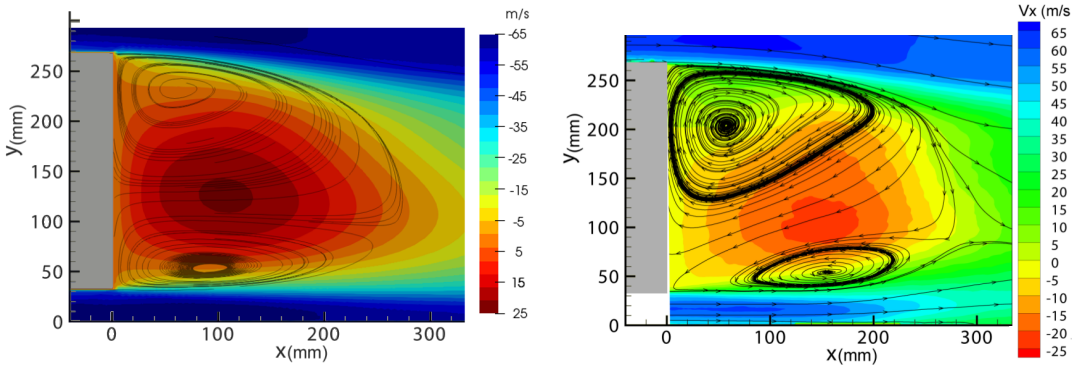

(a) Numerical simulation

(b) PIV measurement [31]

Figure 4.3: Near wake structures, numerical simulation on the left and wind tunnel on the right, performed using stereoscopic PIV measurements

Comparing the near wake structure of the numerical simulation and the wind tunnel experiment reveals that the numerical simulation underestimates the thickness of the boundary layer of the model, in particular at the lower side and the ground plate. This may result in an overprediction of the lower vortex size and an underprediction of the upper vortex size. The wind tunnel shows that flow path between the two vortices is downward instead of horizontal. In addition the length of the near wake in the wind tunnel is much smaller than in the numerical simulation.

4.4 Drag and pressure coefficient

The drag coefficient contributions for the wind tunnel and the numerical simulation are presented in table 4.1. The corrected drag coefficient in the wind tunnel is based on the Merckers method for solid and wake blockage correction.

	Scale	velocity	C_D	$C_{P,base}$
Corrected wind tunnel result	1:15	60 m/s	0.297	-0.163
Numerical result	1:15	60 m/s	0.300	-0.183

Table 4.1: Drag coefficient for the numerical simulation and wind tunnel experiment.

At a yaw angle of 0 degrees, the drag coefficient of the numerical simulation closely matches the corrected wind tunnel drag coefficient, with a discrepancy of 3 drag counts.

It is noted by the authors of the wind tunnel experiment that the struts to mount the model in the test section cause an extra drag component, which is not modeled in the numerical simulation. This causes a small offset in combination with the limitations of the turbulence model.

The pressure coefficient distribution is shown in figure 4.4, the data points are located along the centerline of the vehicle.

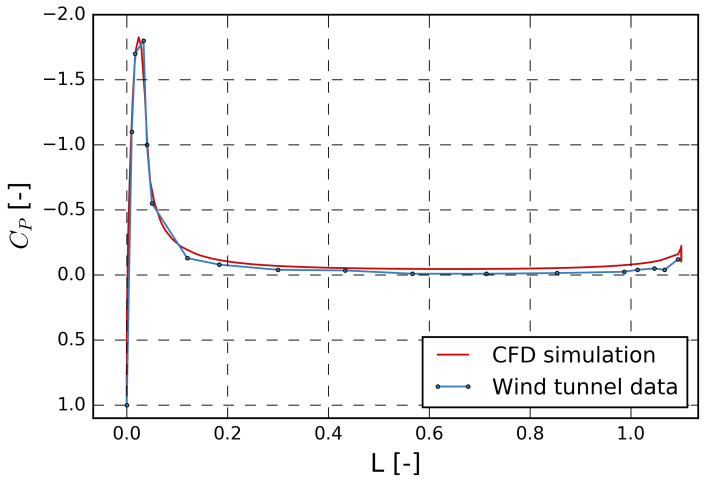

Figure 4.4: A close match is present between the pressure coefficient along the top centerline for the CFD simulation and the wind tunnel data.

The data show a good match between the wind tunnel and the CFD simulation for the pressure peak, both are equal to -1.8. At the sides the numerical simulation shows slightly higher values (more negative) and near the base the values for the wind tunnel experiment are also slightly lower.

4.5 Hoener's relationship

In section 2 Hoerner's relationship is described: according to Hoerner a relationship between the drag coefficient at the front and the rear exists (equation 2.3 and 2.2). This relation has been criticized by Saltzman and Diebler due to the mismatch in their measurements compared to Hoerner's relation. Saltzman suggests that the larger scale of the NASA vans opposed to the small scale models used by Hoerner could cause the observed difference. In figure 4.5 Hoerner's relationship is shown, including the data of the wind tunnel experiment by van Raemdonck and the numerical solutions obtained in this thesis.

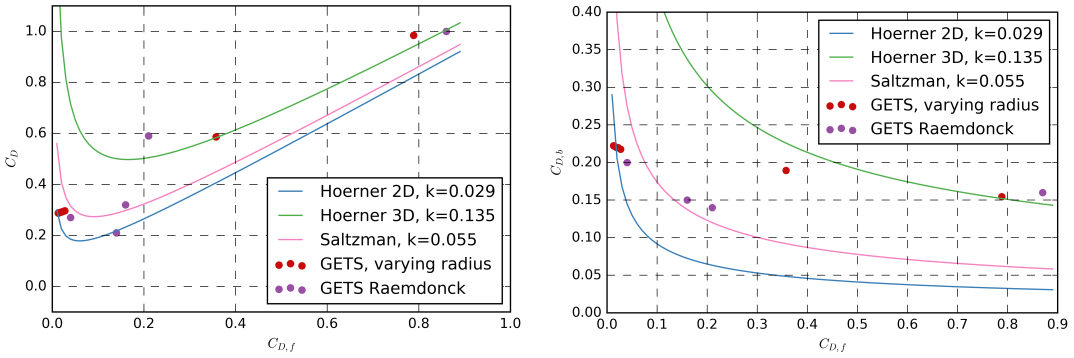

(a) Relation between the front and total drag coefficient

(b) Relation between the front and base drag coefficient

Figure 4.5: Hoerner's relationship compared with various models.

In figure 4.5(a) the relationship between C_D and $C_{Df,b}$ is shown. The fore body drag for attached flow of the GETS model varies between 0.010 and 0.027 as will be explained in section 5. For attached flow the 2D Hoerner equation and the relation of Saltzman are close to the numerical values. Hoerner's 3D equation does not represent these values correctly. For the models with (heavily) separated flow none of the three equations (2D, 3D and Saltzman) correctly predicts the relation between the fore body drag coefficient and the total drag coefficient. Figure 4.5(b) shows the relation between the fore body drag coefficient and the base drag

coefficient. The three equations do not predict the relationship very well, therefore these equations should not be used for quantitative analysis for large bluff bodies.

4.6 Skin friction coefficient

For bluff bodies the skin friction coefficient is not considered as a performance indicator. The pressure friction is the dominant source of friction. The skin friction is discussed here though to complete the drag comparison between experimental and numerical results. Is it calculated in the wind tunnel with an array of 75 Preston tubes varying in diameter on the side surface of the model. The skin friction coefficient is calculated with the Patel method and the Bechert method, resulting in a skin friction coefficient of 0.0031 and 0.0032 respectively. The skin friction coefficient distribution results are shown in figure 4.6.

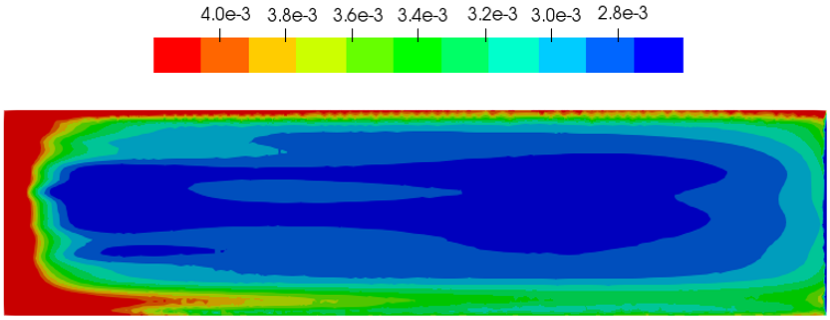

(a) Skin friction coefficient CFD

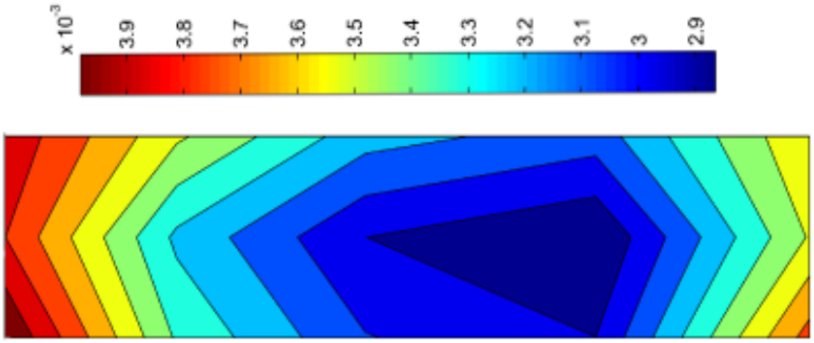

(b) Skin friction coefficient wind tunnel [31]

Figure 4.6: Skin friction coefficient distribution for the left side of the GETS model, the flow streams from left to right.

The results are comparable to a certain extend; the distribution is roughly the same, although quantitative differences are present. The average skin friction value on the side is equal to 0.00192, which is roughly 1 drag count lower than the wind tunnel result. Near the front of the side the skin friction is the highest, this is due to the high velocities passing the edge rounding. At the center of the side the lowest velocities and hence the lowest skin friction is found.

4.7 Base pressure coefficient

A large contribution of the drag coefficient is produced at the base of the vehicle. The pressure coefficient of the base is measured in the wind tunnel and is also simulated numerically. These result are summarized in table 4.2 and the pressure distribution is shown in figure 4.7.

It has been known that the RANS solving capabilities are best for attached flows, while at the base of the vehicle the flow is fully separated (as explained in section 3.2.2. Therefore, the pressure distribution should be interpreted with care. In contrast to the base pressure distribution, the averaged base pressure coefficients

should be correctly simulated using RANS simulations for bluff body flows. For example, in the studies Veluri [60] and Salari [66] the RANS model correctly predicted the average base pressure coefficient on a similar model.

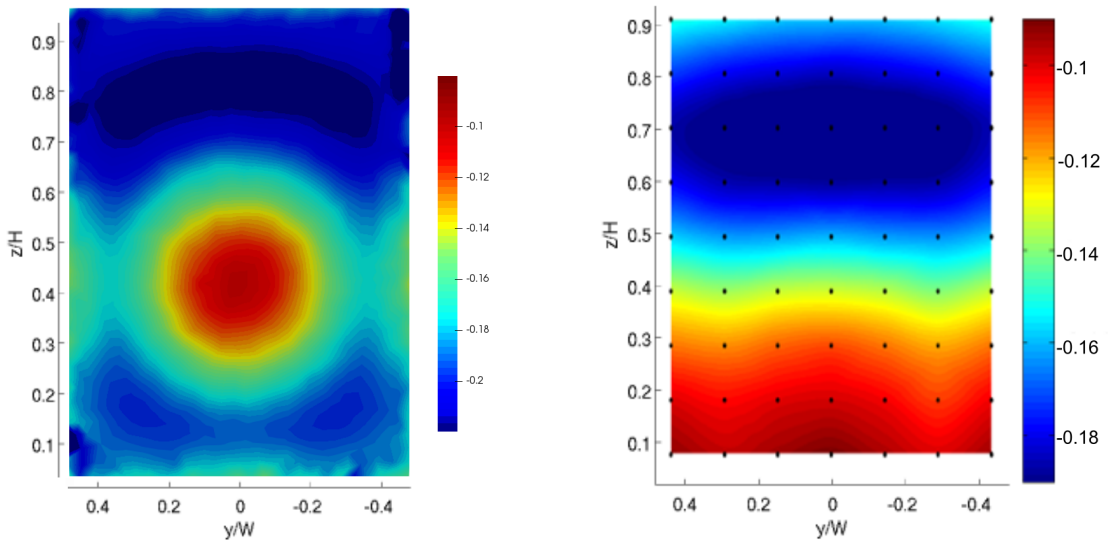

(a) Base pressure coefficient CFD

(b) Base pressure coefficient wind tunnel [31]

Figure 4.7: Base pressure coefficient distribution of the GETS model. The pressure distribution of the numerical simulation (left) is greatly different from that of the wind tunnel experiment (right).

	Scale	velocity	$C_{P,base}$
Corrected wind tunnel result	1:15	60 m/s	-0.163
Numerical result	1:15	60 m/s	-0.183

Table 4.2: Drag coefficient distribution for the numerical simulation and wind tunnel experiment

The rear surface pressure distribution shows a large difference between the CFD results and the wind tunnel experiment, as shown in figure 4.7. The distribution from the numerical simulation shows a low pressure region at the bottom in contrast to the wind tunnel experiment. The lowest pressure is reached at the top, for both the wind tunnel and CFD simulation. In the numerical simulation a circular region of high pressure is located just below the middle, this is absent in the wind tunnel experiment.

As shown in table 4.2, the pressure at the base shows a large discrepancy of 20 drag counts between the wind tunnel experiment and the simulation. The average value of the base pressure is -0.163 for the wind tunnel experiment versus 0.183 for the numerical simulation, while a similar value was expected based on previous studies. Furthermore, the total drag coefficient of the vehicle is correctly predicted as shown in table 4.1 and the pressure coefficient along the topline is also matching the wind tunnel data, illustrated in figure 4.4.

The reason for the discrepancy in average base pressure coefficient is not exactly clear. Two possible causes should be considered: incorrect measurement of the base pressure coefficient in the wind tunnel experiment and an incorrect simulation of the flow conditions at the bottom of the vehicle. The interaction between the flow above the moving road and the flow at the bottom of the model might not be captured correctly in the numerical simulation. The flow structures in the wake of the numerical simulation and in particular the lower vortex also differ from the wind tunnel experiment as illustrated in figure 4.3.

4.8 Boundary layer development

In general boundary layer properties are calculated using the displacement thickness, δ momentum loss thickness θ and the shape factor H. These properties are divided by the width, w of the model in order to

make it dimensionless.

In the wind tunnel the boundary layer properties were measured 15 mm ahead of the rear edge on the side surface of the GETS model. The comparison between the numerical and the wind tunnel results are shown in table 4.3.

	δ/w	δ^*/w	θ/w	H
Wind tunnel result	105	14	10.4	1.3
Numerical result	99	8.7	6.8	1.3
Flat Plate	110	13.6	10.7	1.3

Table 4.3: Boundary layer properties

From table 4.3 it can be concluded that the boundary layer characteristics of the numerical simulation closely match the wind tunnel measurements and that of a flat plate. The thickness of the boundary layer is slightly underestimated. The displacement thickness δ^*/w and the momentum loss thickness θ/w are significantly lower than the flat plate result. The shape factor closely matches the plate theory as well as the wind tunnel result.

4.9 Side wind effect

Side wind has a large influence on the aerodynamic flow behavior around the vehicles. In Europe the average yaw angle is 3 degrees according to study [31] for trucks. In table 4.4 the drag coefficients and the side force coefficients are compared with the wind tunnel data.

	0 yaw	3 yaw	6 yaw
Wind tunnel result, C_D	0.284	0.30	0.32
Numerical result, C_D	0.300	0.305	0.317
Wind tunnel result, C_{P_b}	-0.12	-0.13	-0.155
Numerical result, C_{P_b}	-0.182	-0.183	-0.208
Wind tunnel result, C_S	0.0	0.24	0.60
Numerical result, C_S	0.001	0.296	0.648

Table 4.4: C_D, C_{P_b} and C_S for 0, 3 and 6 degree yaw

For 0 degree yaw the drag coefficient shows good agreement, at 6 degree yaw the CFD simulation underestimate the effect of side wind.

5

ANALYSIS OF BASELINE MODELS

After the validation of the CFD simulation of the 1:15 scale model, 1:1 simulations are performed. The 1:1 scaled models include the standard GETS model and GETS models with a different front edge radius. First the difference between the 1:15 and 1:1 numerical setup and results are explained. Subsequently the baseline model and the 1:1 GETS model and its results are explained. In the final section of this chapter variations of the GETS model are discussed.

5.1 Comparison between baseline model and 1:15 setup

The 1:15 model is used as validation for the CFD simulations. In order to reveal the real world implication the model and the domain is scaled to 1:1 size. The numerical settings are compared in table 5.1. Most notably are the increase in Reynolds number (based on the frontal area) from $0.82*10^6$ to $4.88*10^6$ and the turbulence intensity from 1% to 5%. The turbulence in the 1:15 scale model was set to 1% due to wind tunnel limitations, the real world turbulence intensity varies greatly between the 1% and 12.5% [67]. For an environment without obstacles on-road turbulence levels are close to 5% [68]. In addition, McAullife [34] performed extensive road tests and advocates for a turbulence intensity of 5%.

	Validation model	Full scale model
Scale	1:15	1:1
Length	1.1 m	16.5 m
Front edge radius	36 mm	540 mm
Flow velocity	60 m/s	25 m/s
Reynolds number	$0.82 * 10^6$	$4.88 * 10^6$
Turbulence intensity	1%	5%

Table 5.1: Differences between the 1:1 and 1:15 numerical configuration.

BASELINE MODEL

The baseline model is the 1:1 scale GETS model, this model is the same as the 1:15 model, but 15 times larger. The model is shown in figure 3.4 and the dimensions are listed in table 3.3. A top view and side view of the GETS model is shown in figure 5.1 in red color. The black dotted lines represent the variations on the baseline model, which are further explained in section 5.3.

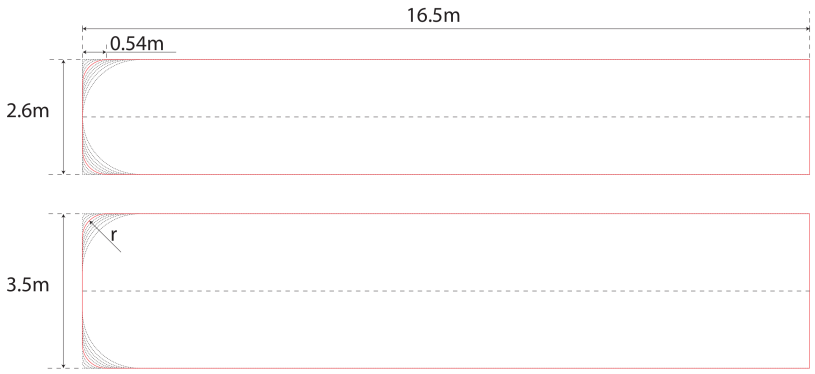

Figure 5.1: The GETS model and variations on the GETS model with different radii are shown. At the top a topview and in the middle a side view. The standard GETS model is shown in red, the variations are shown with a dashed line.

The standard GETS model will be used as a reference for the comparison with other models. The short name is GR540. 'G' stands for the GETS model and the number following 'R' represents the used front edge radius.

y^+ VALIDATION

The y^+ values are iteratively set to a value between 30 and 100 for every model. The y^+ values of the 1:1 GETS model are shown in figure 5.2. According to the Fluent manual the [7] the values should range between the 30 and 300. Kim and Barbat [69] recommend to narrow the range of y^+ even further and set the y^+ value close to 30.

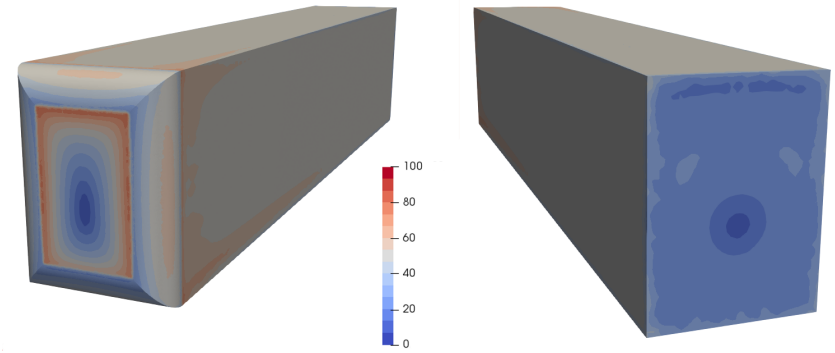

Figure 5.2: y^+ values on the 1:1 scale GETS model, the values are mostly between 30 and 80. On the left hand side the y^+ values near the stagnation point are lower, on the right hand side the base of the model is shown.

Similar to the 1:15 scale model, in the stagnation region the y^+ falls below 30, at the edges of the rectangular front surface the maximum value of 85 is reached. On the rest of the model the y^+ values vary between the 30 and 60.

MESH

Due to the larger dimensions of the 1:1 scale GETS model compared to the 1:15 GETS model and the difference in turbulence intensity the boundary layer height will be different. Using the first layer height obtained from the y^+ calculations, 18 inflation layers are used to fully capture the boundary layer. It is verified that the boundary layer is completely developed within the inflation layers, as shown in figure 5.3.

The inflation layers are also applied to the rear surface of the model in order to ensure high quality mesh cells. When no inflation layer at the base is applied, the inflation layer height is decreased in a stair step way, at the sides of the model, just before the base. This will produce low quality mesh elements when using ANSYS ICEM.

The inner density box, outer density box and the domain size cell dimensions are simply multiplied by the scaling factor of 15. Other mesh parameters are kept the same as in the 1:15 scale model, for example the aspect ratio requirements. An overview of the mesh is shown in Appendix C.

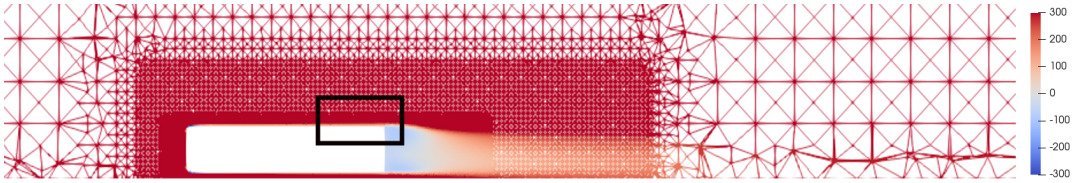

(a) Sideview of the mesh, z = 0 m.

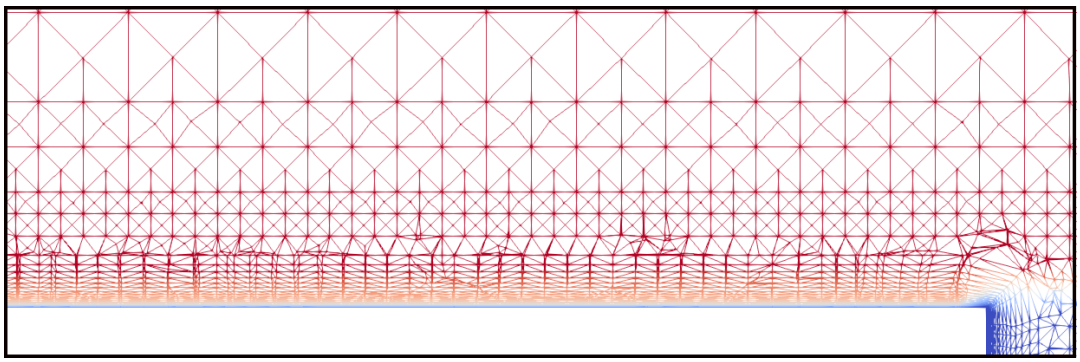

(b) Close-up of the region indicated in figure 5.3(a), at the rear surface at the top.

Figure 5.3: Sideview of the total pressure with a mesh lines overlay. The colors indicate the total pressure in m^2/s^2.

DRAG COEFFICIENT

The drag coefficient contribution of each part of the baseline model is shown in figure 5.4. The front consists out of five parts: a rectangular area where the stagnation is located and four roundings.

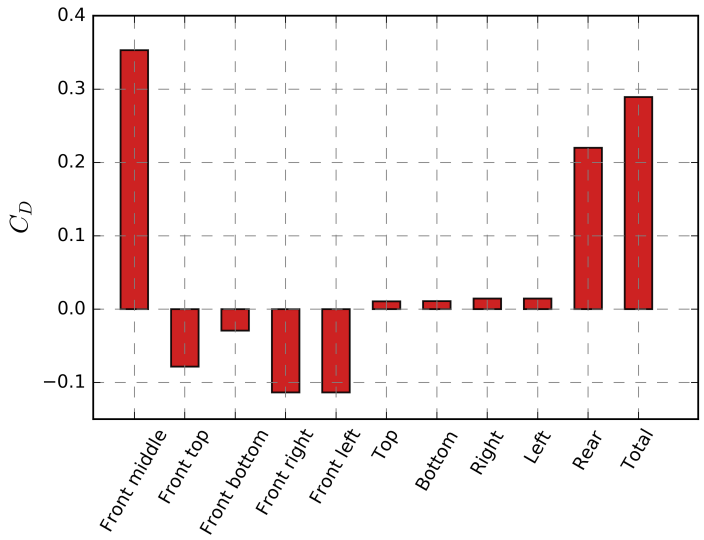

Figure 5.4: C_D contribution per surface at 0 degree yaw.

Surface 'Front middle' is the location of the stagnation point, hence the drag coefficient contribution in that area is relatively large. All other front surfaces have a negative component, id est, a suction force is present at the front edge rounding. In figure 5.4 it is shown that the suction forces at the left and right are the largest, followed by the top. At the bottom the suction forces are the lowest due to interference with the moving ground. The sides force coefficients are small and almost equal for all four surfaces. The right and left side have a slightly larger contribution due to the larger surface area. At the rear a large low pressure region exists and is responsible for a large portion (more than two thirds) of the total drag force.

PRESSURE COEFFICIENT

The pressure coefficient for the baseline model is shown in figure 5.5. Figure 5.5(a) shows the top view and figure 5.5(b) shows the side view. The white area represents the model. High pressure coefficients indicate a low flow velocity an low pressure coefficient regions indicate a high flow velocity.

(a) C_P distribution of the GR540 model. Topview y=1.75m

(b) C_P distribution of the GR540 model. Sideview, x=0m

Figure 5.5: Pressure coefficient for the baseline model. The flow in going from the left to the right.

In front of the model a large stagnation region can be identified, the pressure coefficient reaches a value of 1. Towards the corners the pressure coefficient reaches a value of -2 due to the acceleration of the flow. At the sides the pressure coefficient is close to 0. Near the base of the vehicle the flow is accelerated again and hence a lower pressure coefficient is observed.

5.2 Reynolds number effect

The Reynolds number is a critical parameter for the aerodynamic study and design of bluff bodies [3]. It is defined as the ratio of the inertial forces over the viscous forces, as described in equation 2.1. It is used to characterize among others the boundary layer thickness, the flow separation and the flow reattachment.

SAE J1252 Recommended Practice recommends a minimum value of $0.7 * 10^6$, although the validity of this number has been challenged by many authors including Hucho [70], Gilhaus [42], Storms [71]. These authors recommends width-based Reynolds numbers of between the 1 and 2 million.

In figure 5.6 the Reynolds number effect is shown for various front-edge radii: at the vertical axis the C_D is shown, on the horizontal axis the Reynolds number. The Reynolds numbers in these two graphs are based on the square root of the frontal area. Note that the dimensionless radii defined by $\eta = R/\sqrt{A}$ (a radius of 540 mm corresponds to $\eta = 0.18$). The experiments of Cooper are performed up to a maximum Reynolds number of $2.5 * 10^6$, while the CFD simulations are performed up to a Reynolds number of $6.6 * 10^6$. At this maximum Reynolds number the velocity of the vehicle corresponds with $115 km/h$.

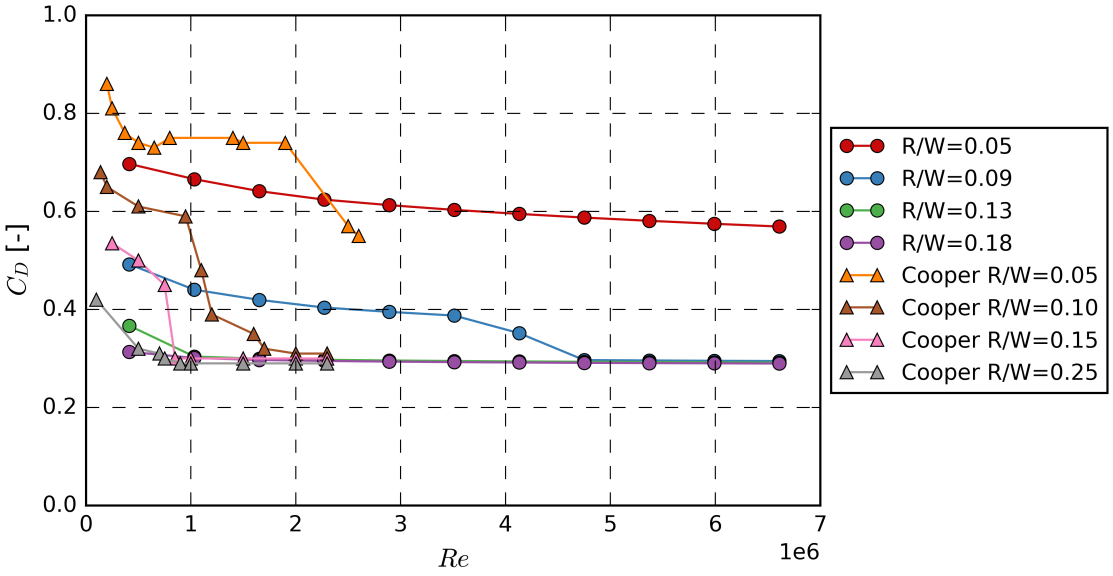

Figure 5.6: Reynolds number effect of the numerical simulation together with the results of Cooper.

The Reynolds number effects in the simulation and the Reynolds number effects of Cooper show the same trends despite the differences in model and test setup. The drag coefficient decreases when the Reynolds number increases and it converges towards a transcritical value (except for $R/W = 0.05$).

An important difference is the range over which the Reynolds number effect is investigated. The onset of the critical Reynolds number regime is found to be different for the obtained simulation results and the results of Cooper. In the numerical simulation the C_D drops at a higher Reynolds number into the stable transcritical regime.

For the full-scale model the Reynolds number is equal to $5.5 * 10^6$. At this Reynolds number, the numerical simulation and the results of Cooper are in the transcritical regime.

5.3 GETS 1:1 scale variations

Variations of the GETS model are produced to reveal the effect of the front edge radius. Work of Cooper [4] and Newnham [21] suggest that a critical radius exists based on the Reynolds number. Increasing the radius more than the critical radius is thought to have a negligible aerodynamic effect. This suggestion will be studied by using models with various radii. First all models will be explained, followed by an examination of the drag, side and pressure coefficient.

MODEL VARIATIONS

The baseline model is altered to understand the influence of the front edge radius. The circular radius is varied between 0 mm (squared model) and 1300 mm (maximum radius). All the used models are visualized in figure 5.1 with dashed lines. In red the baseline model is shown. Note that with a larger front edge radius the length of the sides decreases slightly. Every model has a code name. Like the baseline model, the 'G' is used to indicate the GETS baseline model, the number after 'R' represents the radius. All model names and properties are specified in table A.1 of the Appendix.

DRAG COEFFICIENT

In figure 5.7 the C_D at zero yaw is shown for all model variants and categorized per surface group. The drag coefficients for the front, sides, rear and total are listed in table B.1 for yaw angles of 0, 3 and 6 degrees.

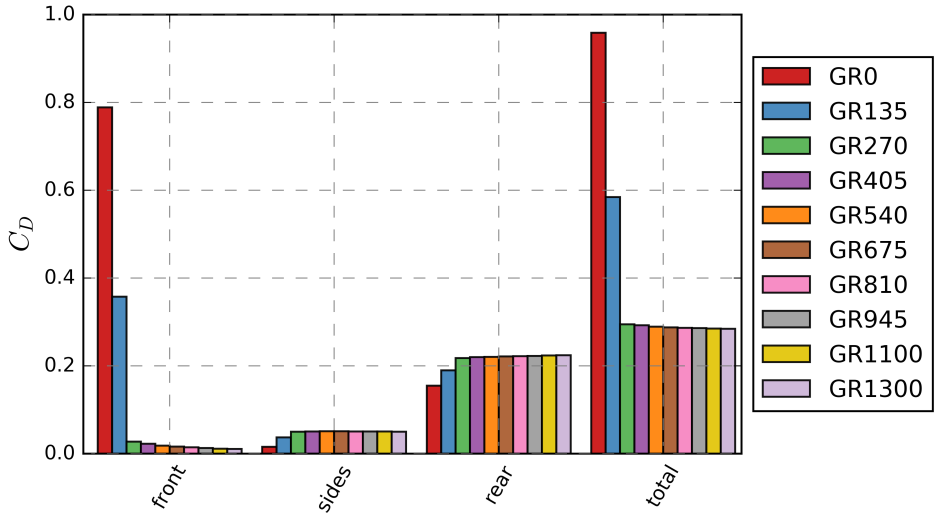

Figure 5.7: Drag coefficient for the GR models categorized per surface group.

It can be observed that the radius has a large effect on the total C_D. GR0 and GR135 shown the highest C_D, this is due to flow separation on the front edge of the model. All other models show very similar behavior, although small changes in C_D still exist. Starting with the front surfaces: increasing the radius decreases the drag coefficient by a minimal amount. The sides show a very constant drag coefficient for all models and the rear drag coefficient is slightly increasing with increasing the front edge radius. Summing all the components results in a trend in which the total drag force coefficient decreases slightly when the radius increases. The difference between the reference model GR540 and GR1300, the model with the maximum circular front edge radius, is only 5 drag counts.

Drag can be divided in pressure and viscous drag, for the GETS model variants this is shown in figure 5.8.

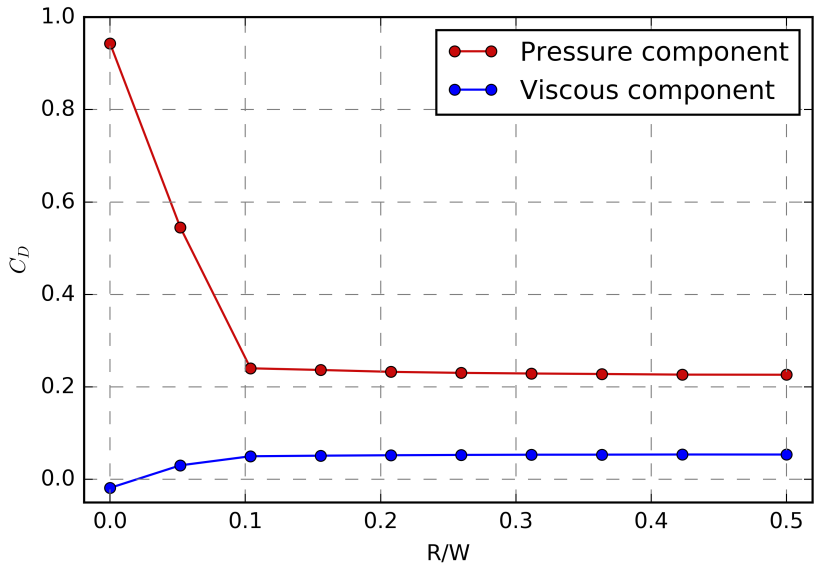

Figure 5.8: The figure shows the pressure force and viscous force for various front edge radii. The pressure force and viscous force are expressed in terms of their contribution to the drag coefficient.

One can observe that for the separated cases, GR0 and GR135, the pressure forces are dominant by a large margin over the viscous forces. From GR270 till GR1300 the pressure and viscous forces change by a small amount; the pressure forces slowly decreases while the viscous forces slowly increase.

PRESSURE COEFFICIENT

The flow around the different models is compared by analyzing the pressure distributions and the pressure coefficient at the centerline of the model. Figure 5.9 shows the pressure coefficient along the centerline of three different models.

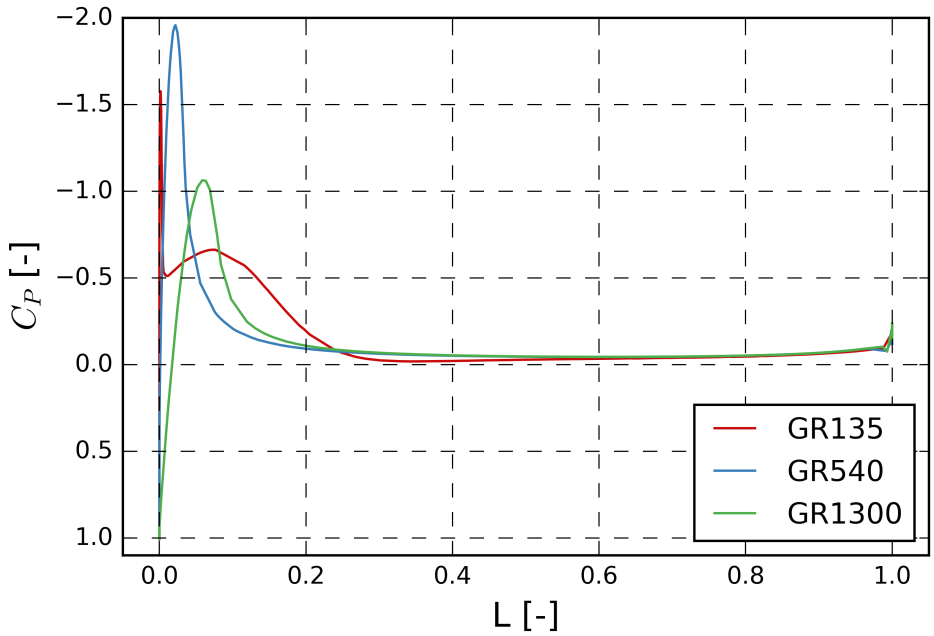

Figure 5.9: Simulated pressure coefficient along the top centerline for three different models.

As can be seen from the figure, larger radii show a lower pressure peak, while the pressure peak lasts longer. The pressure peaks for larger radii last longer because it acts on a larger surface. The pressure coefficient along the centerline of GR135 is different as this model has separated flow.

For each of these models one can also analyze the distribution of the pressure coefficient. The pressure coefficient distribution for the three models is shown in figure 6.4. The top figure shows the model without a radius, the center figure is the baseline model and at the bottom the GR1300 model is presented.

The pressure coefficient distribution reveals that the stagnation area of GR0 is much larger than the stagnation area of the GR540 and GR1300 models. The low pressure area at the sides of the GR540 and GR1300 models is not present at the GR0 model due to separation of the flow at the sharp corners. At the rear of GR0 model the vortical structures, which are present in the other models, are also not observed.

(a) C_P distribution of model GR0

(b) C_P distribution of model GR540

(c) C_P distribution of model GR1300

Figure 5.10: Top view; C_P distribution of models GR0, GR540 and GR1300.

PRESSURE DISTRIBUTION REAR

The pressure distribution at the rear is one of the largest contributors to the overall drag of the vehicle. In figure 5.11 the pressure coefficient distribution of GR0 and GR540 are compared. As can be seen from this figure the location of the pressure coefficient peak and its value are different. However, as explained in section 4.7, RANS is not able to predict the distribution correctly at the rear, therefore, the relevance of these pressure distributions figures can be discussed.

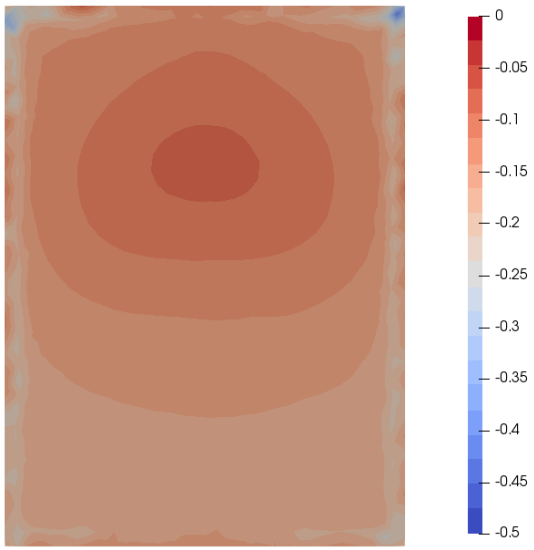

(a) C_P rear GR0

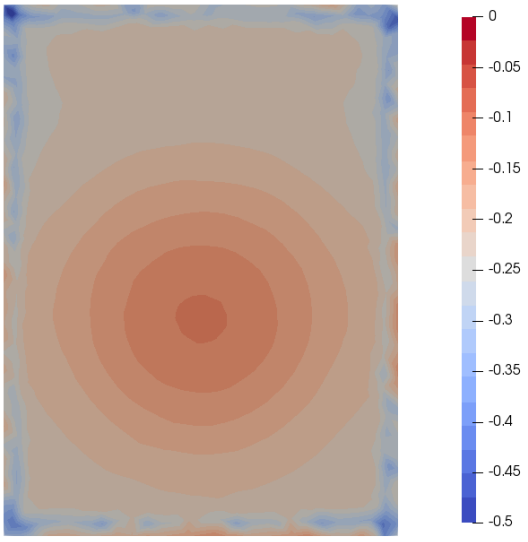

(b) C_P rear GR540

Figure 5.11: Distribution of the pressure coefficient at the rear surface of the models GR0 and GR540.

The contribution of the base pressure to the drag coefficient of the models is shown in table B.1 (in the appendix). It can be observed that the yaw averaged drag coefficient at the rear surface increases with 4 drag counts between GR540 and GR1300, for these models the flow is attached at all yaw angles. When separation occurs, the drag coefficient contribution at the rear changes significantly (more than 50 drag counts).

EFFECT OF YAW ANGLE

The effects of yaw angle are important to take into consideration, since this represents the wind of various directions. The drag force coefficient, side force coefficient and the pressure distribution are analyzed in this section for 3 and 6 degree yaw.

Drag force coefficient In figure 5.12 the drag force coefficient distribution is shown for 0, 3 and 6 yaw for the GETS models with different radii.

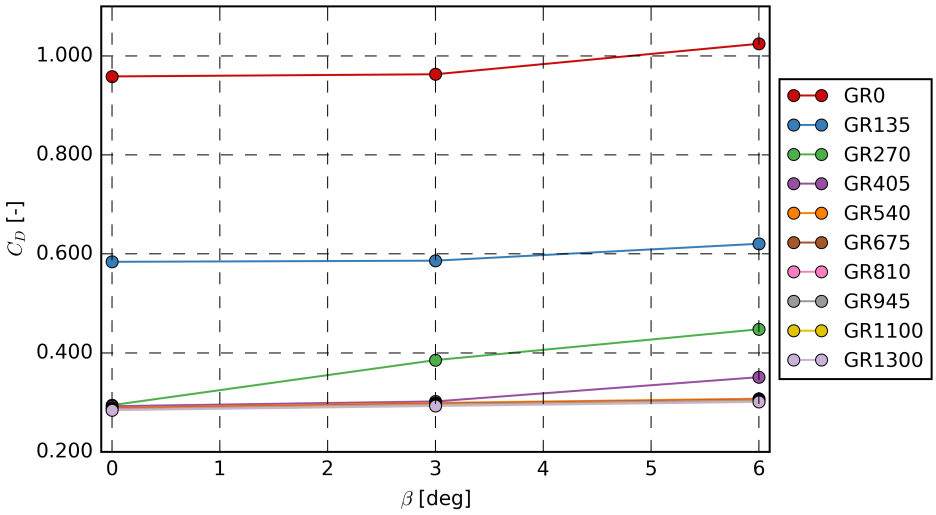

Figure 5.12: Drag coefficient of GETS models with different radii for 0, 3 and 6 degree yaw.

As explained in section 5.3, the drag coefficient varies largely due to separation at the front egde radii of the model. For radii slightly smaller than the critical radius of 540 mm ($\eta = 0.18$), flow separation depends on the yaw angle. For a yaw angle of zero degrees the flow stays attached, while the flow separates at larger yaw angles.

For example, the GR270 model has a drag coefficient of 0.294 at 0 yaw, 0.385 at 3 yaw and 0.448 at 6 degree yaw. In contrast, the baseline model shows only a minor increase in drag coefficient: 0.289 at 0 yaw to 0.308 at 6 yaw. The drag increase is caused by separation on the front edge of the model. This can also be observed in table B.1 in the appendix, the front surface increases from 0.027 for 0 yaw to 0.114 for 3 yaw and 0.147 for 6 yaw, while the C_D of the sides and rear remain almost constant. The GR405 model is also displaying signs of separation at 6 yaw, while at 0 and 3 yaw the C_D remains near that of the baseline model. Increasing the radius beyond the critical radius does not lead to significant changes in C_D. At 0 yaw the difference between GR540 and GR1300 is 5 drag counts, and at 6 yaw the difference is 7 drag counts. This difference is caused by the 1 drag count at the sides and 1 drag count at the rear.

In order to better show the effects of flow separation, figure 5.13 is added. This figure shows the flow velocity in x direction for the GR270 model. The velocity distribution is shown at half the model height. In addition, an iso-surface is visualized where the flow velocity in x-direction equals $0 m/s$. This indicates the locations of flow separation. In figure 5.12, it is shown that the drag coefficient drastically increases for yaw angles of 3 and 6 degrees. In the figure below, using the velocity distribution, it can be observed that the high drag coefficient is produced by the flow separation at the front edge.

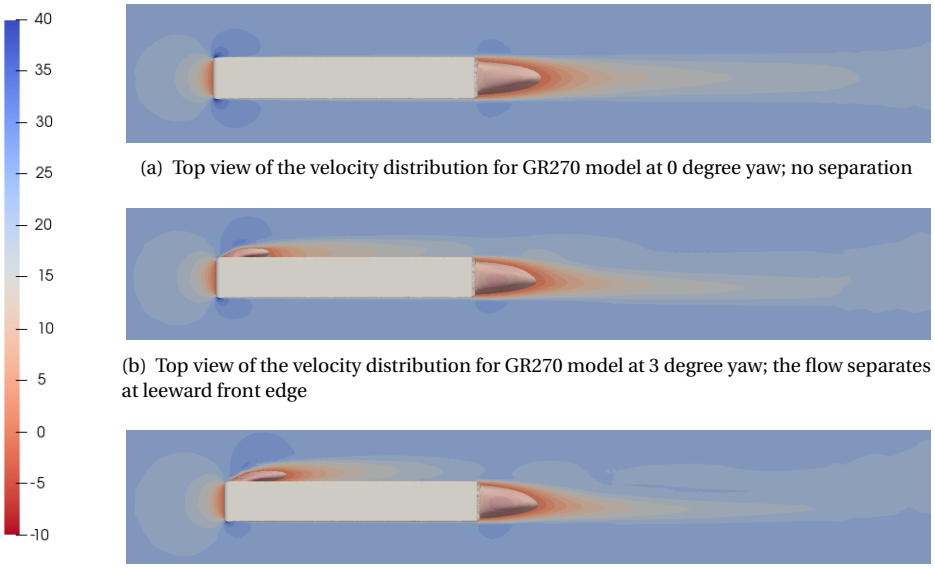

(a) Top view of the velocity distribution for GR270 model at 0 degree yaw; no separation

(b) Top view of the velocity distribution for GR270 model at 3 degree yaw; the flow separates at leeward front edge

(c) Top view of the velocity distribution for GR270 model at 6 degree yaw; the flow separates at leeward front edge

Figure 5.13: Velocity distribution in x direction at y = 1.75 m for the GR270 models for 0, 3 and 6 degree yaw. At the leeward front edge and at the rear an iso-surface is visualized where the flow velocity in x direction equals 0 m/s, this iso-surface indicates that flow does not separates for 0 yaw, in contrast to the 3 and 6 degree yawing angle.

Side force coefficient The side force coefficient is a measure for the susceptibility of the vehicle to side wind, and is therefore important for the stability of the model. In figure 5.14 the side force coefficient distribution is shown for 0, 3 and 6 yaw.

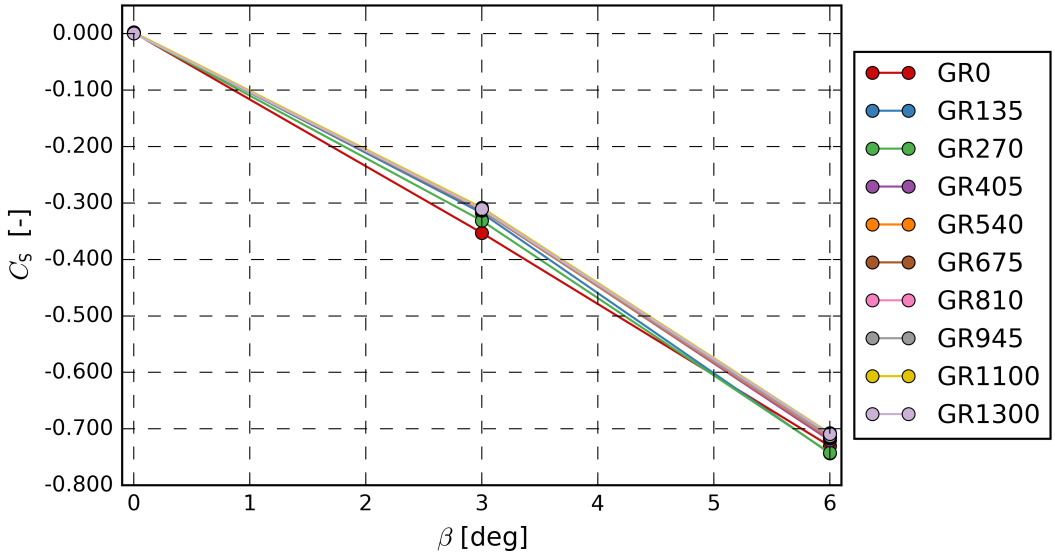

Figure 5.14: Side force coefficient of the GETS model

In figure 5.14 the trend for all models is almost the same. At 0 degree yaw the side force coefficient is negligible, at 3 degree yaw the C_S varies between -0.3 and -0.35 and at 6 yaw the C_S varies between -0.7 and -0.75.

Pressure distribution In figure 5.12 the pressure coefficient distribution is shown for 3 and 6 yaw.

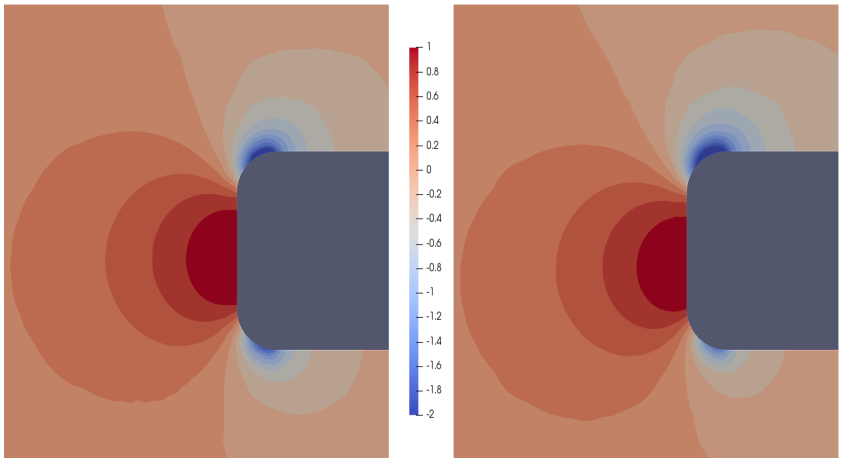

Figure 5.15: GETS pressure coefficient distribution, top view. 3 yaw angle at the left and 6 degree yaw angle at the right. The flow is entering from the lower left corner.

At 0 degree yaw angle the pressure distribution at the front edges are similar, for 3 and 6 degree yaw angle differences between the front left and front right edge can be observed. At the leeward side (front right edge) the pressure coefficient is higher in the 3 yaw and 6 yaw case.

5.4 Conclusion

In this chapter the 1:15 scale model is scaled to the 1:1. The differences between these two models are mainly present in the drag coefficient due to the change in Reynolds number and turbulence intensity. Decreasing the front edge radius below the 540 mm of the baseline model shows separated flow for at least 1 yaw angle. Increasing the front edge radius decreases the drag coefficient with a very small amount. The larger the radii the lower the stagnation pressure, but also the lower the suction forces around the corners.

6

ANALYSIS OF ELONGATED MODELS

The designs in this chapter are based on a 500 mm elongated GETS model. The aerodynamic effects of several designs are investigated. For each design a comparison will be made with the standard (not elongated) GETS model, this model has a front edge radius of 540 mm. First the effect of different circular front edge radii will be investigated, followed by the effect of elliptical front edge radii and asymmetrical front edge rounding. The final part of this chapter will cover different front shapes and a summary of the obtained trends.

6.1 Effect of circular front edge radius

The first effect that is investigated is the variation in the front edge radius of the EGETS model. It is varied in the same way as the GETS model is varied: the minimum radius is 0 mm and the maximum radius is 1300 mm.

MODEL EXPLANATION

The models in this section are almost identical to that of the section above, the difference is the 500 mm elongation as is shown in figure 6.1. In red the baseline model is sketched, the EGR1100 and the EGR1300 models are just trimming the baseline model. All model names and model properties are given in table A.2 of the appendix.

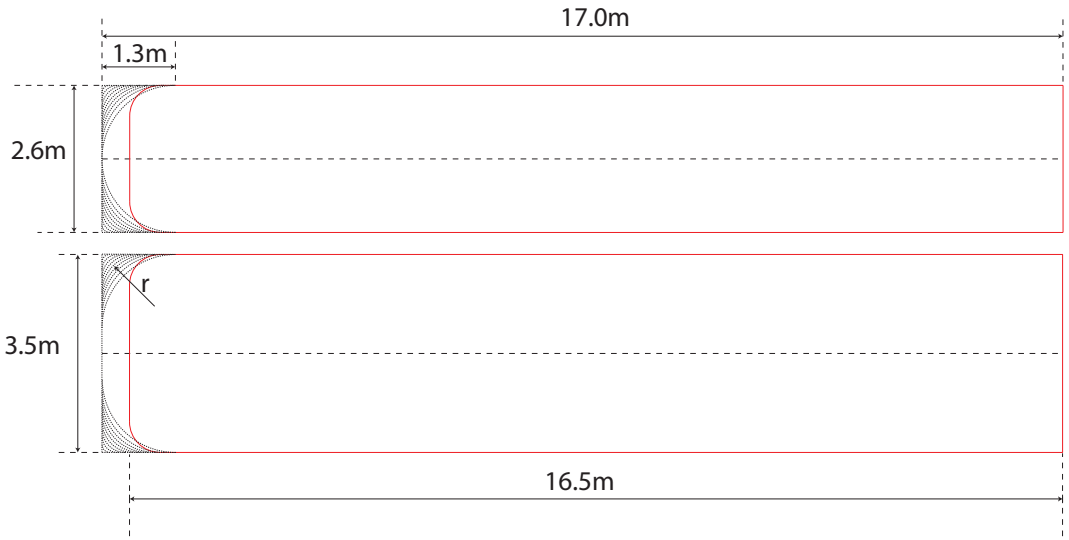

Figure 6.1: EGETS model overview, above the top view, below the side view of the elongated models.

DRAG CONTRIBUTIONS

The drag coefficient is a measure for the aerodynamic efficiency of the model, this will be the major focus point of changing the radius. In figure 6.2 the drag coefficients of the EGETS models with various radii are shown for 0, 3 and 6 yaw. The results are also listed in table B.2 of the appendix and.

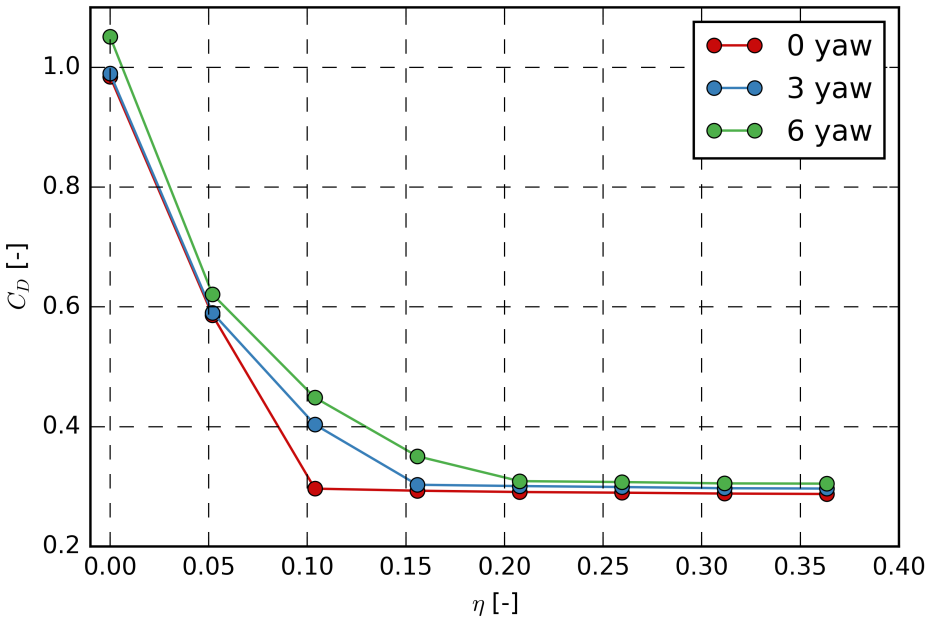

Figure 6.2: Drag coefficient for all EGETS models for 0, 3 and 6 degree yaw

Drag coefficients range from 0.985 for the EGR0 model to 0.284 for the EGR1300 model. For EGR0 and EGR135 the drag coefficient is significantly higher for all yaw angles compared to the other models due to separation at all yaw angles. For EGR270 and EGR405, the separation only occurs at higher yaw angles: EGR270 increases from 3 degree yaw onward and EGR405 increases at 6 degree yaw angle.

Drag contribution per surface The drag contributions per surface are depicted in figure 6.3 for three GETS models, GR270 (red), GR540 (blue) and GR945 (green). The positive and negative drag contribution of the individual mesh elements on each surface are summed in order to acquire the separate positive and negative drag coefficient of each individual surface. The surface of the front edge radii have a positve and negative component.

From figure 6.3 it can be observed that the sides have a very small role in the overall drag coefficient for zero degree yaw. The contribution at the rear increases slightly with increasing front edge radius. The positive pressure at the front middle surface of the vehicle is drastically reduced by applying a larger radius, while the drag contribution of the front edges increases with increasing front edge radius. It is noted that the wetted area of the 'front-middle' part is reduced when a larger radius is applied and with the same logic the wetted area of the curved surfaces like 'front-top' is increased. When the front middle and front sides surfaces are accumulated, the drag of this group is reduced with increasing radius, this is shown in table 6.1. At zero degree yaw a decrease of 17 drag counts is observed between EGR270 and EGR1300 for the front group, while the sides remain almost constant and the rear contribution is increased with 5 drag counts.

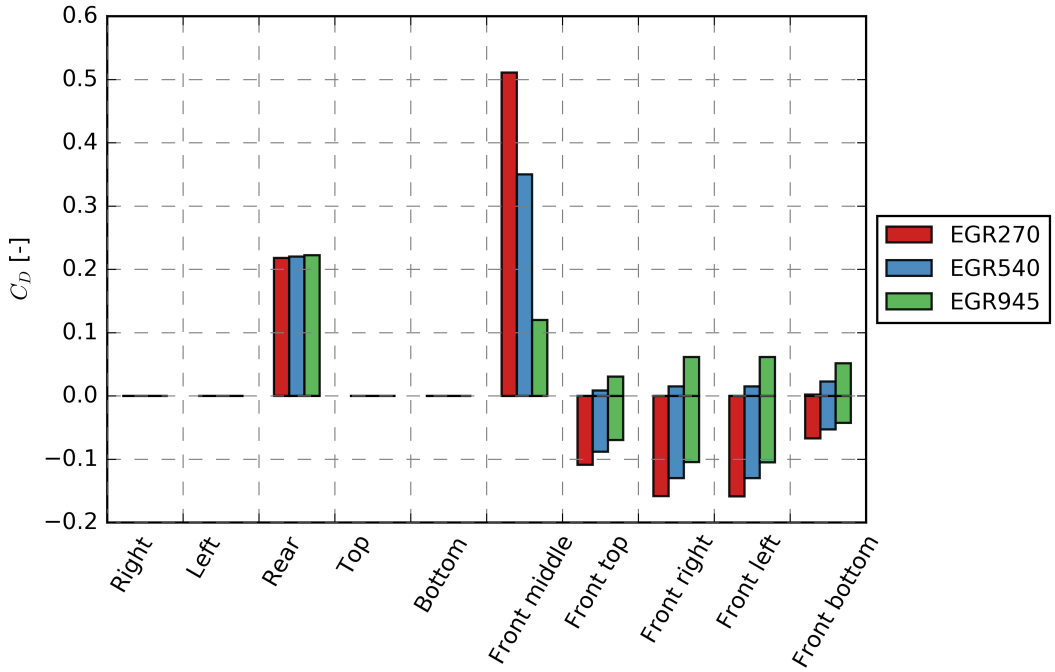

Figure 6.3: Individual positive and negative contributions to the drag coefficient for each of the surfaces for EGR270(red), EGR540(blue) and EGR945(green).

When comparing the drag coefficient contributions of the surfaces in table 6.1 for 0, 3 and 6 yaw, one can observe the following: the drag coefficient for the small radius increases rapidly with increasing yaw angle just as the normal GETS model. For larger radii the differences observed at 0 degree yaw are also present at 3 degree yaw and 6 degree yaw. The drag coefficient at the rear increases slightly with increasing radius, this can be attributed to the thinner boundary layer as explained by Hoerner [27].

	0 yaw				3 yaw				6 yaw			
Modelname	tot	front	sides	rear	tot	front	sides	rear	tot	front	sides	rear
EGR270	0.297	0.028	0.051	0.218	0.404	0.133	0.050	0.221	0.449	0.146	0.054	0.248
EGR540	0.291	0.019	0.052	0.220	0.301	0.021	0.054	0.226	0.309	0.004	0.057	0.249
EGR945	0.288	0.013	0.052	0.222	0.297	0.015	0.053	0.228	0.305	-0.002	0.056	0.250
EGR1300	0.284	0.011	0.051	0.223	0.293	0.013	0.053	0.228	0.301	-0.004	0.055	0.250

Table 6.1: Drag coefficients for elongated models with a circular front edge radius

6.1.1. PRESSURE DISTRIBUTION

The pressure distribution of EGR135, EGR540 and EGR1300 are shown in figure 6.4(a), 6.4(b) and 6.4(c). As expected from the findings for the non-elongated models, the trends are identical. The stagnation area is reduced in size and the pressure peaks are reduced in magnitude as the radius increases. In the topfigure 6.4(a) the flow at the top of the model is fully separated, while at the bottom a suction peak is present due to the interaction with the flow of the moving ground. This effect is not visible for the other two models.

(a) C_P distribution of model EGR135

(b) C_P distribution of model EGR540

(c) C_P distribution of model EGR1300

Figure 6.4: Side view; C_P distribution of models EG135, EGR540 and EGR1300.

COMPARISON WITH STANDARD GETS MODEL

Comparing the elongated GETS models with the baseline models reveals that the maximum difference in C_D is only 5 drag counts. The lowest C_D in the elongated models is achieved using a front edge radius of 1300 mm. A direct comparison of the drag coefficient of the surfaces per yaw angle is shown in table 6.2.

	0 yaw				3 yaw				6 yaw			
Modelname	tot	front	sides	rear	tot	front	sides	rear	tot	front	sides	rear
GR540	0.289	0.018	0.051	0.220	0.299	0.020	0.052	0.226	0.308	0.003	0.056	0.249
EGR540	0.291	0.019	0.052	0.220	0.301	0.021	0.054	0.226	0.309	0.004	0.057	0.249
EGR1300	0.284	0.011	0.051	0.223	0.293	0.013	0.053	0.228	0.301	-0.004	0.055	0.250

Table 6.2: A comparison between the drag coefficients of various surfaces of three model types for yaw angles of 0, 3, and 6 degrees.

When the baseline model is compared to the elongated variant with the same radius (EGR540) it can be observed that a slightly higher drag coefficient is produced by the front and side surfaces when an elongation is applied.

CONCLUSION

Elongating the model and applying a large front edge radius can have a beneficial influence on the C_D. The largest difference between the EGR models and the baseline models is 5 drag counts. It is noted that this is a small difference.

6.2 Effect of elliptical front edge radius

Elliptical shapes are often used in low drag bodies, therefore it is investigated whether an elliptical front edge rounding can be beneficial in terms of drag coefficient.

MODEL EXPLANATION

An ellipse can be defined using a major and minor axis, as shown in figure 6.5. L1 is the major axis and L2 is the minor axis; these are varied while the minimum radius of the ellipse at all points is 540 mm or higher. The minimum radius is calculated using equation 6.1 [72]:

$$R_{min} = \frac{c^2}{b}, \tag{6.1}$$

where b is the length of the major axis and c the length of the minor axis. The location of the minimum radius is at the end of the major axis. Keeping the minimum radius larger than 540 mm, should prevent separation in all side wind conditions. Six models are studied: three with $L1 > L2$ (the short ellipse models) and three with $L1 < L2$ (the long ellipse models). In red the standard GETS model outline is indicated.

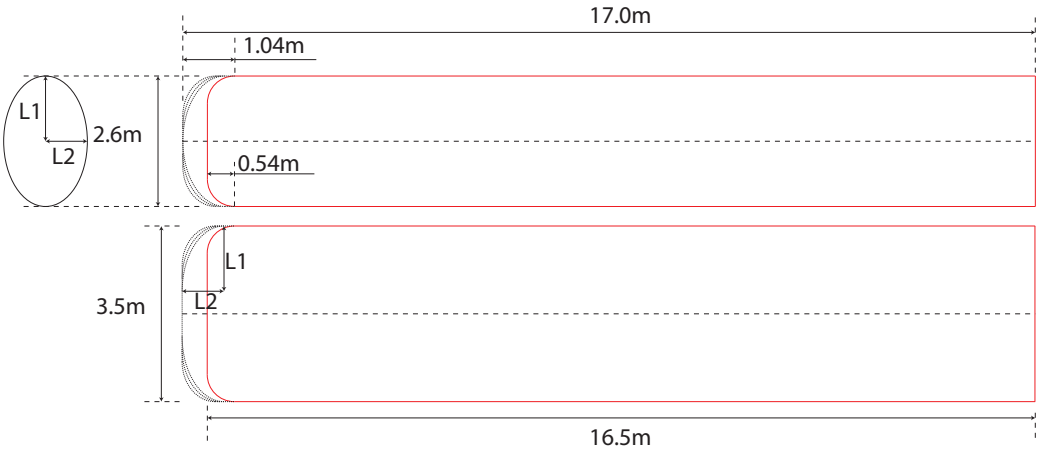

(a) Topview and sideview of models with a larger L1 than L2

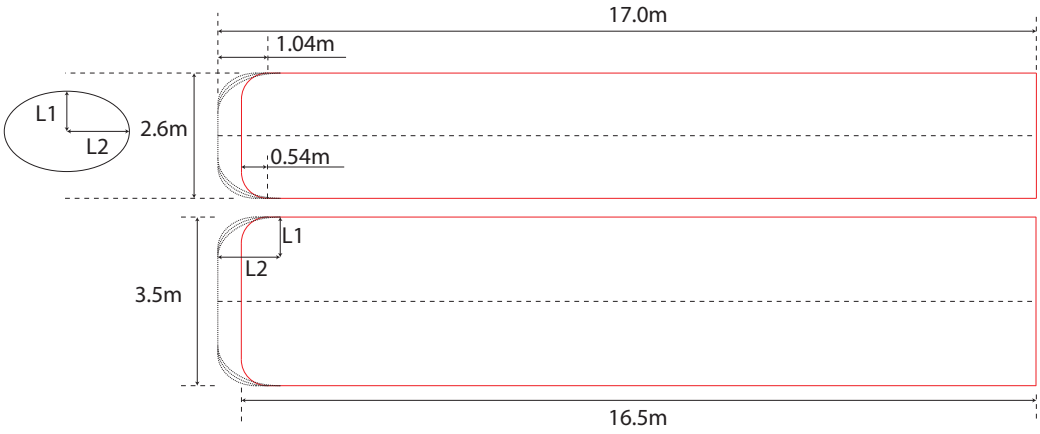

(b) Topview and sideview of models with a smaller L1 than L2

Figure 6.5: Elliptical rounding models, the standard GETS model is shown as a reference.

The names of the models and its properties are listed in table A.3 of the appendix. The model names consist of an 'E' to indicate the elongated model, an 'L' with a number for the length of the lateral axis 'L1' and another 'L' with a number indicating the length of longitudinal axis 'L2'.

DRAG COEFFICIENT

The drag coefficient for all models is shown in table B.3 for 0 yaw, 3 yaw and 6 yaw. The differences are the most significant when the minor and major axes are largest, therefore these are shown in table 6.3.

	0 yaw				3 yaw				6 yaw			
	tot	front	sides	rear	tot	front	sides	rear	tot	front	sides	rear
GR540	0.289	0.018	0.051	0.220	0.299	0.020	0.052	0.226	0.308	0.003	0.056	0.249
EL1299-L834	0.288	0.013	0.052	0.222	0.297	0.015	0.054	0.228	0.305	-0.002	0.057	0.250
EL834-L1299	0.286	0.011	0.051	0.223	0.295	0.013	0.053	0.229	0.302	-0.004	0.055	0.251

Table 6.3: Drag coefficient summary for elliptical models

Model EL1299-L834 is the model with the short axis in the longitudinal direction. The C_D only performs slightly better than the baseline results. One drag count for 0 yaw and three drag counts for 6 yaw. The other model, EL834-L1299, performs marginally better. Noticeably, the front of both models produces a lower drag coefficient (for all yaw angles), but this result is counteracted by the increase in drag coefficient at the rear.

PRESSURE COEFFICIENT DISTRIBUTION

The pressure coefficient distributions for the two models in table 6.3 (EL1299L834 and EL134L1299) are shown in figure 6.6.

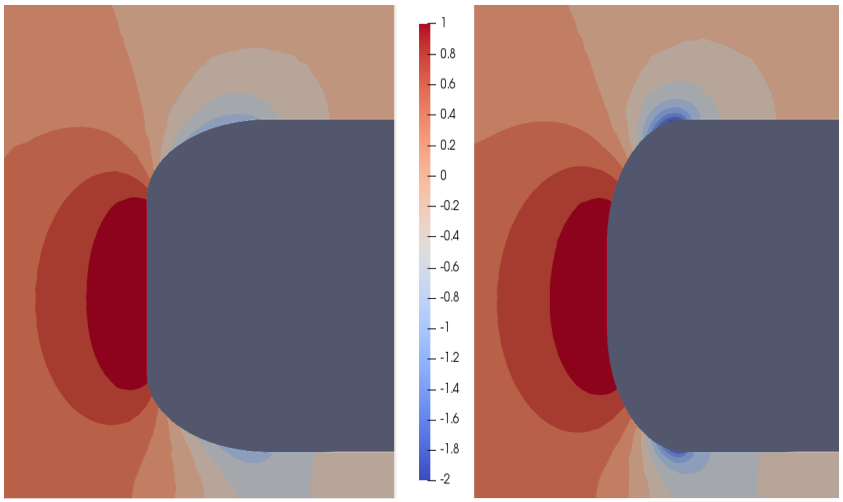

Figure 6.6: Pressure distribution of EL834L1299 on the left and EL1299L834 on the right.

In figure 6.6 the pressure distribution for these models is shown in the xy-plane at z=0 m. Both models have a minimal radius of 540 mm, the location of this minimum radius is located upstream for the left model (near the rectangular front) and downstream for the right model (near the side surface of the vehicle). Differences in pressure coefficient between these models, reveal that the location for an elliptical rounding is important for the flow development around the vehicle. A more upstream location of the minimum radius produces a lower stagnation pressure at the front and hence lower suction forces at the front edges. For a more downstream location, this effect is reversed.

CONCLUSION

Elliptical radii can decrease the C_D, just like the circular models. The benefits of the reduced drag at the front of the models are offset by the increase in drag at the rear surface. The location of the minimum radius, upstream or downstream, has a minor influence on the aerodynamic drag reduction potential. A drag coefficient reduction of 3 drag counts can be realized using an elliptical fillet with respect to the standard GETS model.

6.3 Frontal end design variations

The final part of this research, variations in front end shapes, is split in three parts: the first starts with a new baseline model on which various front end designs are systematically varied. The second is also based on the baseline model, but uses different front edge radii. Lastly more radical designs, such as a slanted front and a SN are explored.

6.3.1. FRONTAL SHAPE VARIATIONS

The influence of the frontal shape is explored in this section. First a new baseline model for all these frontal shapes is constructed, this model is shown in figure 6.7. By changing systematically one of properties the influence of all the shapes is explored. The baseline model E_S consists of a rectangle front shape with a width and height of one third of the total vehicle width and height. This frontal rectangle is altered in shape, for example a triangle (figure 6.9(d)) and the location of the rectangle is varied as shown in figure 6.8

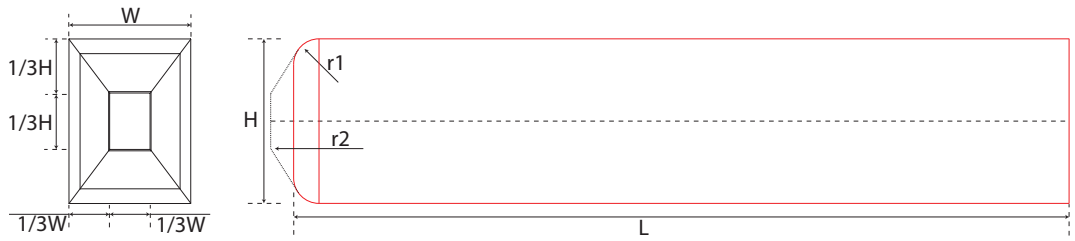

Figure 6.7: Baseline model E_S frontview and sideview.

The total length of the baseline model is 17.0 m and the outer radii (r1) are set at 540 mm to prevent flow separation. A small rectangular shape is used as a frontal area, with radii of 148 mm (r2), inspired by the radii of the GTS model [65]. Variations are made by altering the vertical position of the rectangular area, as shown in figures 6.8(a), 6.8(b), 6.8(c). In addition, the size of the rectangular shape is changed: smaller/wider and taller/shorter (figure 6.8(e) and 6.8(d)). Next the shape is modified, from a rectangular to a point, line, triangle, and a circle (figure 6.9).

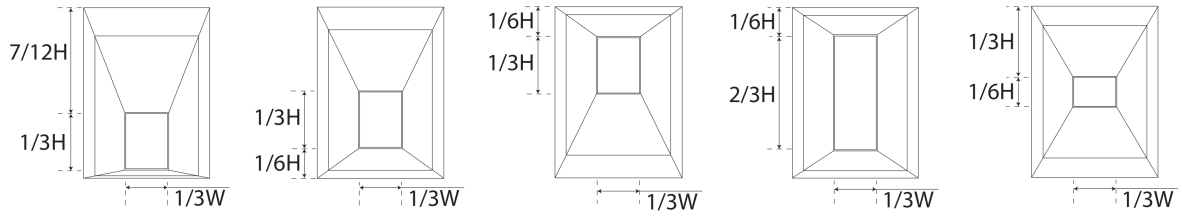

(a) E_S_lowest (b) E_S_down (c) E_S_up (d) E_S_taller (e) E_S_shorter

Figure 6.8: Model variations on the baseline model, the rectangle is varied in size and position.

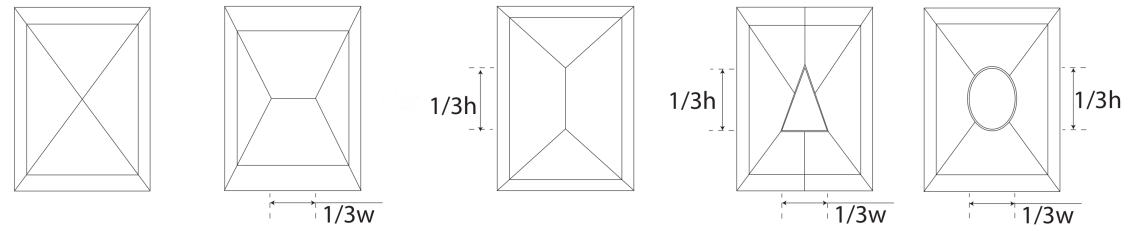

(a) E_S_point (b) E_S_hline (c) E_S_vline (d) E_S_triangle (e) E_S_ellipse

Figure 6.9: Model variations on the baseline model, the 500 mm front elongation is used to shape different front end designs.

In figure and 6.9, variations in front end designs are shown. The front edge radius is kept constant at 540 mm in order to prevent separation for all yaw angles. Only the 500 mm front elongation is used to design the different front end shapes.

DRAG COEFFICIENT

All the results with respect to the drag coefficient can be found in table B.5 of the appendix. For two models (E_S_lowest and E_S_wider) a significant difference can be observed. It is very likely that the frontal square

of these models is too close to the rounding such that the surface on which the rounding acts is too small to keep the flow attached. In table 6.4 a selection of the results is shown.

	0 yaw				3 yaw				6 yaw			
	tot	front	sides	rear	tot	front	sides	rear	tot	front	sides	rear
GR540	0.289	0.018	0.051	0.220	0.299	0.020	0.052	0.226	0.308	0.003	0.056	0.249
E_S	0.289	0.015	0.052	0.222	0.298	0.017	0.053	0.228	0.307	0.000	0.056	0.250
E_S_lowest	0.301	0.030	0.051	0.220	0.310	0.032	0.052	0.225	0.319	0.016	0.055	0.249
E_S_vline	0.288	0.014	0.052	0.222	0.297	0.016	0.053	0.227	0.305	-0.001	0.057	0.250
E_S_triangle	0.286	0.014	0.051	0.222	0.295	0.016	0.052	0.227	0.304	-0.001	0.055	0.250

Table 6.4: Drag coefficient summary for models with various front designs.

In comparison to the GETS baseline model the E_S_lowest has a high C_D and is therefore not an aerodynamic improvement. The other shape variations do not show significant changes in the total drag coefficient with the baseline model. For example, E_S_triangle shaped front has a lower drag coefficient of 4 drag counts at the front, but an increase of 2 drag counts at the rear. The triangle shape is most beneficial in terms of the drag coefficient.

PRESSURE COEFFICIENT

The simulated pressure coefficients on the frontal surface for different models are analyzed. The models analyzed are the baseline model (E_S), E_S_lowest and E_S_point.

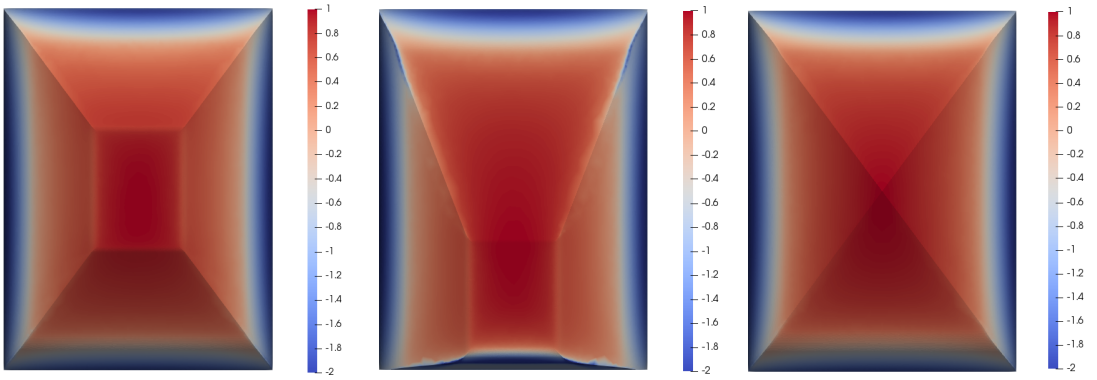

(a) E_S (b) E_S_lowest (c) E_S_point

Figure 6.10: Simulated pressure distribution of different models

The pressure coefficient distribution is shown on the front part of the model. All three models show a large stagnation are near the center of the front. E_S_lowest is a bit different since this model is only symmetrical around the vertical axis. An important difference is the lower part of this model, due to the location of the square, the front edge rounding at the bottom of this model is acting on a very small surface. This is the reason that the flow is not able to stay attached at the bottom front surface, hence the drag coefficient is higher.

6.3.2. ASYMMETRICAL CIRCULAR ROUNDING

The second type of shape variations is asymmetrical rounding at the front edges. The influence of the rounding on the individual surfaces is explored. The models in this section use the E_S model as a basis (illustrated in figure 6.7) and systematically two of the edges are rounded with a different radius. Two examples are shown in the figure 6.11 below.

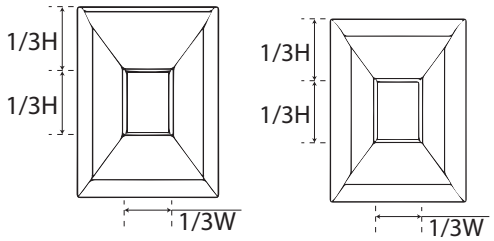

(a) E_top_135 (b) E_Side_810

Figure 6.11: Left, the model with a top radius of 135 mm, all other edges have a radius of 540 mm. Right, the side have a 810 mm radius.

All simulated models are listed in table A.4 of the appendix. All sides are varied between a radius of 135 mm and 810 mm.

DRAG COEFFICIENT

In table 6.5 the results of three models and the baseline model is shown. All C_D values of the models with different rounding are listed in table B.4 of the Appendix. Note that no convergence is obtained for the E_bot_R135 and therefore this model is not listed in the latter table. Observing the results, it is clear that the he influence of the side panels of the front is the largest, the top and bottom behave almost identical.

	0 yaw				3 yaw				6 yaw			
	tot	front	sides	rear	tot	front	sides	rear	tot	front	sides	rear
GR540	0.289	0.018	0.051	0.220	0.299	0.020	0.052	0.226	0.308	0.003	0.056	0.249
E_top_R810	0.289	0.015	0.052	0.222	0.298	0.016	0.054	0.228	0.306	-0.001	0.056	0.250
E_side_R810	0.287	0.013	0.052	0.222	0.297	0.015	0.053	0.228	0.305	-0.002	0.056	0.250
E_bot_R810	0.288	0.015	0.051	0.222	0.296	0.017	0.053	0.227	0.305	0.000	0.056	0.250

Table 6.5: Drag coefficient summary for asymmetrical circular rounded models

The difference between the baseline and the E_Side_R810 is approximately 2 drag counts for all yaw angles, for the E_top_R810 and E_bot_R810 the difference is 1 drag count. At 6 yaw the difference in C_D at the front is most pronounced. The differences between the baseline model and the models with variations in rounding are small, with a maximum difference of 3 drag counts at 6 yaw.

VELOCITY DISTRIBUTION

The velocity distribution for three models is analyzed. The three models are E_top_R135, E_top_R270 and E_top_R810. The trends observed in varying the top edge are also observed when the side and bottom front edge are varied. The velocity distributions are shown in figure 6.12. The trends for the separate rounded models are similar to those of the GETS and EGETS models. The radius of the rounding is crucial for the flow to separate. The flow for model E_top_R135 separates at the front top edge, this is indicated by the negative velocity in figure 6.12(a). After the flow separation bubble the flow reattaches and the boundary layers follow the contours of the model. The flow around the model in figure 6.12(b) stays attached and a prominent suction peak is observed. Model E_top_R810 in figure 6.12(c) shows that by applying a larger radius the suction peak is reduced. The influence on other parts of the model is negligible, the velocity distribution at the bottom of the vehicle is very similar for the different models.

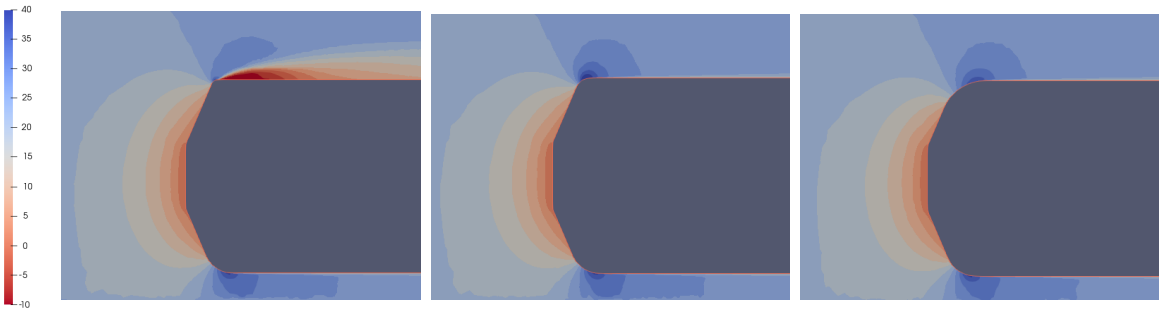

(a) Velocity distribution for model E_top_135 (b) Velocity distribution for model E_top_R270 (c) Velocity distribution for model E_top_R810

Figure 6.12: Velocity distribution in the xy-plane at z = 0 m, measured in m/s for three models with varying top edge radius. The flow is going from left to right.

6.4 Summary

The GETS model is elongated with 500 mm in order to investigate the aerodynamic effects of different frontal shapes. The front edge radius is varied between 0 mm and 1300 mm. A radius of 1300 mm shows the lowest total drag coefficient. The second type of variation used an elliptical rounding. The model with the longest major axis in longitudinal direction is the most beneficial in term of drag coefficient. The third type of front design explores a number of different shapes and these are systematically tested. Only the triangle shaped front showed a small decrease in drag coefficient. In addition, the effect of the rounding on one or two edges is studied. The effect of altering the front side has the largest effect.

When the four types of changes are compared, the change is front edge radius showed the best improvement in C_D compared to the GETS baseline model. However the improvement is relatively small, only five drag counts.

7

DISCUSSION

This chapter presents an analysis of the results of all full scale models. The obtained results will be put into perspective and the broader trends will be discussed. This chapter concludes with a reflection on the aerodynamic benefits and emission reduction of front elongated modern heavy duty trucks.

7.1 Analysis and trends

The simulated results of the non-elongated model and the elongated models will be analyzed using non-dimensional parameters. This is a common method to discover trends between models. As part of this analysis the simulated results will be compared to results of other studies. This chapter starts with an analysis of the GETS models, followed by the analysis of the elongated models. It concludes with an analysis of the boundary layer development and the presentation of the wake length.

7.1.1. FULL SCALE GETS MODEL

The CFD simulations were validated on the 1:15 scale model and subsequently performed on a full scale model. The difference in flow behavior between these models is very small. However, due to the higher Reynolds number and turbulence intensity, small changes were observed in the drag coefficient; the drag coefficient was lower in the full scale model. The causes of the small changes between the 1:15 and full scale model are discussed below.

The higher Reynolds number is discussed first. Wood [3] extensively studied the phenomenon where a higher Reynolds number leads to a lower drag coefficient. As expected, this phenomenon is observed for the 1:15 scale model and the full scale model. The simulated Reynolds number effect for a full scale GETS model is shown in figure 5.6. In this figure the variation in Reynolds number between $0.5 * 10^5$ and $6 * 10^6$ leads to a reduction in drag coefficient of 22 drag counts. These two Reynolds numbers roughly correspond to the Reynolds numbers in the 1:15 and full scale models.

Secondly, the turbulence intensity is discussed. When a 1:15 scale model and a full scale model are compared based on the data of Wood [3], an increase in turbulence level, from 1% to 5%, is expected to offset the drag coefficient reduction by the higher Reynolds number. A total difference in drag coefficient between the small and full scale model of 11 drag counts was observed when both effects are taken into account.

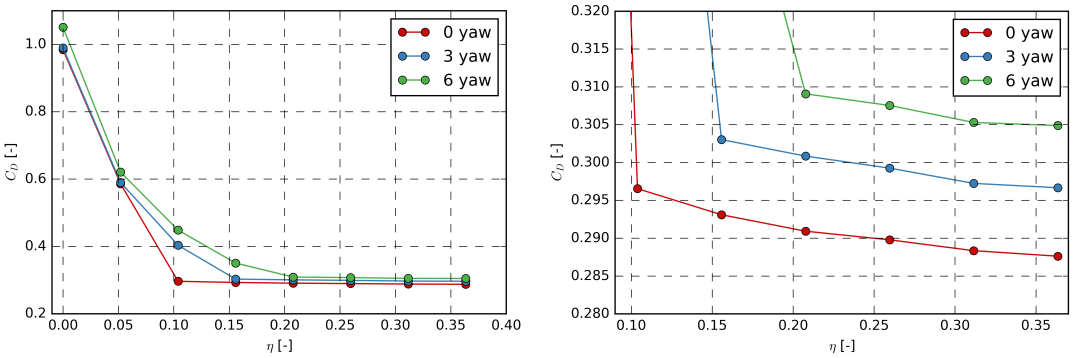

(a) C_D of all GETS models

(b) C_D GETS close up of the models with a larger radii of figure 7.1(a).

Figure 7.1: C_D of the GETS models for 0, 3 and 6 degree yaw

The drag coefficients for the full scale GETS model for 0, 3 and 6 degree yaw angle are shown in figure 7.1. Two main conclusions can be drawn from the results in this figure. Firstly, high drag coefficients are obtained for models which have small front edge radii, especially at high yawing angles. At a yaw angle of 0 degrees, the drag coefficient levels off at a non-dimensional radius of 0.11; at 6 degree yaw this radius is 0.22. In the figure 5.13 it was observed that these large differences in drag coefficient are due to the separation of flow. These results are also found by others like Cooper[4], Newnham [21] and Sakuma [48].

Secondly, only small drag coefficient reductions can be obtained for attached flow. The drag coefficient for attached flow for the GETS models is shown in figure 7.1(b). One can observe a small decline in drag coefficient with an increasing front edge radius. The largest difference for 0 degree yaw is 9 drag counts. This small difference in drag coefficient is translated into a smaller stagnation area at the front of the model, lower suction forces at the front edges of the model and a higher base pressure. This is shown in the pressure distribution in figure 5.15.

7.1.2. FULL SCALE ELONGATED MODELS

The elongated models can be categorized into three categories: the first with a circular front edge rounding, the second with an elliptical front edge rounding and the third category contains a variety of frontal shapes. The models with a circular front edge radius have a radius between $\eta = 0$ and 0.5. A similar variation of front edge radius is applied to the non-elongated models. When the elongated and non-elongated model with the same circular radius are compared, the influence of elongation can be studied. As expected the difference between these models is very small. It is only 1-2 drag counts for all yaw angles and originates mainly from the sides of the model.

For the other two model categories, a minimum front edge radius of 540 mm is applied, such that the effects of attached flow are analyzed for all measured yaw angles. In order to compare the aerodynamic performance of the circular rounding with that of the elliptical rounding a non-dimensional parameter $L2/W$ is defined. $L2$ is the length of the rounding in the longitudinal direction and W represents the width of the model. The drag coefficients at 0 degree yaw of the elongated models with an elliptical front edge, of the non-elongated GETS models and of the elongated GETS model are shown in figure 7.2.

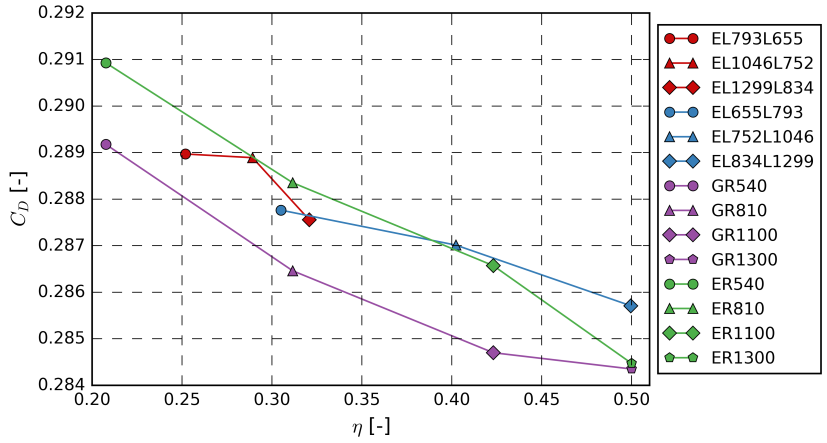

Figure 7.2: The C_D versus the non-dimensional front edge length $L2/W$ for 0 degree yaw.

The differences in C_D between the models are small; the best and the worst model in terms of the drag coefficient differ only 9 drag counts. The round dots represent the models with an elliptical front edge where $L1 > L2$. The difference found is only 3 drag counts. A larger spread is found for the other elliptical front edge round models ($L1 < L2$), represented by the 'x' marker. The EGETS models are shown with a star symbol, these models show an almost linear decrease in drag coefficient when the non-dimensional radius is increased. The GETS models show a converging trend. Both the EGETS and GETS model converge towards a C_D of 0.284 with a $L2/W$ value of 0.5.

When the turbulence model of the simulation, the influence of the assumptions and the mesh differences for different models are taken into account, the results of figure 7.2 have to be interpreted with care. The two equation time-averaged turbulence model (k-ω) has difficulties with predicting the accurate flow properties at the rear. The mesh differences for some models lead to a higher number of cells and a higher number of cells can decrease the drag coefficient slightly as explained in the mesh sensitivity study, section 4.2. Therefore, it is difficult to draw very specific conclusions based on these small differences. A general trend for all models can be observed though: the drag coefficient is decreasing with an increasing radius.

The third category with different front-end designs, a variety of frontal shapes, only shows very small differences between the models. Two models show separated flow, as the front edge radius is too small. The flow for all other models stays attached and the difference between these models is within 3 drag counts. When taking into account that the mesh of these models is slightly different due to the different front-end designs and that the drag differences are so small, no definitive conclusions can be drawn from these different designs.

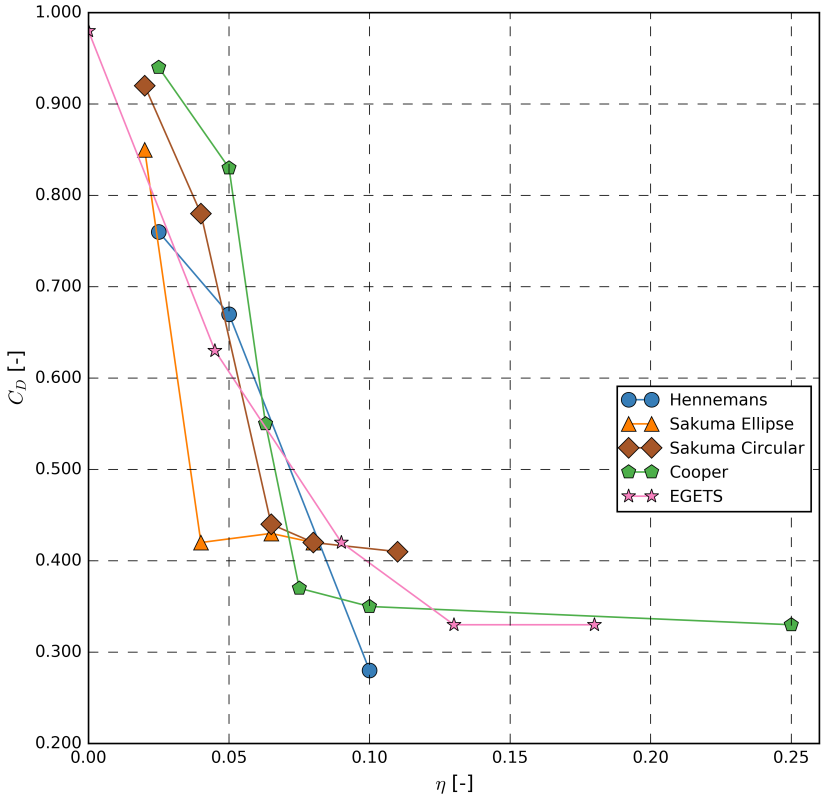

Figure 7.3: C_D versus η comparison for different studies.

7.1.3. BOUNDARY LAYER AND WAKE DEVELOPMENT

At the front of the model the development of the boundary layer originates. The front end thus influences the drag of the fore body but also the drag at the base of the model. This phenomenon is explained by Hoerner and Mariotti. In figure 7.4 the boundary layer thickness is shown as a function of the non-dimensional radius for the EGETS and long elliptical models. The elliptical model has a constant minimum radius of 540 mm and acts between η 0.3 and 0.5. The boundary layer thickness is measured 1 m before the base for both models and 2 m after the front of the model. The GETS and EGETS models peform almost identical, for clarity only the EGETS is shown in the figure.

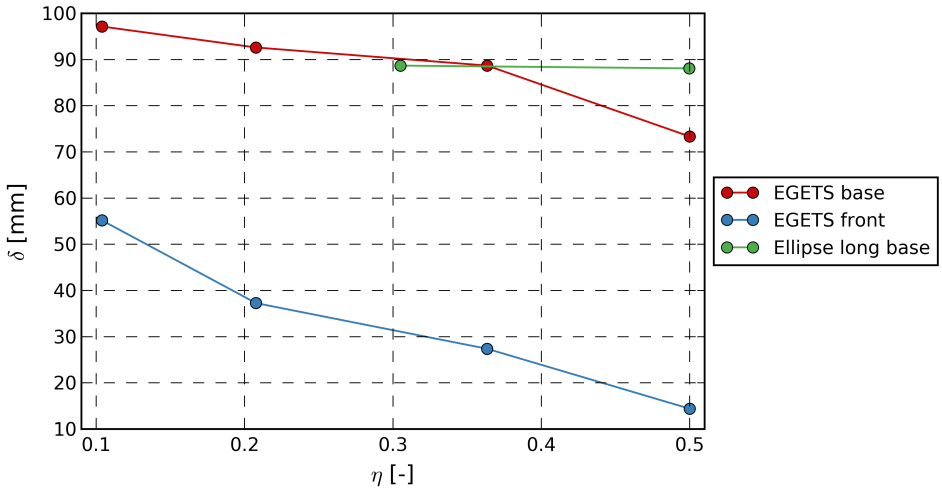

Figure 7.4: Boundary layer thickness versus non-dimensional radius r/W for 0 degree yaw for EGETS models.

For the EGETS model the boundary layer height at the front and rear is decreasing with increasing radius. The boundary layer thickness for the elliptical model is nearly constant. These trends were expected based on the base drag: the base drag of the EGETS models increased with increasing radius, while that of the elliptical models remained virtually constant.

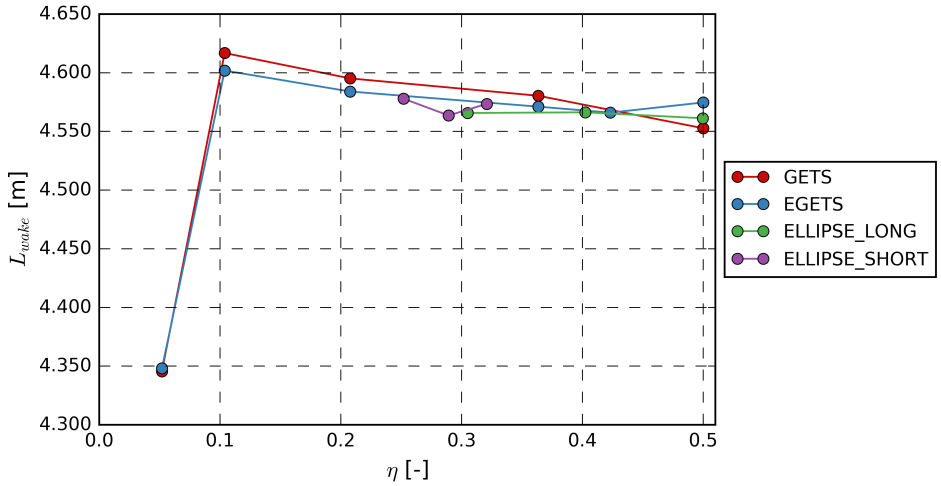

Figure 7.5: Wake length for several models.

A thinner boundary layer is responsible for higher velocities at the separation point at the base and a shorter recirculation region (wake length) as shown by Mariotti [44]. Figure 7.5 shows the wake length versus the non-dimensional radius for various models. The GETS and EGETS model with separated flow have the smallest wake length (η = 0.05). When the flow is attached the wake length is much larger and it decreases slightly with increasing radius. This was expected by the results of Mariotti. The general trend shows an almost linear decrease in wake length for all models.

7.2 Reflection on climate goals

The goal of the new European directives is to reduce the CO_2 equivalent emissions by allowing front elongated vehicles. A front elongation of 500 mm is analyzed in this study, while maintaining most of the original volume of the model. The model with the lowest yaw averaged aerodynamic drag is the EGR1300. Compared to the original GR540 model a benefit of 5 drag counts is realized, at a yaw averaged drag of 3 degrees yaw. This equals a 1.7% reduction in drag coefficient and a roughly 0.85% reduction in CO_2 emissions. The benefits for more realistic and detailed trucks is likely smaller, since the small protuberances, mirrors, air intake and rotating wheels will disturb the smooth flow of the thin boundary layer at the front.

Elongating the truck by 500 mm can roughly be translated into a weight increase of 250 kg, based on a study performed by Eknander in 2013 [73] and based on the weight increase of a DAF XF 105 with an increased wheelbase of 500 mm [74]. The maximum allowable weight limit for CoE trucks in most European states is 40 tonnes in total [73]. An elongation therefore increases the vehicle weight. Subsequently the drag due to rolling resistance is increased by (maximum) 0.6%. It also means that the cargo transport capability is reduced by roughly 1%. Since the drag due to rolling resistance and air drag resistance at high way speeds are roughly equal (45%), the small benefit of elongating the front is negated by the weight penalty of the elongation.

In contrast to model GR540 there is room for improvement for current CoE models. The minimum front edge radius at the sides of the truck are in the range of 100-200 mm [43], meaning flow separation occurs at these regions. Such a modern CoE truck has a similar front edge radius as model E_side_R135. Comparing the E_side_R135 model with an EGR1300 model a drag reduction of 16.3% at a yaw averaged drag of 3 degrees is possible. When the increased rolling resistance is included, this corresponds to a drag force and emission reduction of 6.7%.

Notice that the used models are schematic of nature and therefore the results of more detailed HDV might be lower. A follow up study using more realistic trucks, including an intake, rotating wheels and mirrors is

recommended to better estimate the benefits of a larger front edge radius.

8

CONCLUSION AND RECOMMENDATIONS

8.1 Conclusion

The EU committed itself to reduce the greenhouse gas emissions with respect to the 1990 level. Therefore the EC is proposing new laws which relax the dimensional constraints for truck-trailer combinations. In this study it is investigated whether an elongation can be beneficial for reducing drag and hence reduce emissions. Based on steady state numerical simulations the baseline model and elongated models with different frontal designs are tested.

The numerical simulations are validated using the data from a wind tunnel test. The model in the wind tunnel test is scaled down to 1:15. Numerical data of near wake structures, force coefficients, pressure distributions and boundary layer development are in agreement with the wind tunnel data.

To explore the real-world effects the 1:15 scale results are compared to 1:1 scale models. Small differences between these two models are a result of using different Reynolds numbers and turbulence intensities. Varying the front edge radius of the 1:1 model shows that a critical radius of 540 mm exist for the flow to stay attached at yaw angles of 0, 3 and 6 yaw. Increasing the radius beyond 540 mm shows a minor decrease in drag coefficient, while a large decrease of the stagnation area and suction forces can be observed.

After the analysis of the non-elongated 1:1 models, the models are elongated with 500 mm. Elongating the baseline model increases the drag slightly due to the increased wetted area. The stagnation pressure and suction force do not change when the model is only elongated.

The final part of this research explores several front designs for elongated models. The first effect that is studied is the change in circular radius. The observations found are in line with the observations for non-elongated models: when the radius is larger than the critical radius of 540 mm, the flow stays attached and only a small decrease in drag coefficient is observed. The model with the lowest drag coefficient has a circular radius of 1300 mm, the benefit over the baseline model is 6 drag counts for 3 degree yaw. Second, an elliptical front edge radius is applied. Variations in front edge radius showed minor changes in drag coefficient. Lower drag coefficients are observed when longer axes are chosen, while the minimum radius is kept constant. Finally, various frontal shapes are applied to an elongated model. The benefits of changing the frontal shape are minimal.

When all models variations in this study are taken into account, an overall conclusion can be drawn. The most important parameter for the drag coefficient, which has been studied, is the front edge radius. When the radius is larger than critical radius, the flow stays attached for all models, which reduces the drag coefficient. With a radius larger than the critical radius, the effect of frontal shapes are relatively small.

8.2 Recommendations

The research on bluff body vehicles is far from finished and the research topic of this study can be expanded in various ways, these are stated below.

8.2.1. CFD CONFIGURATION

The model in this discourse had limitations to consider. The found effects of various front designs are small, therefore the impact of the assumption of a steady state simulation with a two parameter turbulence model could skew the simulations. One could overcome this by using a high resolution time-dependent model, like a Detached Eddy Simulation (DES) or Large Eddy Simulation (LES) model.

8.2.2. DETAILED MODEL

The model used in this researched could also be extended in various way. A more detailed model would for example give more information on the gains that can be obtained for realistic heavy duty trucks. This could be achieved by modeling rotating wheels, mirrors and engine cooling systems.

8.2.3. HOLISTIC APPROACH TO DRAG REDUCTION DESIGN

One could also use an holistic approach to the drag reduction design. The effects of changing the front of the truck allow for a change in flow behavior at the rear of the trailer. In the current discourse only changes were made at the front of the truck. If a more holistic approach is used various designs for the front, sides and rear can be tested simultaneously. This could lead to a more overall understanding of the drag reduction possibilities.

A

APPENDIX A - MODEL OVERVIEW

In this chapter an overview of all the models is given.

A.1 GETS models

Modelname	Explanation	Elongation [mm]	fillettype	radius [mm]			
				top	bottom	left	right
GR0	GETS	0	circular	0	0	0	0
GR135	GETS	0	circular	135	135	135	135
GR270	GETS	0	circular	270	270	270	270
GR405	GETS	0	circular	405	405	405	405
GR540	Basline GETS	0	circular	540	540	540	540
GR675	GETS	0	circular	675	675	675	675
GR810	GETS	0	circular	810	810	810	810
GR945	GETS	0	circular	945	945	945	945
GR1100	GETS	0	circular	1100	1100	1100	1100
GR1300	GETS	0	circular	1300	1300	1300	1300

Table A.1: Model properties of non-elongated models with a circular front edge radius

A.2 EGETS circular models

Modelname	Explanation	Elongation [mm]	fillettype	radius [mm]			
				top	bottom	left	right
ER0	EGETS	500	circular	0	0	0	0
ER135	EGETS	500	circular	135	135	135	135
ER270	EGETS	500	circular	270	270	270	270
ER405	EGETS	500	circular	405	405	405	405
ER540	EGETS	500	circular	540	540	540	540
ER675	EGETS	500	circular	675	675	675	675
ER810	EGETS	500	circular	810	810	810	810
ER945	EGETS	500	circular	945	945	945	945
ER1100	EGETS	500	circular	1100	1100	1100	1100
ER1300	EGETS	500	circular	1300	1300	1300	1300

Table A.2: Model properties of elongated models with a circular front edge radius

A.3 EGETS elliptical models

Modelname	Explanation	Elongation [mm]	fillettype	radius [mm]			
				top	bottom	left	right
ELR793-L655	Ellipse (short)	500	elliptical	793/655	793/655	793/655	793/655
EL1046-L752	Ellipse (short)	500	elliptical	1046/752	1046/752	1046/752	1046/752
EL1299-L834	Ellipse (short)	500	elliptical	1299/834	1299/834	1299/834	1299/834
EL655-L793	Ellipse (long)	500	elliptical	655/793	655/793	655/793	655/793
EL752-L1046	Ellipse (long)	500	elliptical	752/1046	752/1046	752/1046	752/1046
EL834-L1299	Ellipse (long)	500	elliptical	834/1299	834/1299	834/1299	834/1299

Table A.3: Model properties of elongated models with an elliptical front edge radius

A.4 EGETS asymmetrical models

Modelname	Explanation	Elongation [mm]	fillettype	radius [mm]			
				top	bottom	left	right
E-R-T-135	Top edge	500	circular	540	540	540	540
E-R-T-270	Top edge	500	circular	540	540	540	540
E-R-T-405	Top edge	500	circular	540	540	540	540
E-R-T-810	Top edge	500	circular	540	540	540	540
E-R-S-135	Side Edge	500	circular	540	135	540	135
E-R-S-270	Side Edge	500	circular	540	270	540	270
E-R-S-405	Side Edge	500	circular	540	405	540	405
E-R-S-810	Side Edge	500	circular	540	810	540	810
E-R-B-135	Bottom Edge	500	circular	135	540	540	540
E-R-B-270	Bottom Edge	500	circular	270	540	540	540
E-R-B-405	Bottom Edge	500	circular	405	540	540	540
E-R-B-810	Bottom Edge	500	circular	810	540	540	540

Table A.4: Model properties of elongated models with an asymmetrical circular front edge radius

A.5 EGETS frontal shapes

Modelname	Explanation	Elongation [mm]	fillettype	radius [mm]			
				top	bottom	left	right
E_S	Square	500	circular	540	540	540	540
E_S_up	Square High	500	circular	540	540	540	540
E_S_down	Square Low	500	circular	540	540	540	540
E_S_lowest	Square Lowest	500	circular	540	540	540	540
E_S_taller	Square Taller	500	circular	540	540	540	540
E_S_shorter	Square Shorter	500	circular	540	540	540	540
E_S_wider	Square Widest	500	circular	540	540	540	540
E_S_smaller	Square Smaller	500	circular	540	540	540	540
E_S_wide	Square Wide	500	circular	540	540	540	540
E_S_point	Point	500	circular	540	540	540	540
E_S_vline	Vertical Line	500	circular	540	540	540	540
E_S_triangle	Triangle	500	circular	540	540	540	540
E_S_ellipse	Ellipse	500	circular	540	540	540	540
E_S_hline	Horizontal Line	500	circular	540	540	540	540

Table A.5: Model properties of elongated models with various front designs

B

APPENDIX B - SIMULATION RESULTS

The results for all models are shown in the tables in this section for 0, 3 and 6 yaw.

B.1 GETS circular front egde radius

	0 yaw				3 yaw				6 yaw			
Modelname	tot	front	sides	rear	tot	front	sides	rear	tot	front	sides	rear
GR0	0.958	0.789	0.015	0.155	0.963	0.786	0.016	0.161	1.024	0.784	0.024	0.217
GR135	0.584	0.358	0.037	0.189	0.586	0.355	0.036	0.196	0.620	0.347	0.041	0.232
GR270	0.294	0.027	0.050	0.218	0.385	0.114	0.049	0.222	0.448	0.147	0.053	0.248
GR405	0.292	0.022	0.050	0.220	0.302	0.024	0.052	0.226	0.351	0.051	0.054	0.247
GR540	0.289	0.018	0.051	0.220	0.299	0.020	0.052	0.226	0.308	0.003	0.056	0.249
GR675	0.288	0.016	0.051	0.221	0.297	0.018	0.052	0.227	0.306	0.001	0.055	0.249
GR810	0.286	0.014	0.051	0.222	0.296	0.016	0.052	0.227	0.304	-0.001	0.055	0.250
GR945	0.286	0.013	0.050	0.222	0.295	0.015	0.052	0.228	0.303	-0.002	0.055	0.251
GR1100	0.285	0.011	0.050	0.223	0.294	0.013	0.052	0.229	0.302	-0.004	0.055	0.251
GR1300	0.284	0.010	0.050	0.224	0.293	0.012	0.051	0.230	0.301	-0.005	0.054	0.252

Table B.1: Numerical results for the non-elongated models with a circular front edge radius

B.2 EGETS circular front egde radius

	0 yaw				3 yaw				6 yaw			
Modelname	tot	front	sides	rear	tot	front	sides	rear	tot	front	sides	rear
EGR0	0.985	0.815	0.015	0.154	0.990	0.814	0.016	0.159	1.051	0.812	0.024	0.215
EGR135	0.586	0.358	0.039	0.190	0.590	0.356	0.038	0.196	0.621	0.346	0.042	0.232
EGR270	0.297	0.028	0.051	0.218	0.404	0.133	0.050	0.221	0.449	0.146	0.054	0.248
EGR405	0.293	0.023	0.052	0.219	0.303	0.025	0.053	0.225	0.351	0.045	0.056	0.249
EGR540	0.291	0.019	0.052	0.220	0.301	0.021	0.054	0.226	0.309	0.004	0.057	0.249
EGR675	0.290	0.016	0.053	0.221	0.299	0.018	0.054	0.227	0.308	0.001	0.057	0.250
EGR810	0.288	0.015	0.052	0.222	0.297	0.017	0.054	0.227	0.305	-0.001	0.057	0.249
EGR945	0.288	0.013	0.052	0.222	0.297	0.015	0.053	0.228	0.305	-0.002	0.056	0.250
EGR1100	0.287	0.011	0.052	0.223	0.296	0.013	0.053	0.229	0.304	-0.004	0.056	0.251
EGR1300	0.284	0.011	0.051	0.223	0.293	0.013	0.053	0.228	0.301	-0.004	0.055	0.250

Table B.2: Drag coefficients for the elongated models with a circular front edge radius

B.3 EGETS elliptical front egde radius

	0 yaw				3 yaw				6 yaw			
	tot	front	sides	rear	tot	front	sides	rear	tot	front	sides	rear
ER793R655	0.289	0.014	0.053	0.222	0.298	0.016	0.054	0.228	0.306	-0.001	0.057	0.250
ER1046R752	0.289	0.014	0.053	0.223	0.298	0.015	0.054	0.229	0.306	-0.002	0.057	0.251
ER1299R834	0.288	0.013	0.052	0.222	0.297	0.015	0.054	0.228	0.305	-0.002	0.057	0.250
ER655R793	0.288	0.013	0.052	0.222	0.297	0.015	0.054	0.228	0.305	-0.002	0.057	0.250
ER752R1046	0.287	0.012	0.052	0.223	0.296	0.014	0.053	0.229	0.304	-0.003	0.056	0.251
ER834R1299	0.286	0.011	0.051	0.223	0.295	0.013	0.053	0.229	0.302	-0.004	0.055	0.251

Table B.3: Drag coefficients for the elongated models with a elliptical front edge radius

B.4 EGETS asymmetrical front edge rounding

	0 yaw				3 yaw				6 yaw			
	tot	front	sides	rear	tot	front	sides	rear	tot	front	sides	rear
E_top_R135	0.315	0.044	0.051	0.220	0.323	0.044	0.052	0.227	0.330	0.025	0.055	0.249
E_top_R270	0.290	0.016	0.052	0.222	0.299	0.018	0.053	0.228	0.308	0.001	0.057	0.250
E_top_R405	0.289	0.015	0.052	0.222	0.298	0.017	0.053	0.227	0.307	0.000	0.056	0.250
E_top_R810	0.289	0.015	0.052	0.222	0.298	0.016	0.054	0.228	0.306	-0.001	0.056	0.250
E_side_R135	0.295	0.023	0.051	0.221	0.349	0.076	0.050	0.222	0.405	0.104	0.053	0.248
E_side_R270	0.292	0.018	0.052	0.222	0.301	0.020	0.053	0.227	0.335	0.033	0.055	0.247
E_side_R405	0.290	0.016	0.052	0.222	0.299	0.018	0.053	0.228	0.308	0.001	0.056	0.250
E_side_R810	0.287	0.013	0.052	0.222	0.297	0.015	0.053	0.228	0.305	-0.002	0.056	0.250
E_bot_R270	0.289	0.015	0.052	0.222	0.299	0.017	0.054	0.228	0.307	0.000	0.057	0.251
E_bot_R405	0.289	0.015	0.052	0.222	0.298	0.017	0.053	0.228	0.306	0.000	0.057	0.250
E_bot_R810	0.288	0.015	0.051	0.222	0.296	0.017	0.053	0.227	0.305	0.000	0.056	0.250

Table B.4: Drag coefficients for the elongated models with an asymmetrical circular front edge radius

B.5 EGETS frontal shapes

	0 yaw				3 yaw				6 yaw			
	tot	front	sides	rear	tot	front	sides	rear	tot	front	sides	rear
E_S	0.289	0.015	0.052	0.222	0.298	0.017	0.053	0.228	0.307	0.000	0.056	0.250
E_S_lowest	0.301	0.030	0.051	0.220	0.310	0.032	0.052	0.225	0.319	0.016	0.055	0.249
E_S_down	0.288	0.015	0.052	0.222	0.298	0.017	0.053	0.228	0.306	0.000	0.056	0.250
E_S_up	0.291	0.017	0.052	0.222	0.300	0.019	0.053	0.227	0.309	0.003	0.056	0.250
E_S_wider	0.299	0.026	0.051	0.222	0.308	0.029	0.052	0.226	0.327	0.025	0.054	0.248
E_S_wide	0.291	0.017	0.052	0.222	0.300	0.019	0.053	0.227	0.308	0.002	0.056	0.250
E_S_small	0.289	0.014	0.052	0.222	0.298	0.016	0.054	0.228	0.306	-0.001	0.057	0.250
E_S_taller	0.291	0.020	0.051	0.220	0.300	0.022	0.052	0.226	0.308	0.005	0.055	0.248
E_S_shorter	0.291	0.016	0.052	0.223	0.299	0.018	0.053	0.228	0.308	0.001	0.056	0.250
E_S_point	0.289	0.015	0.052	0.222	0.298	0.017	0.053	0.228	0.306	0.000	0.056	0.250
E_S_vline	0.288	0.014	0.052	0.222	0.297	0.016	0.053	0.227	0.305	-0.001	0.057	0.250
E_S_triangle	0.286	0.014	0.051	0.222	0.295	0.016	0.052	0.227	0.304	-0.001	0.055	0.250
E_S_ellipse	0.288	0.014	0.052	0.221	0.297	0.016	0.054	0.227	0.305	-0.001	0.057	0.250
E_S_hline	0.292	0.018	0.052	0.222	0.300	0.020	0.053	0.227	0.309	0.003	0.056	0.250

Table B.5: Drag coefficients for the elongated models with various front designs

C

APPENDIX C - MESH OVERVIEW

In this section the mesh is shown for the 1:15 scale model and the 1:1 model for the GETS model. The mesh is build using ANSYS ICEM. Every mesh is tested for three important mesh quality characteristics: aspect ratio, orthogonality and skewness. When the mesh fails for one of these test the mesh is locally refined or smoothed. Recommendations for the quality tests are extensively discussed in the ANSYS Fluent Manuel [7] and by Lanfrit [63].

C.1 1:15 scale model

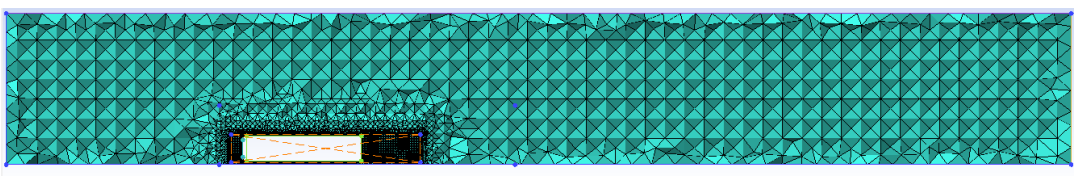

Figure C.1: Mesh overview 1:15, sideview. The orange dotted lines indicated the refined cells of the density box.

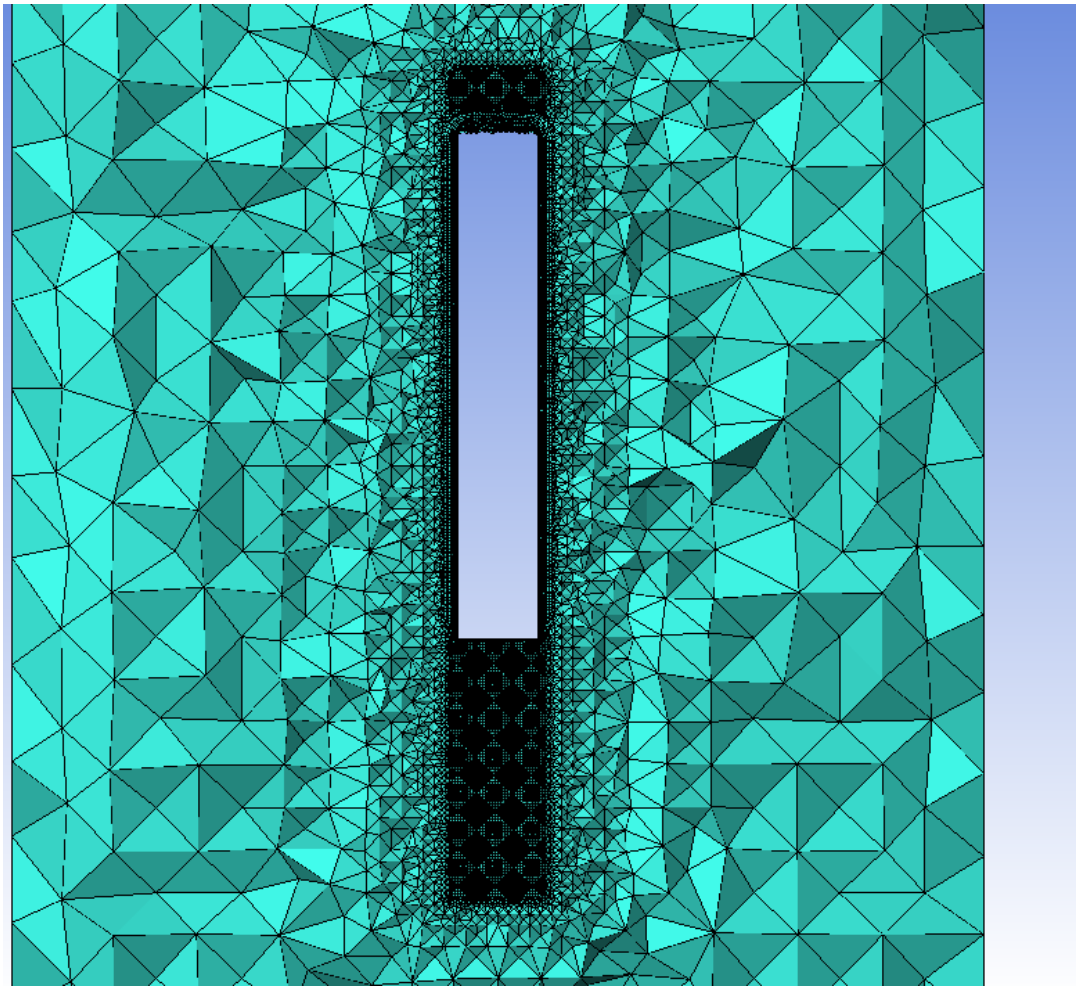

Figure C.2: Mesh overview 1:15, topview. The refinement area is extra wide to account for side wide.

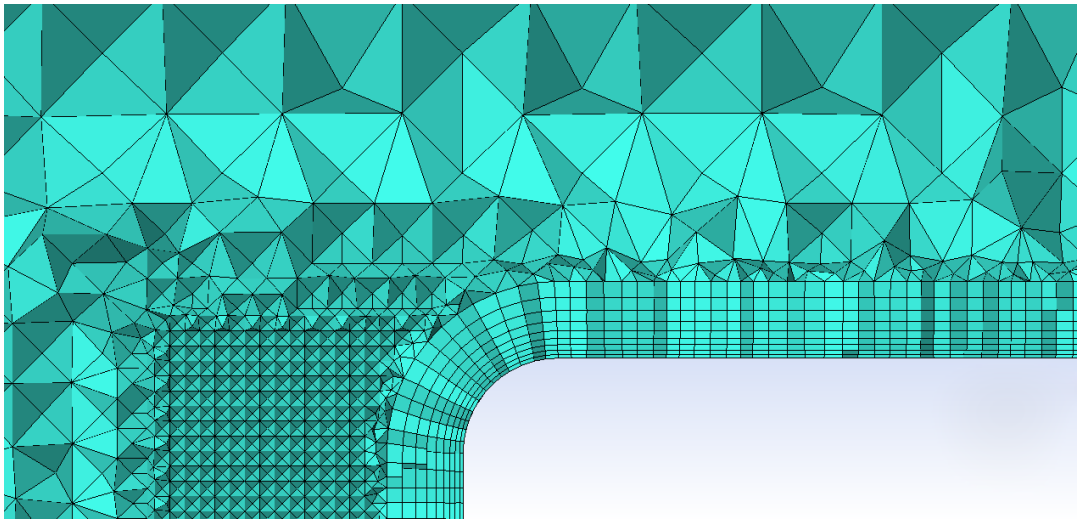

Figure C.3: Closeup of the mesh at the front of the 1:15 scale model, sideview. At the left part of the density box is shown. Note that the inflation layers around the models increase with 20% per layer. The cell size difference between the tetrahedral elements and the last inflation layer should be small in order to accurately simulate the flow.

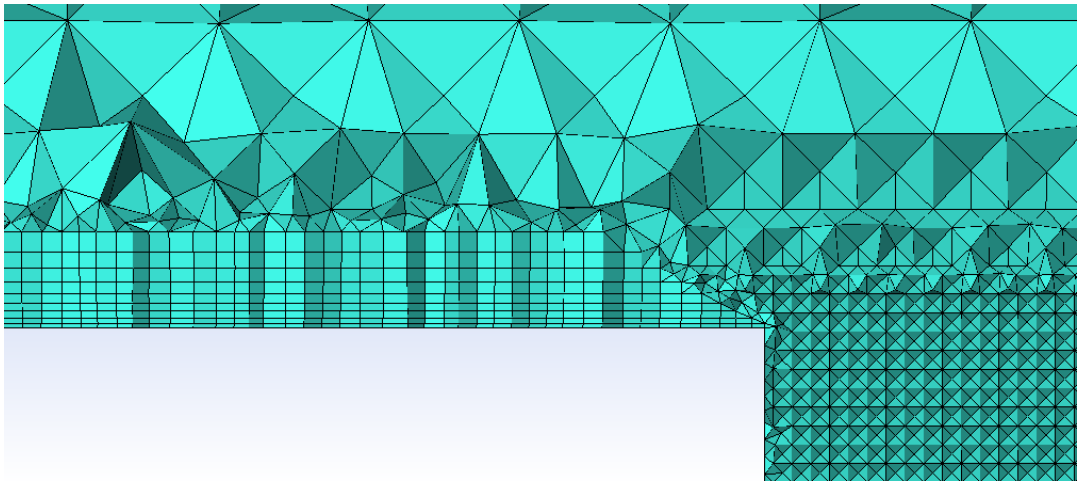

Figure C.4: Closeup of the mesh at the base of the 1:15 scale model, sideview. At the base of the 1:15 scale model no inflation layers are positioned. Therefore side structured cells are gradually decreasing using a stair step method in ANSYS ICEM.

C.2 1:1 scale GR540 model

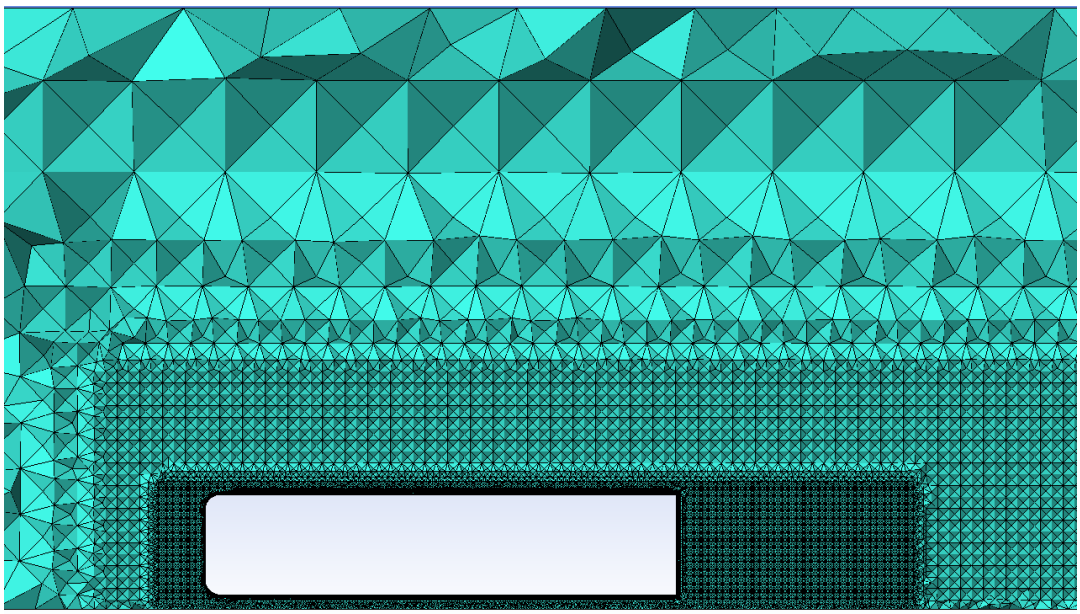

Figure C.5: Mesh overview 1:1, sideview. The inner and outer density box can be observed clearly, the used cell mesh size is 7 mm for the inner density box and 56 mm for the outerbox.

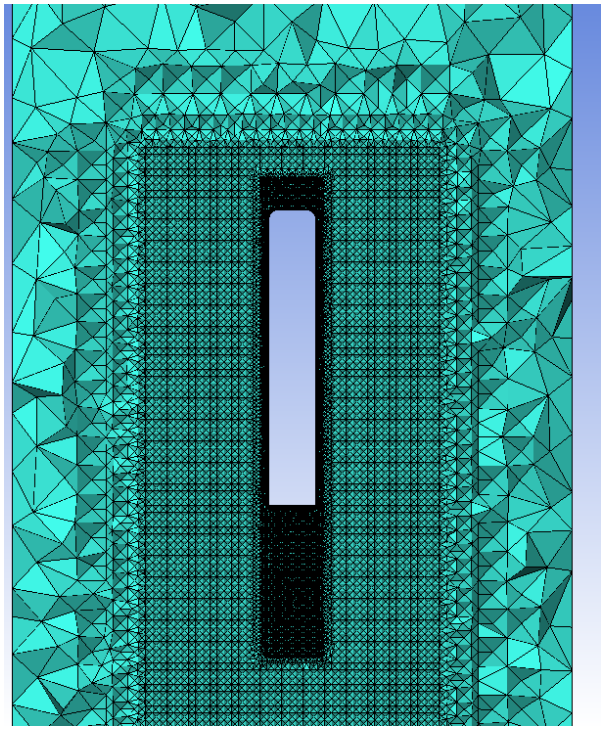

Figure C.6: Mesh overview 1:1, topview. The longitudinal shape of the density boxes are used to capture the wake of the flow with high detail.

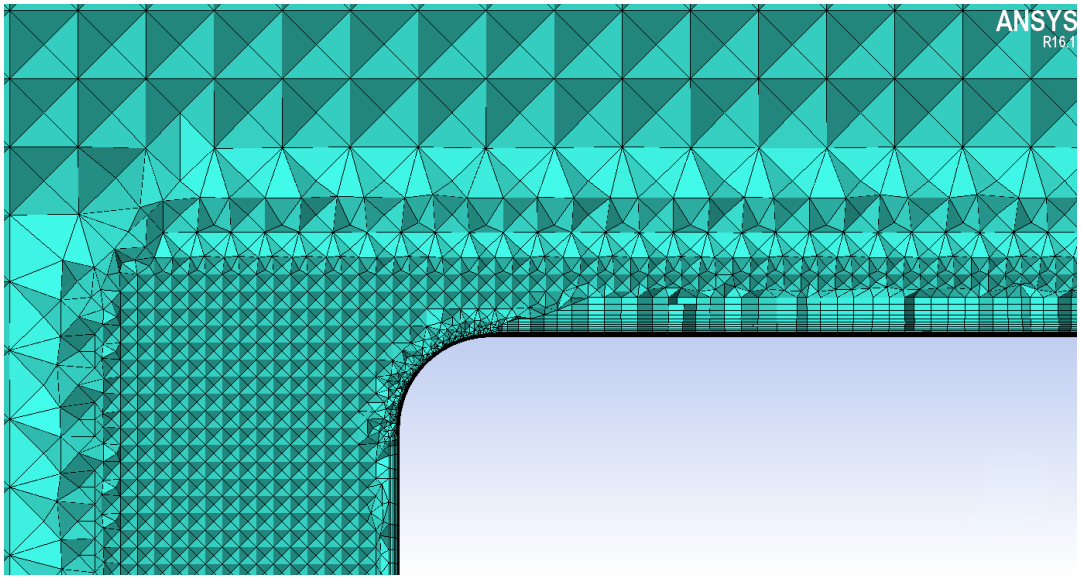

Figure C.7: Closeup of the mesh at the front of the 1:1 scale model, sideview. At the 'front middle' surface large mesh cells are used, while at the edges smaller cells sizes are used. The cell sizes are manipulated according to the local flow velocities, such to produce y^+ values close to 30.

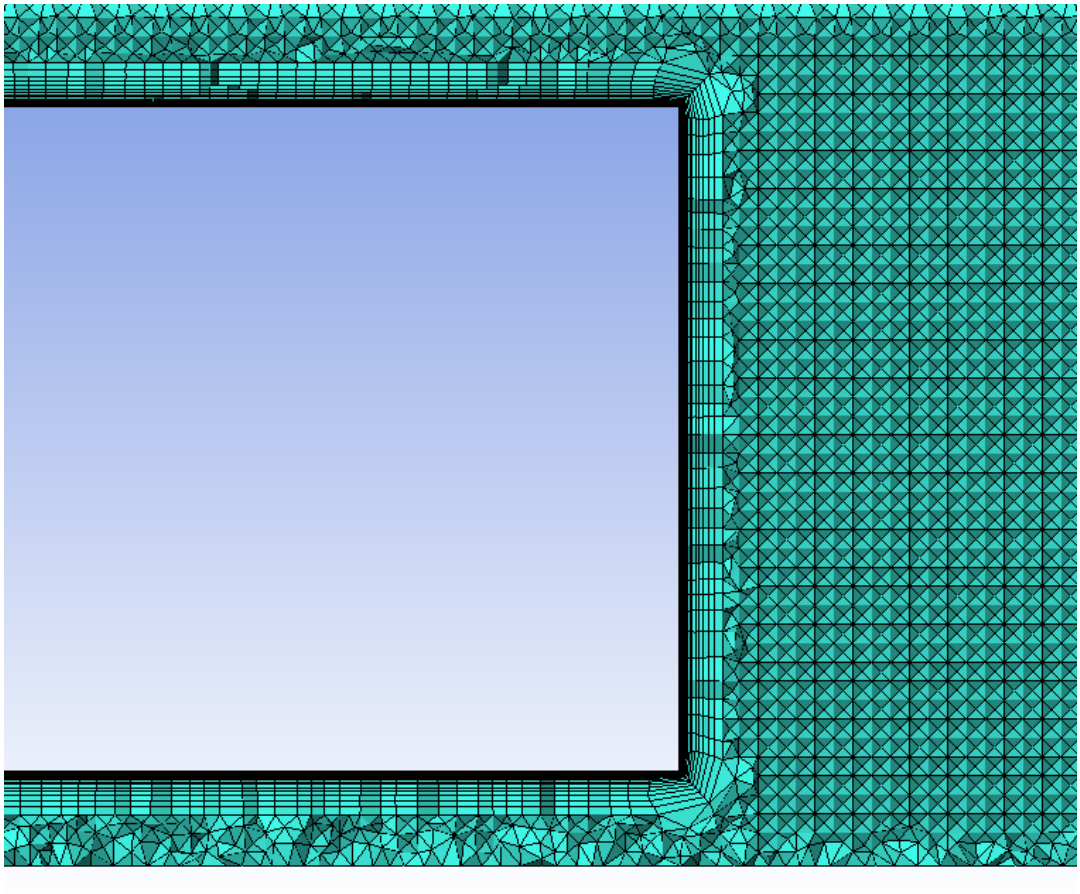

Figure C.8: Closeup of the mesh rear of the 1:1 scale model, sideview. For the 1:1 scale models it was found that using structured cell at the rear of the model increases the quality of the mesh cells. The cost of adding these small structured layers was less than 8% of the total amount of mesh cells.

D

WIND TUNNEL SETUP

The wind tunnel experiments were conducted in the Low Turbulence Tunnel (LTT) at Delft University of Technology by Van Raemdonck [31]. The tunnel has a closed octagonal test section with dimensions shown in table D.1. A mechanical balance system measures the aerodynamic forces and pressures. The tests were conducted with the maximum turbulence intensity. The ground board is a fixed elevated ground board, with added trigger tape to provide a uniform boundary layer development on the ground board.

Blockage corrections for drag (C_T) are calculated using the correction method of Merker, this method is based on classical theory for streamlined shapes. For correction of the pressure coefficient, the method of Thom and Herriot is applied, as recommended by SAE Special Report 1176 [75]. These corrections correct the obtained wind tunnel data for wall interference, therefore using these corrections, a CFD simulation can be performed without modeling the wind tunnel walls.

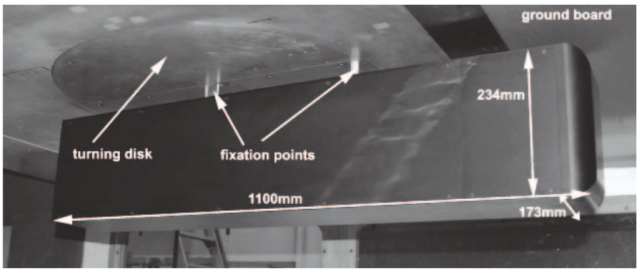

Figure D.1: Photograph of the wind tunnel setup.

Volume	Relative length
Cross sectional area	2,07m^2
Height	1,25m
Width	1,8m
Operating velocity	0-120 m/s
Turbulence Intensity	0,02-0,1 %
Yaw angle	0-10°

Table D.1: Wind tunnel parameters

A consequence of using a scaled down model is that the Reynolds number is lower compared to the 1:1 model, this could have an effect on the aerodynamic performance.

BIBLIOGRAPHY

[1] European Commission, *EU transport in figures* (Publication Office of the European Union, 2016).

[2] DOT, *Quick Guide to Truck Aerodynamics*, Tech. Rep. (Department of Transport UK, 2009).

[3] R. Wood, *A review of reynolds number effect on the aerodynamics of commercial ground vehicles,* SAE International Journal of Commercial Vehicles **01**, 628 (2012).

[4] K. R. Cooper, *The effect of front-edge rounding and rear-edge shaping on the aerodynamic drag of bluff vehilces in ground proximity,* SAE Techinal Paper (1985), 850288.

[5] B. Weatherly, *Upfront advantages,* `http://archive.commercialmotor.com/article/19th-november-2009/48/upfront-advantages` (2009).

[6] S. B. Pope, *Turbulent Flows* (Cambridge University Press, 2000).

[7] ANSYS Inc., *ANSYS FLUENT 16.0 User's Guide*, ANSYS Inc. (2016).

[8] European Commission, *Taking stock of the europe 2020 strategy for smart, sustainable and inclusive growth,* `http://eur-lex.europa.eu/legal-content/EN/ALL/?uri=CELEX:52014DC0130R(01)` (2014).

[9] European Commission, *White paper roadmap to a single european transport area towards a competitive and resource efficient transport system,* `http://eur-lex.europa.eu/legal-content/EN/TXT/PDF/?uri=CELEX:52011DC0144&from=EN` (2011).

[10] K. R. Cooper, *The Aerodynamics of Heavy Vehicle Trucks, Buses, and Trains*, 1st ed., edited by R. McCallen, F. Browand, and J. Ross, 19 (Springer-Verlag Berlin Heidelberg, 2004) pp. 9–28.

[11] R. Muncrief and B. Sharpe, *Overview of the Heavy duty Vehicle Market and CO2 Emissions in the European Union*, Tech. Rep. 6 (International Council on Clean Transportation, 2015).

[12] European Commission, *96/53/ec - laying down for certain road vehicles circulating within the community the maximum authorised dimensions in national and international traffic and the maximum authorised weights in international traffic,* (2015).

[13] T. Frank and J. Turney, *Aerodynamics of commercial vehicles,* in *The Aerodynamics of Heavy Vehicles III*, edited by A. D. D. Orellano (Springer, 2016).

[14] J. Y. Wong, *Theory of Ground Vehicles*, 4th ed., edited by J. Y. Wong (John Wiley & Sons, 2008).

[15] Daimler, *Recovery Act – Class 8 Truck Freight Efficiency Improvement Project*, Tech. Rep. (Daimler Trucks North America, 2015).

[16] J. Barrand and J. Bokar, *Reducing tire rolling resistance to save fuel and lower emissions*, SAE Technical Paper 2008-01-0154 (Michelin AND SAE, 2008).

[17] Y. Xiong and A. Tuononen, *Rolling deformation of truck tires: Measurement and analysis using a tire sensing approach,* Journal of Terramechanics **61**, 33 (2015).

[18] F. Grosche and G. Meier, *Research at dlr goettingen on bluff body aerodyanmics, drag reduction by wake ventilation and active flow control,* Journal of Wind Engineering and Industrial Aerodyanmics **98**, 1201 (2001).

[19] W. Hucho and G. Sovran, *Aerodynamics of road vehicles,* Annu. Rev. Fluid Mech **25**, 485 (1993).

[20] H. Götz, *Present and future trends in automotive aerodynamics,* Short Course (1984), von Karman Institute.

[21] P. Newnham, *The Influence of Turbulence on the Aerodynamic Optimisation of Bluff Body Road Vehicles*, Ph.D. thesis, Loughborough University (2007).

[22] B. Hennemans, *Modeling of front edge flow separation on rounded bluff bodies using commercial CFD software*, Master's thesis, Delft University of Technology (2005).

[23] A. Roshko, *Perspectives on bluff body aerodynamics,* Journal of Wind Engineering and Industrial Aerodynamics **49**, 70 (1993).

[24] D. Hummel, *Aerodynamics of Road Vehicles*, edited by W.-H. Hucho (Butterworth-Heinemann, 1987).

[25] E. Duell and A. George, *Experimental study of a ground vehicle body unsteady near wake*, Tech. Rep. 1999-01-0812 (SAE, 1999).

[26] M. Pastoor, L. Henning, B. Noack, R. King, and G. Tadmor, *Feedbck shear layer control for bluff body drag reduction,* Journal of Fluid Mechanics **608**, 161 (2008).

[27] S. Hoerner, *Fluid Dynamic Drag*, edited by 2 (Hoerner Fluid Dynamics, 1965).

[28] E. J. Saltzman, *Drag reduction obtained by modifying a box-shaped ground vehicle*, Technical Report NASA-TM-X-56027 (NASA Flight Research Center Edwards, California, 1974).

[29] C. Diebler and M. Smith, *A Ground-Based Research Vehicle for Base Drag Studies at Subsonic Speeds*, Tech. Rep. NASA/TM-2002-210737 (NASA Dryden Flight Research Center, 2002).

[30] T. Gheyssens, *Aerodyanmic Analysis of a Platoon of Bluff Bodies Subjected to Cross Wind*, A numerical investigation on the effect of drag reduction devices, Delft University of Technology (2016).

[31] G. van Raemdonck, *Design of Low Drag Bluff Road Vehicles*, Ph.D. thesis, Delft University of Technology (2012).

[32] J. Leuschen and K. Cooper, *Full-scale wind tunnel tests of production and prototype, second-generation aerodyanmic drag-reduction devices for tractor-trailer,* National Research Council (SAE International, 2006).

[33] R. Milhelic, D. Schaller, and M. Roeth, *Confidence report on trailer aerodynamic device solutions,* (2016).

[34] B. R. McAuliffe, *Improving the Aerodynamic Efficiency of Heavy Duty Vehicles: Wind Tunnel Test Results of Trailer-Based Drag-Reduction Technologies*, Tech. Rep. LTR-AL-2015-0272 (National Research Council Canada, 2015).

[35] Frank, *Parameterstudie an einem Fahrerhaus*, Tech. Rep. (Technischer Bericht Daimler-Chrysler, 2001).

[36] P. van Leeuwen, *Computational Analysis of Base Drag Reduction Using Active Flow Control*, Master's thesis, Delft University of Technology (2009).

[37] A. Seifert, T. Shtendel, and D. Dolgopyat, *From lab to full scale active flow control drag reduction: How to bridge the gap?* Journal of Wind Engineering and Industrial Aerodyanmics **147**, 262 (2015).

[38] M. Maciejewski, *Does an active adjustment of aerodynamic drag make sense?* in *IOP Conf. Series: Materials Science and Engineering*, 148, edited by I. Publishing (IOP Publishing, 2016).

[39] T. Schutz, *Fahrzeug-aerodynamik* (Springer Vieweg, 2016).

[40] V. Mali, *Basics of y plus, boundary layer and wall function in turbulent flows,* `https://learncax.com/knowledge-base/blog/by-category/cfd/basics-of-y-plus-boundary-layer-and-wall-function-in-turbulent-flows` (2016).

[41] A. Sommerfeld, *Ein beitrag zur hydrodynamischen erklerung der turbulenten flussigkeitsbewegungen,* in *International Congress of Mathematicians*, Vol. 3 (1908) pp. 116–124.

[42] A. Gilhaus, *The influence of cab shape on air drag of trucks,* Journal of Wind Engineering and Industrial Aerodyanmics **9**, 77 (1981).

[43] A. Devesa and T. Indinger, *Verbrauchreduktion an nutzfahrzeugkombinationen durch aerodynamische massnahmen,* VDA-FAT **237** (2011).

[44] A. Mariotti and G. Buresti, *Experimental investigation on the influence of boundary layer thickness on the base pressure and near-wake flow features of an axisymmetric blunt-base body,* Experiments in Fluids **54**, 1612 (2013).

[45] E. J. Saltzman and R. R. Meyer, *A Reassessment of Heavy-Duty Truck Aerodynamic Design Features and Priorities*, Tech. Rep. (NASA Dryden Flight Research Center, 1999) nASA/TP-1999-206574.

[46] H. Nakaguchi, *Aerodynamic drag mechanisms of bluff bodies and road vehicles,* (Springer US, 1978) Chap. Recent Japanese Research on Three-Dimensional Bluff-Body Flows Relevant to Road Vehicle Aerodynamics, pp. 227–252.

[47] H. Götz, *On the aerodynamic development of the experimental vehicles c 111 i-iv(mercedes),* Journal of wind engineering and industrial aerodynamics **9**, 3 (1981).

[48] Y. Sakuma and A. Ido, *Wind tunnel experiments on reducing separated flow region tunnel around front ends of vehicles on meter -gauge railway lines,* QR of RTRI **50**, 20 (2009).

[49] P. Erlofsson, *Experimental methods in vehicle aerodynamics,* (2007), scania Presentation.

[50] H. Martini, *Perspectives of Aerodynamic Drag and Cooling Airflow of Heavy-Duty Trucks - Reconsidering Europe Total-Length Legislation*, Ph.D. thesis, Chalmers University of Technology (2016).

[51] H. Martini, P. Gullberg, and L. Lofdahl, *Comparative studies between cfd and wind tunnel measurements of cooling performance and external aerodynamics for a heavy truck,* SAE International Journal of Commercial Vehicles **7** (2014), 10.4271/2014-01-2443.

[52] Hjelm, *The aerodynamics of heavy vehicles ii: Trucks, buses, and trains,* (Springer, 2009) Chap. European Truck Aerodynamics - A Comparison Between Conventional and CoE Truck Aerodynamics and a Look into Future Trends and Possibilities, pp. 469 – 477.

[53] J. D. Anderson, *Fundamentals of Aerodynamics*, 3rd ed. (McGraw-Hill, New York, 2013).

[54] W. Mulkens, *Aerodyanmic Analysis of Drag Reduction Devices for the Tractor-Trailer Gap,* An experimental and numerical analysis, Delft University of Technology (2016).

[55] S. A. J. Jansen, *A Feasibility Study on the Aerodyanmic Concept of the Blueliner*, Master's thesis, Delft University of Technology (2013).

[56] H. Choi, J. Lee, and H. Park, *Aerodynamics of heavy vehicles,* Annual Review of Fluid Mechanics **46**, 441 (2014).

[57] D. Pointer, T. Sofu, J. Chang, and D. Weber, *Applicability of commercial cfd tools for assessment of heavy vehicle aerodynamic characteristics,* in *The Aerodynamics of Heavy Vehicles II: Trucks, Buses, and Trains*, edited by F. Browand, R. McCallen, and J. Ross (Springer Berlin Heidelberg, 2009).

[58] S. Veluri, C. Roy, A. Ahmed, and R. RIfki, *Preliminary rans simulations and experimental study of a simplified tractor trailer geometry,* in *24th Applied Aerodynamics Conference*, AIAA 2006-3857 (2006).

[59] S. Nalanagula and G. T. Varadharajan, *Aerodynamics Drag Reduction Methodology for the Commercial Vehicles Using Computational Fluid Dynamics*, SAE Technical Paper 2016-01-8139 (KPIT Technologies, 2016).

[60] S. Veluri and C. Roy, *Joint computational/experimental aerodyanmic study of a simplified tractor/trailer geometry,* Journal of Fluids Engineering **131** (2009), 10.1115/1.3155995.

[61] SAE, *Surface vehicle recommended Practice Guidelines for Aerodynamic Assessment of Medium and Heavy Commercial Ground Vehicles Using Computational Fluid Dynamics*, Tech. Rep. J2966 SEP2013 (SAE International, 2013).

[62] A. Hyvärinen, *Investigation of blockage correctino methods for full-scale wind tunnel testing of trucks*, Master's thesis, KTH, Royal Institute of Technology (2015).

[63] M. Lanfrit, *Best practice guidelines for handling Automotive External Aerodynamics with FLUENT*, Best Practice Guideline 1.2 (Fluent Deutschland GmbH, 2005).

[64] G. van Raemdonck and M. van Tooren, *Time-averaged phenomenological investigation of a wake behind a bluff body,* (2008).

[65] B. Storms, Ross, Heineck, and Walker, *An experimental study of the ground transportation system (gts) model in the nasa ames 7- by 10-ft wind tunnel,* (2001).

[66] P. Castellucci and K. Salari, *Computational Simulation of Tractor-Trailer Gap Flow with Drag-Reducing Aerodynamic Devices*, Tech. Rep. (SAE, 2005).

[67] B. Duncan, L. D'Alessio, J. Gargoloff, and A. Alajbegovic, *Vehicle aerodynamic impact of on-road turbulence,* in *Proceedings in Mechanical Engineering Part D: Journal of Automobile Engineering* (2017).

[68] J. Barden and K. Gerova, *An on-road investigation into the conditions experienced by a heavy goods vehicle operating within the united kingdom,* Transportation Research Part D: Transport and Environment **48**, 287 (2016).

[69] M. Salim and S. Cheah, *Wall y+ strategy for dealing with wall-bounded turbulent flows,* in *Proceedings of the International MultiConference of Engineers and Computer Scientist*, Vol. II (2009).

[70] W. Hucho, L. Janssen, and H. Emmelmann, *The optimization of body details - A method for reducing the aerodynamic drag of road vehicles*, Tech. Rep. SAE Technical Paper 760185 (SAE, 1976).

[71] B. L. Storms, Satran, Heineck, and Walker, *A study of reynolds number effect and drag-reduction concept on a generic tractor-trailer,* in *34th AIAA Fluid Dynamics Conference and Exhibit* (2004).

[72] D. J. B. Calvert, *Definition of the ellipse,* `https://mysite.du.edu/~jcalvert/math/ellipse.htm` (01-09-2015).

[73] A. Znidaric, *Heavy-duty vehicle weight restrictions in the eu,* `http://www.acea.be/uploads/publications/SAG_23_Heavy-Duty_Vehicle_Weight_Restrictions_in_the_EU.pdf` (2015).

[74] DAF, *Specification sheet - fat xf105 super space cab,* `http://www.daf.com/en/products/euro-6-range/product-specification-sheets-search-euro-6` (2018).

[75] SAE, *Closed-test-section wind tunnel blockage corrections for road vehicles,* SAE (1996).